Decay Studies of ^{178}Au and Its Daughter ^{174}Ir

Monther Hamed AL-Monthery

Doctor of Philosophy

University of York
Physics
January 2019

Decay Studies of ^{178}Au and Its Daughter ^{174}Ir

Monther Hamed AL-Monthery

Abstract

Over the past several years, multiple studies by means of in-source laser spectroscopy for the isotopic chains of gold, astatine, mercury and bismuth have been carried out at the CERN ISOLDE facility by the Windmill-RILIS-ISOLTRAP-IDS collaboration. Relevant to the present work, in the experiment dedicated to studies of the long chain of gold isotopes, two alpha-decaying states were identified in ^{178}Au. The results from the laser-spectroscopy measurement showed that both of these states in ^{178}Au were proved to be strongly deformed.

To shed further light on this phenomenon, a dedicated in-beam γ-ray and α-decay study was performed at the gas-filled separator, RITU, at the Accelerator Laboratory in Jyväskylä, Finland. The ^{178}Au nuclei were produced in the fusion-evaporation reaction ^{92}Mo(^{88}Sr,np)^{178}Au. A combination of the JUROGAM II gamma-ray array and the RITU gas-filled separator was used, complemented by the GREAT spectrometer at the focal plane of RITU. The nucleus ^{174}Ir, the α-decay daughter of ^{178}Au, was also studied.

The much higher statistics obtained in the RITU investigation, in comparison to the complementary study of ^{178}Au performed at ISOLDE, allowed to detect several new fine structure alpha decays in ^{178gs,is}Au. This knowledge provides further input in respect of the puzzling discovery in the ISOLDE experiment of three unhindered α-decays of ^{178}Au, which is a situation, hardly known for any other nuclei. Furthermore, the present study identified two sub-microsecond isomeric transitions in ^{178}Au. These are built on top of both α-decaying ground and isomeric states in ^{178}Au. The identification of these isomeric states considerably simplifies the construction of rotational bands in this nucleus, the first examples of which are presented in this work.

Declaration

This thesis has been submitted for the degree of Doctor of Philosophy in accordance with the regulations of the University of York. The work contained herein has not been previously submitted for any other degree or qualification. I declare that the work here is my own, and where other sources of information have been used, they are clearly marked and referenced.

Acknowledgement

As Gertrude Stein once said "Silent gratitude isn't very much to anyone.", therefore I begin by acknowledging those who have given me great support and shown high forms of kindness.

For the long hours he invested, for the guidance and wisdom he bestowed upon me and for the vast patience he extended towards me; my thanks goes to my commendable supervisor Andrei Andreyev. My appreciation extends to my supervisor Charles Barton III, for his countless efforts, time, never ending enlightenment and valuable knowledge.

My appreciation also goes out to my respected colleague Stephen for helping in coding for GRAIN and ROOT. My thanks is given to James as well for being alongside me in every experiment in Jyväskylä and CERN. I thank my dear nuclear physics group colleagues and my old office mates Rubena and Aliyu for their company in the dreariest of days. My gratitude goes out to Luke and our scientific and social conversations. Thank you Antonio deeply for the theory discussion, Laura for her wonderful home parties.

I wish to thank the CERN and Jyväskylä staff for their support in the experiments. I am grateful for my supportive parents and siblings for their care and concerns, my three kids (Reem, Laura and Hamed) whom have become my world and finally my wonderfully brilliant wife Badriya for all the struggles she had to face alongside me and all the sacrifices she had to endure, this is all for you.

Contents

List of Figures

List of Tables

Chapter 1

Introduction

It is common knowledge that investigating doubly odd nuclei is an extremely challenging undertaking. The reason is that the coupling of the odd valence nucleon (proton, neutron) may result in multiplets of numerous low-lying energy states, and the subtle energy differences between these states may lead the study to become further complicated.

One of the fundamental properties of the nucleus is its shape. In its simplest form, the nuclear potential well is spherical. In fact, most of the nuclear ground states are deformed, as shown in Figure 1.1. In partially filled nuclear shells, the deformation is mainly caused by the tendency of the valence nucleons to polarise the nuclear core, which leads to a non-spherical mass distribution. Along with the aforementioned statements, certain observables could not be explained under the spherical potential well framework, such as the existence of rotational bands and the nuclear quadrupole moments. The widest deviation from the spherical shape is that of the quadrupole shape, wherein the shape can be elongated (prolate), disk-shaped (oblate) or triaxial.

The attribute of having different shapes in a single nucleus within a small excitation energy range (as compared to the mass scale of the nucleus) is referred to as *shape coexistence* or, sometimes, *shape isomerism*. Historically, the first observation of shape coexistence was found in the doubly-closed shells ^{16}O [Mor56] and

^{40}Ca [RW10]. The evidence of shape coexistence in the ^{16}O nucleus is supported by the characteristic rotational band spacing built on top of the $K^{\pi} = 0^{+}$ states and the strong $B(E2)$ γ transition within the band, as seen in Figure 1.2 (a). As the rotational band builds on top of the $K^{\pi} = 0^{+}$ band, indicating that the nucleus is deformed since quantum mechanically, a spherical nucleus cannot rotate. A similar behaviour is seen in ^{40}Ca, where the first 0^{+} excited state is interpreted as the excitation of a proton pair and neutron pair across the second closed shell Z ,N=20 leading to a deformed shape that can rotate and is built upon the excited 0^{+} state.

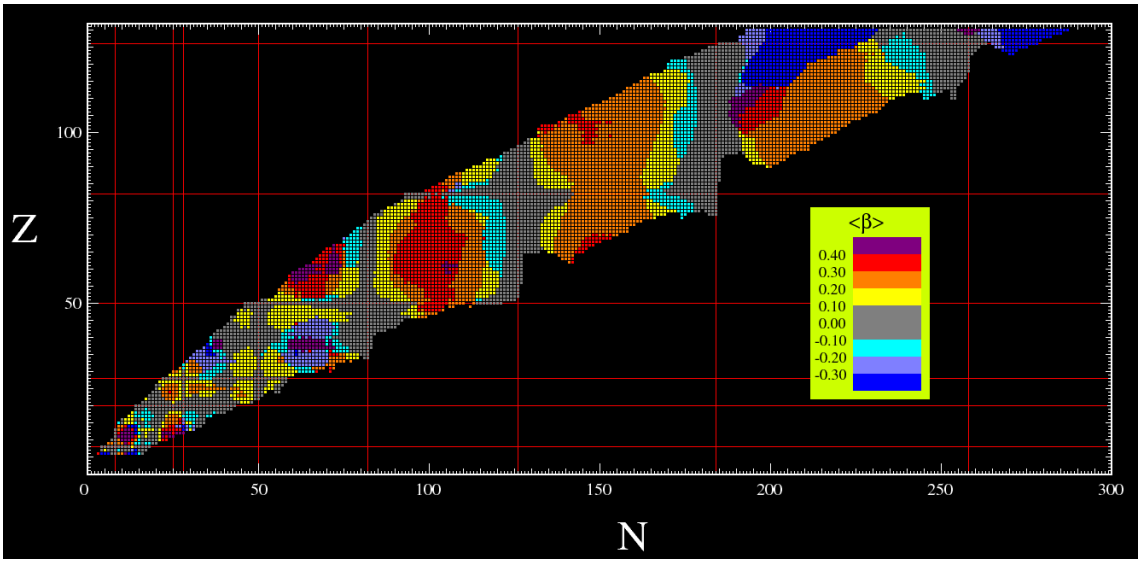

Figure 1.1: The nuclear landscape as a function of the ground-state quadrupole deformation for nuclei with N < 300. Spherical ground-states are indicated in grey and occupy small regions of the nuclear landscape typically near the closed proton and neutron shells indicated by the horizontal and vertical lines. Most of the nuclear landscape has significant quadrupole deformation indicated by the magnitude of β. The Figure is taken from [HG16].

This work is a constituent of an extensive systematic research program on topics related to the nuclear structure surrounding the shell closure $Z = 82$, such as nuclear decay studies, nuclear deformation and shape coexistence. The thesis consists of seven chapters. Chapter 2 underlines the theoretical approach for the current work, focusing on certain nuclear models, nuclear decays and the introduction of the shape coexistence phenomenon. Chapter 3 provides a brief presentation on the analysis methods used in the work and the experimental methodology. The analysis and the interpretations of ^{178}Au and ^{174}Ir are discussed in Chapters 4 and 5 respectively. Chapter 6 contains the detection of two μs isomers in ^{178}Au. The last chapter summarises the main finding in this work along with the recommended

future work.

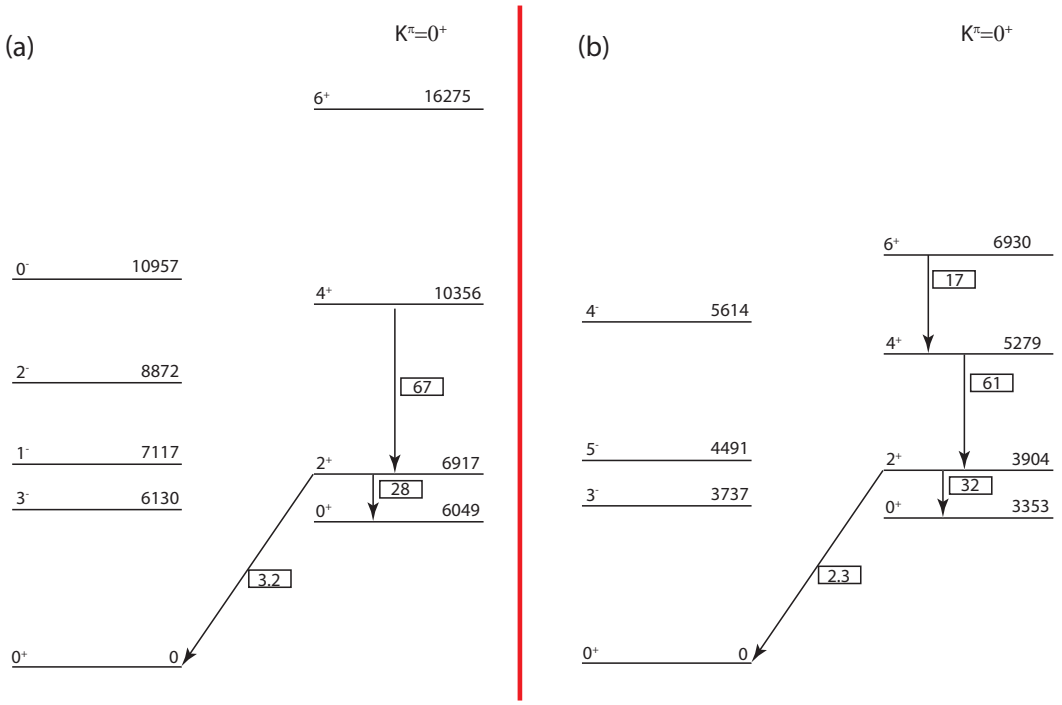

Figure 1.2: Level schemes for (a) ^{16}O and (b) ^{40}Ca. The E(2) γ transitions are indicated by an arrow and the values in the boxes are the transition strengths in Weisskopf units. The first excited 0^+ state clearly has a rotational band built upon it in both cases. The Figure is reproduced from [RW10].

1.1 Previous Studies of ^{178}Au and Motivation

Neutron-deficient isotopes in the vicinity of the Z = 82 proton shell gap and N = 104 neutron mid-shell gap have become one of the most extensively characterised regions of low-energy shape coexistence [HW11; Hey+83; Woo+92]. To date, forty-two gold isotopes have been identified. One isotope is stable (^{197}Au), while twenty-eight are neutron-deficient and thirteen are neutron-rich isotopes [NND]. The very neutron-deficient ^{178}Au isotope has 19 neutrons fewer than the stable ^{197}Au isotope.

Previous recoil-decay tagging method used to populate excited states in ^{177}Au [Ven+17] using ^{92}Mo(^{88}Sr, p2n) reaction and identified by using Jurogam-II and GREAT spectrometers in conjunction with the RITU gas-filled separator at the University of Jyväskylä Accelerator Laboratory. In this work, a strongly coupled band and its decay path to the $K = \Omega = 11/2^-$ (13/2) α-decaying isomer has been observed. This configuration has a very low degree of rotational alignment relative

to the prolate cores of ^{178}Hg and ^{176}Pt configurations.

Venhart *et al.* [Ven+11] investigate shape coexistence in ^{179}Au. A new isomeric state has been observed for the first time at 89.5 keV state. The states associated with the $\pi s_{1/2}^{-1}$, $\pi d_{3/2}^{-1}$ and established an excitation energy of $\pi h_{9/2}^{+1}$ and $\pi f_{7/2}^{+1}$ intruder states. The minimum of the parabolic trend is unambiguously established at $N = 104$ (midshell point) and the $\pi f_{7/2}^{+1}$ structure is lower in energy relative to $\pi h_{9/2}^{+1}$ with decreasing the of mass number.

A sudden jump is shown in mean-squared charge radius of Au as the neutron number approaches the N = 104 midshell [Woo+99]. This jump was interpreted to be due to a reordering of states, from nearly spherical-shell ground state $\pi 2d_{3/2}$ to intruder configuration $\pi 1h_{9/2}$. In the lighter isotopes of Au, it is predicted that the mean-square radii will approach to spherical shape. The mean-square charge radii for the ground state of Au for A $\geq$ 183 were also measured [Krö+88; Bla+97] and showed a dramatic jump from nearly spherical to deformed configuration around ^{186}Au as seen if Figure 1.3.

With an aim of understanding the nuclear structure of ^{178}Au, Potential Energy Surfaces for ^{177,178,179}Au are calculated by S. Hilaire and M. Girod using large-scale mean-field calculations [HG07]. In Figure 1.4, the calculations illustrate similar structures in the three isotopes, with a positive deformation in the ground state (prolate) competing with a low-lying negative configuration (oblate) for all three ^{177,178,179}Au isotopes.

The first observation of ^{178}Au was investigated by Siivola [Sii68] in 1968, who identified one α decay using the reactions ^{16}O+^{175}Lu, ^{20}Ne+^{169}Tm and ^{19}F+^{168}Yb. The observed α decay, with an energy of 5920 keV, has been unambiguously assigned to ^{178}Au. Keller *et al.* [Kel+86] performed a second attempt in 1986, exploiting stationary thin targets of ^{90}Y, ^{90,92,96}Zr and ^{90}Mo that were bombarded by a beam of ^{90}Zr with an energy of $E = 321 - 390$ MeV by employing the velocity filter SHIP to separate the recoils from the beam projectiles that were accelerated by the UNILAC at GSI. In this experiment, Keller *et al.* observed two new α lines along with the one that was previously known, with energies of $E_\alpha = 5850, 5920$ and 5980

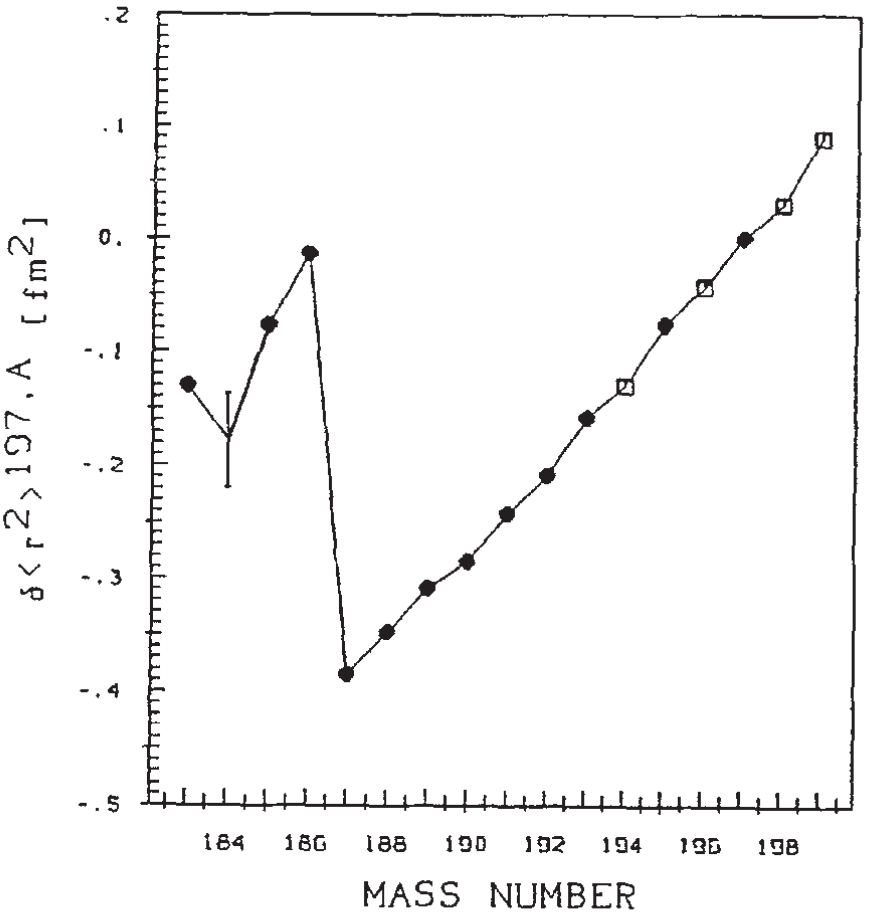

Figure 1.3: Evolution of mean-square charge radii of Au for A=183-200 [Krö+88]

.

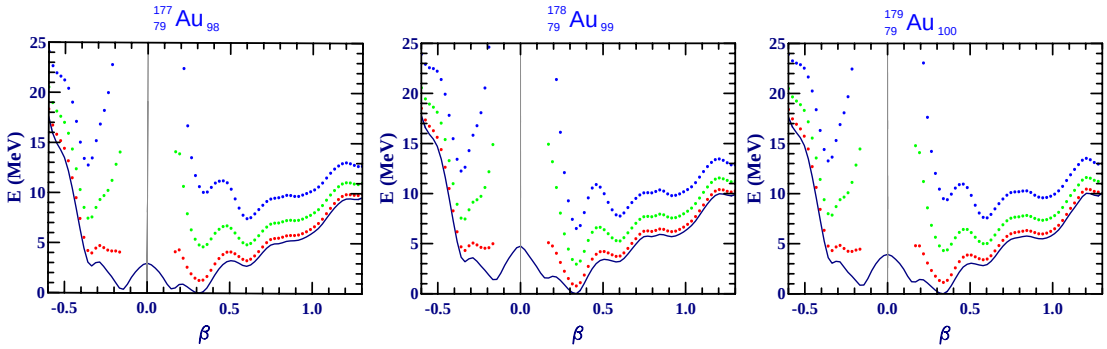

Figure 1.4: Potential Energy Surfaces for ^{177}Au (left), ^{178}Au (middle) and ^{179}Au (right panel), calculated by S. Hilaire and M. Girod [HG07] within the Large-scale mean-field approach using the D1S Gogny force. The calculation shows that the ground-state of ^{178}Au should be deformed with $\beta \sim 0.3$.

keV.

In our complementary laser spectroscopy IS534 experiment [Cub17] performed at ISOLDE CERN facility, we identified two states in ^{178}Au, a low-spin ground state and a high-spin isomeric state for the first time. The separation between the states was accomplished through hyper fine structure measurements (HFS). Tentatively, the ground state spin was assigned a spin of 3^- or ,4^-, while the isomeric state spin was 7^+ or, 8^+. The spin assignments were undertaken by analysing γ-ray decaying states populated in ^{178}Pt, the β-decay daughter of ^{178}Au. Both of the states in ^{178}Au where deformed [And15] and the main goal of the thesis is to search for rotational bands on top of each state. Based on the observation of μs isomer in ^{179}Au [Ven+11], we can also expect a similar isomer(s) in ^{178}Au. Further details on the findings, as compared to the present work are noted in Section 4.

Chapter 2

Theoretical Background

The atomic nucleus is a many-body quantum system that is characterized by the complex interactions between protons and neutrons, which are collectively called nucleons. These nucleons interact with their neighbours via the short-range strong force which acts over distances of about 1 fm. Numerous theoretical models have been developed to describe the interaction between the nucleons. Some of these were able to explain the behaviour of the nucleus under certain conditions. For example, the spherical shell model is able to describe and predict the existence of what is referred to as 'magic numbers' in the nucleus. On the other hand, this model was unable to explain the observed large quadruple moments of ^{174,175}Lu [TFL49]. In the following sections, a brief introduction to the Liquid Drop Model, the spherical shell model, and some deformed nuclear models are presented.

2.1 The Liquid Drop Model

The liquid drop model (LDM) is one of the first successful macroscopic models to describe and predict the binding energy of a nucleus as a function of mass number A (number of protons Z + number of neutrons N). The model was first proposed by George Gamow and later formalized by Carl Friedrich von Weizsäcker in 1935 [Wei35]. The LDM model describes and treats the atomic nucleus as an incompressible charged liquid drop with a spherical volume. The Weizsäcker (semi-empirical)

mass formula calculates the total binding energy of a nucleus in terms of the geometry (volume and surface), charge, quantum effects, and the nucleon mass as follows

$$B_{tot}(A,Z) = a_v A - a_s A^{2/3} - a_c \frac{Z^2}{A^{1/3}} - a_P \frac{(A-2Z)^2}{A} \pm E_\delta \,, \tag{2.1}$$

where the first term is called the volume term and arises from the fact that the binding energy increases as the mass number A becomes larger, since the nuclear force is proportional to the number of nucleons. The second term is the surface correction term, where a nucleon near the surface is not as tightly bound compared to when it is located in the interior. Therefore, the term is proportional to the surface area of the nucleus. The third term, the Coulomb term, is introduced in the formula to account for the Coulomb repulsion of protons, which reduces the binding energy of the nucleus. The symmetry or Pauli term, a_P, is the first quantum mechanical term in the formula and arises due to the effect of the Pauli exclusion principle, which states that no more than one fermion can have the same quantum numbers which is equivalent to saying that only one fermion can occupy a single particle state. Therefore, the more asymmetric proton and neutron numbers are energetically less favourable. The energy excess consequence of having an unsymmetrical nucleon number, causes the separation energy between states δ that have different values of $A \propto 1/\delta$. The a_P term is extremely important in light nuclei but less significant in heavy nuclei. The last term, the pairing term E_δ, is defined as two protons or two neutrons that form a pair that corresponds to the binding energy, which is much greater than an isolated nucleon. Table 2.1 shows the sign of the E_δ term for different nucleon numbers configurations.

Table 2.1: The sign of the paring term in even-even, odd-odd, even-odd, and odd-even nuclei.

A	Z	N	E_δ
even	even	even	+
even	odd	odd	-
odd	even	odd	0
odd	odd	even	0

Table 2.2: The semi-empirical mass formula coefficients extracted from the experimentally measured masses.

Parameter	Extracted value [MeV] [Kra87]
a_V	15.5
a_S	16.8
a_C	0.72
a_P	23
E_δ (even-even)	34
E_δ (odd-odd)	-34
E_δ (even-odd)	zero
E_δ (odd-even)	zero

The coefficients of the semi-empirical mass formula are extracted by fitting the experimentally measured masses of different nuclei shown in Figure 2.1. Table 2.2 shows the coefficients and their values that were extracted from the fit.

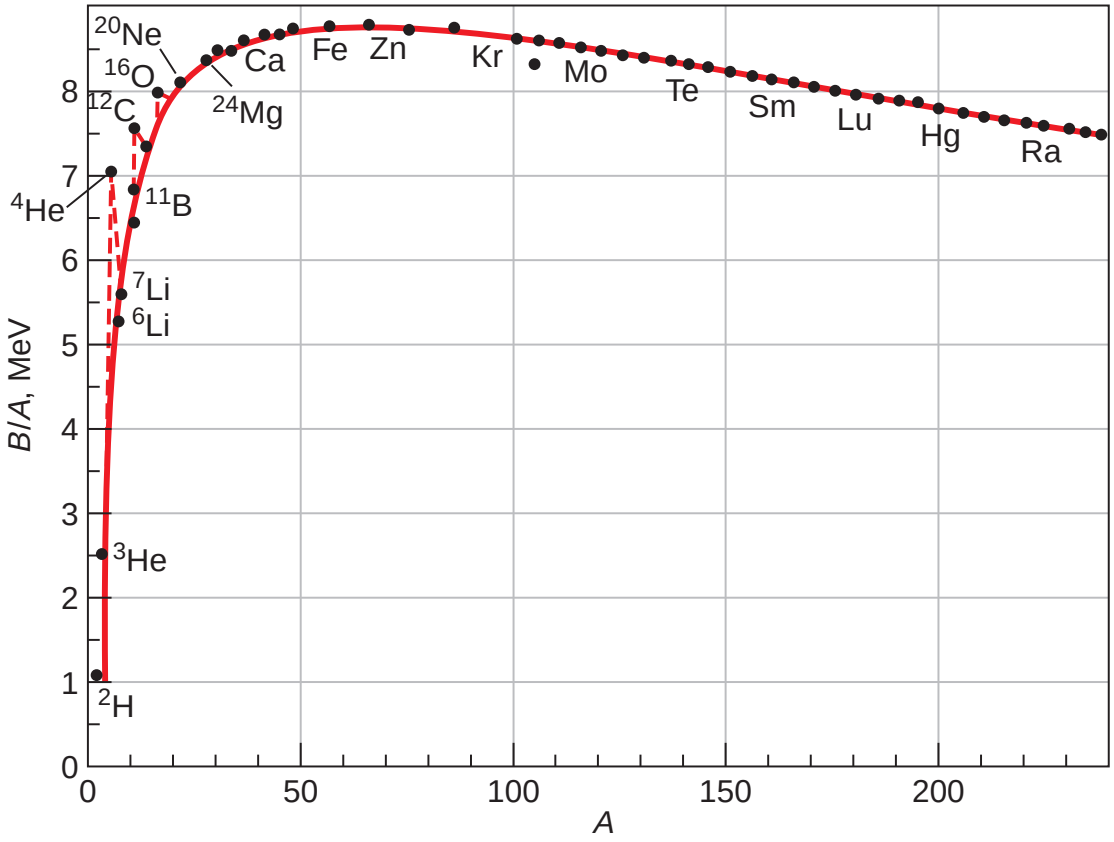

Figure 2.1: A plot of the experimentally determined nuclear data showing the binding energy per nucleon as a function of mass number A. The solid red line represents the Weizsächer semi-empirical binding-energy formula. The figure is reproduced from [TL03].

The coefficients are expressed in MeV, and the values are extracted by fitting the experimental measured masses of different nuclei.

2.2 The Spherical Shell Model

The fitting of the semi-empirical mass formula is not an absolute fit of the data curve. There are peaks (as seen in Figure 2.1), which indicates a sudden increase in the binding energy for specific nuclei. These peaks in the Figure 2.1 have been found to appear at certain numbers, Z or N = 2, 8, 20, 28, 50, 82, and 126, which are referred to as 'magic numbers' and not all of them have been predicted in the Weizsäcker formula.

The shell model of the nucleus was first proposed by Gapon and Iwanenko in 1932, [GI32] and later by Mayer [May50] and Haxel, Jensen, and Suess [HJS49], which they independently developed as a new phenomenological model that was similar to the atomic shell model. Thus, in this case, the shell model describes a nucleus as consisting of nucleons moving in specific orbits in the nucleus, similar to the manner in which electrons move inside an atom. The model presumes that the nucleon moves in a potential $V(r)$, which is created due to the interaction between the neighbouring nucleons. Solving the three-dimensional Schrödinger equation in a square well or in a harmonic oscillator nuclear potential was unable to yield all the magic numbers. A realistic potential well was developed by Woods and Saxon [WS54], where the potential at distance, r, from the centre of the core of the nucleus, and is given by

$$V(r) = \frac{-V_0}{1 + exp[\frac{r-R_0}{a}]}\,, \tag{2.2}$$

where V_0 is the depth of the nuclear potential at the centre and in the order of $\sim$ 50 MeV, R_0 is the mean radius of the nucleus and, a is the surface diffuseness. The mean radius, R_0, is measured in fm and can be calculated as follows:

$$R_0 = 1.25A^{1/3} \tag{2.3}$$

The Wood-Saxon potential is successful at producing the first three magic numbers

but fails to reproduce the rest. The Wood-Saxon potential needs to be 'slightly' modified in order to yield the proper magic numbers for the heavier nuclei. The modifications include the intrinsic angular momentum (spin) of the nucleon, s, and its orbital angular momentum, l, and it is expressed as [May50; HJS49]

$$V(r) \Rightarrow V = V(r) + V_{so}(r)\vec{l}.\vec{s}\,, \tag{2.4}$$

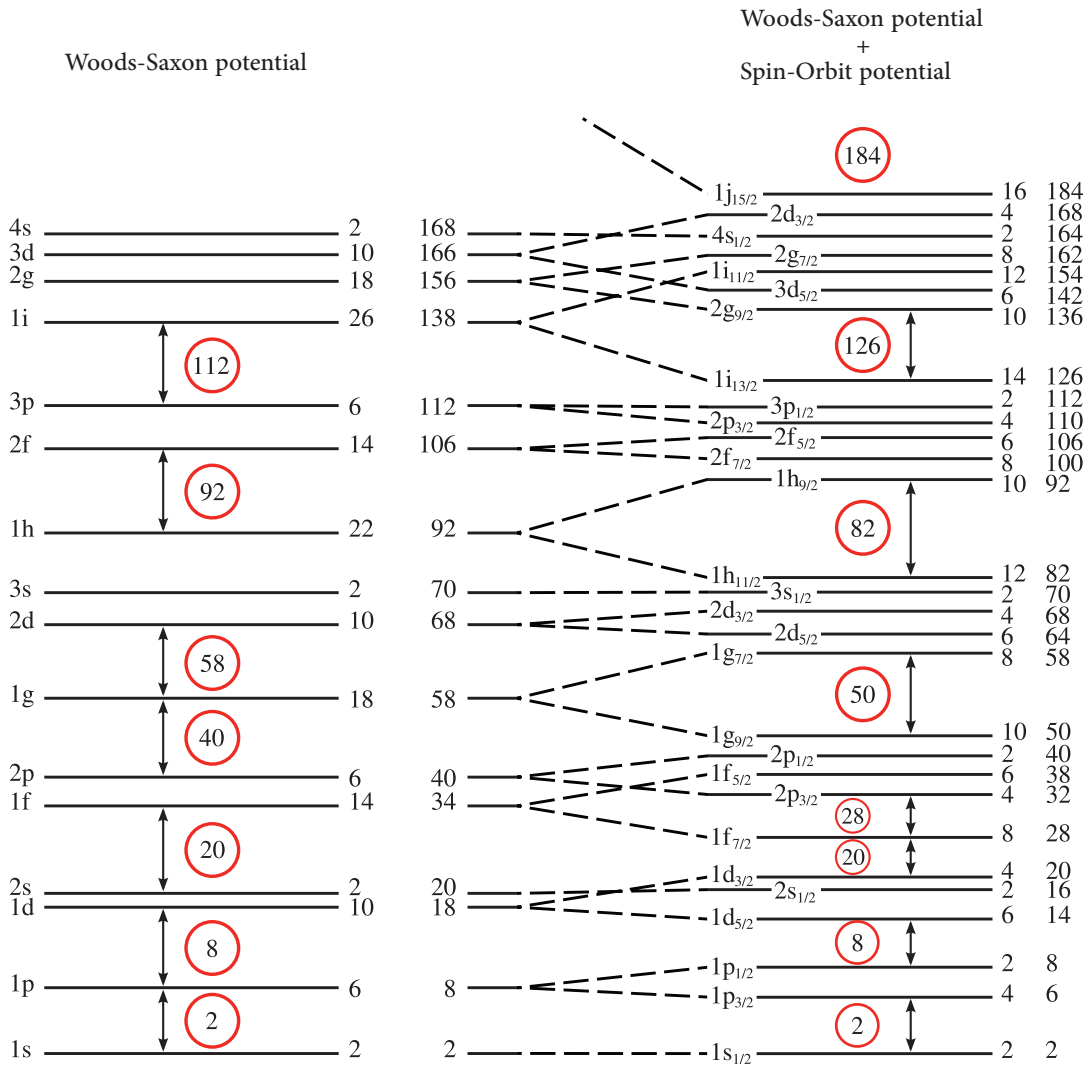

Figure 2.2: Schematic drawing of the single-particle orbitals in Woods-Saxon and the latter with spin-orbit coupling. The numbers in circles indicate the cumulative capacity up to the given orbit and are commonly called the "magic numbers". The magic numbers of the Woods-Saxon potential with a spin-orbit potential agree with experimentally observed magic numbers.

where $V_{so}(r)\vec{l}.\vec{s}$ is the strength of interaction. The spin-orbit correlation arises from the tendency of the nucleons to align their intrinsic and orbital angular moment in order to maximise the nucleus binding energy. The result of spin-orbit coupling is

the splitting of the l orbital degeneracy instead of one occupying only when $l > 0$. The energy splitting is directly proportional to l therefore, the nucleon with higher total angular momentum ($j = l + s$) is pushed deeper into the potential well, while the nucleon with total angular momentum ($j = l - s$) will be higher in energy, hence lowering the binding energy of the nucleus. The effect of including the spin-orbit interaction in the Woods-Saxon potential is illustrated in Figure 2.2. Note that each state has a degeneracy of, $2j + 1$, nucleons.

As the nucleons moves within the nuclear orbitals, another modification is needed to the total nuclear potential in order to include the centrifugal force which is calculated from

$$V_{cent}(r) = \frac{l(l+1)\hbar}{2mr^2} \tag{2.5}$$

The Coulomb potential acts between protons only and can be expressed as

$$V_{Coulmb}(r) = k\frac{Ze^2}{r}\,, \tag{2.6}$$

where k is the Coulomb's constant in expressed N.m^2.C^2 units. Therefore, this term must be included in the total nuclear potential such that:

$$V_{total} = \begin{cases} V(r) + V_{so}(r) + V_{cent}(r) + V_{Coulmb}(r) & \text{for protons} \\ V(r) + V_{so}(r) + V_{cent}(r) & \text{for neutrons} \end{cases} \tag{2.7}$$

Figure 2.3 illustrates different nuclear terms, including the Woods-Saxon potential, the spin-orbital, the centrifugal, and the Coulomb potential.

The Deformed (Nilsson) Shell Model

The Nilsson model [Nil55] is based on a modification of the spherical shell model, where the nuclear potential well is 'deformed' instead of being spherical. In this

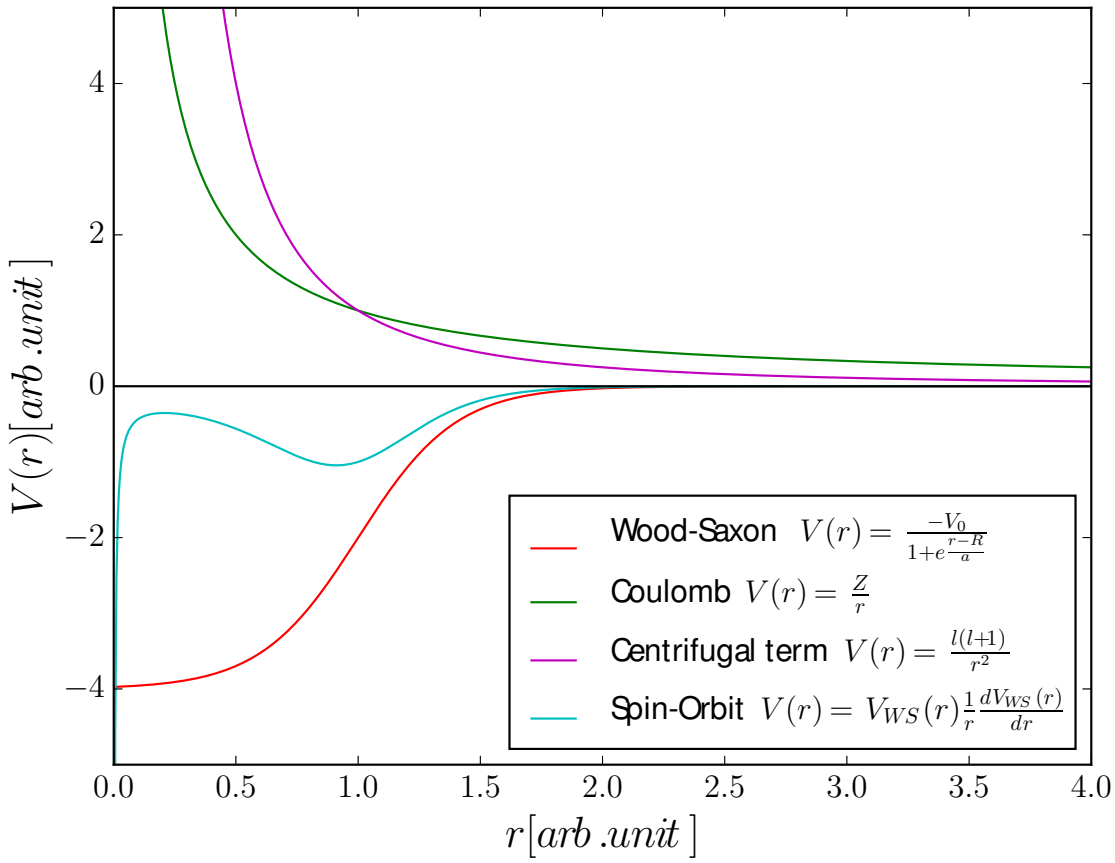

Figure 2.3: A plot of the different nuclear potential component terms from Equation 2.7. See text for details.

model, the deformation of the nucleus has a significant impact on the single-particle energy states. Unlike the shell model, where each level holds $2j + 1$ nucleon(s), the model's degeneracy for a particular level is 2. Plots of a single-particle energy in units of oscillator frequency, $\hbar\omega$, versus deformation parameter ϵ_2 are illustrated in Figures 2.4 and 2.5 for the region under investigation (^{178}Au).

New quantum numbers, called "asymptotic quantum numbers", are required to identify each eigenstate, which are labelled as

$$[Nn_z\Lambda]\Omega^\pi \,, \tag{2.8}$$

where

N= the major oscillator shell number.

n_z= the number of oscillator quanta in the z symmetry axis.

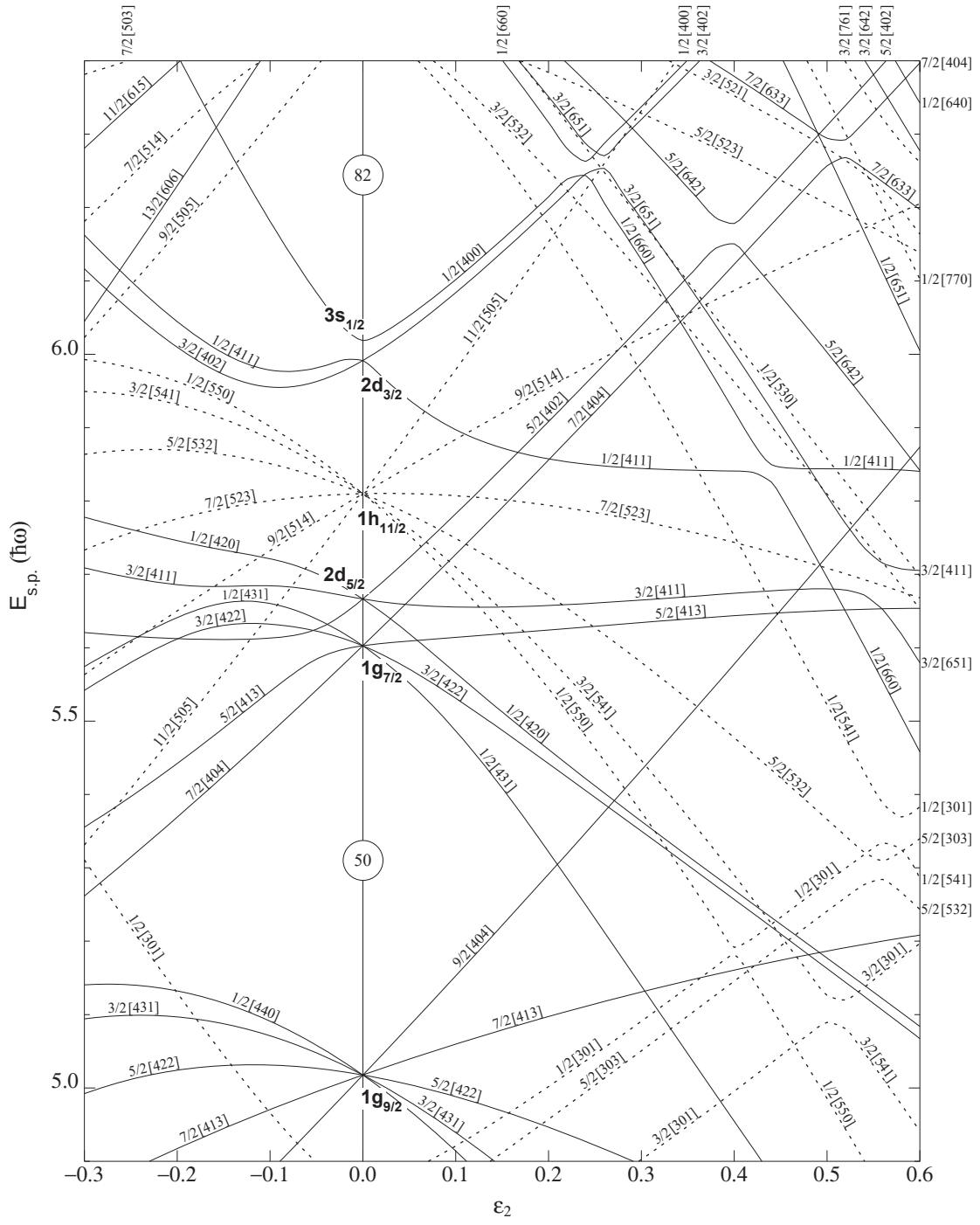

Figure 2.4: Nilsson diagram for protons, $50 \leq Z \leq 82$ [Fir+96].

$\Lambda=$ the projection of I, the orbital angular momentum along the symmetry axis z. $\Lambda = \Omega - 1/2$.

$\Omega=$ the magnitude projection of the total angular momentum j on the symmetry axis, z (the overlap of the orbital with the core). $\Omega = \Lambda + 1.2$

$\pi=$ the parity[1] of the state.

[1]The term parity π is used to describe the reflection symmetry quantum number of a state. The parity of a system can be positive or negative, $\pi = +, -$.

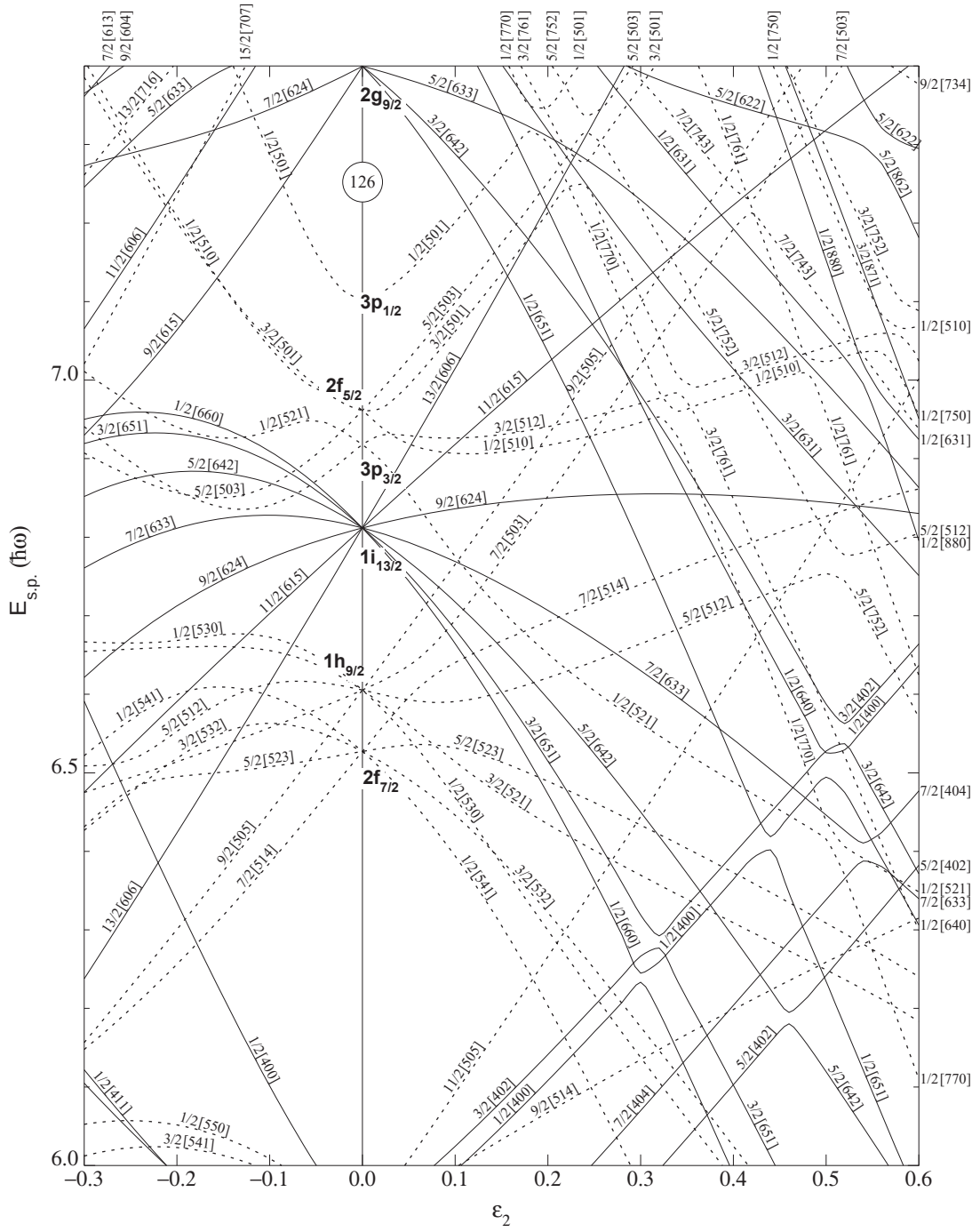

Figure 2.5: Nilsson diagram for neutrons, $82 \leq N \leq 126$ [Fir+96].

The components of the asymptotic quantum numbers are shown in Figure 2.6. From the figure, the orbit of a prolate deformed shape interact strongly with the lowest possible Ω $(\frac{1}{2})$, hence enhancing the bound energy of the particle. While the contrary occurs in the oblate shape, where the highest possible wave-function of $\Omega = j$ interacts strongly with the core, which leads to the lowest possible particle energy

(tightly bound).

The deformation parameter, β_2, is defined in terms of ε_2 in the following series

$$\beta_2 = \sqrt{\frac{16\pi}{5}} \left(\frac{1}{3}\varepsilon_2 + \frac{1}{9}\varepsilon_2^2 + \frac{1}{27}\varepsilon_2^3 + \frac{1}{81}\varepsilon_2^4 ... \right) , \tag{2.9}$$

where the two parameters, ϵ_2 and β_2, are comparable in low values of deformation.

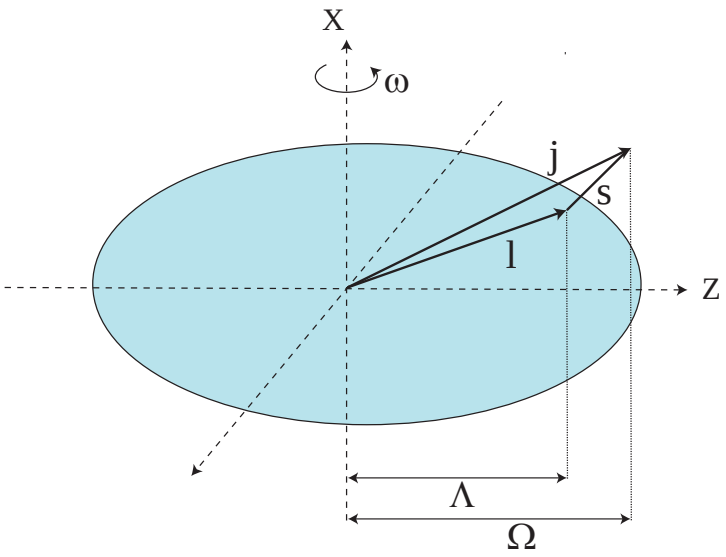

Figure 2.6: The components of the quantum numbers used to in the Nilsson model. See text for details.

2.3 The Collective Models

The nuclear shell model can give a reasonable explanation for the ground and low-lying excited states of odd-A and odd-odd nuclei. The accuracy rises even further in the vicinity of the closed shells and closed sub-shells. Nuclear collective models combine aspects of the shell model and the LDM to explain some of the nuclear properties that could not been explained from the spherical shell model, e.g. the first excited state of almost all even-even nuclei have $J^\pi = 2^+$.

Nuclear Vibration

The vibrational model treats the nuclear excitations as fluctuations in the nuclear density distribution around an equilibrium point [Hey04]. The nuclear shape at time t can be represented mathematically in terms of polar coordinates (θ, φ) as

$$R(t) = R_{av}\left\{1 + \sum_{\lambda\geq 1}^{\infty}\sum_{\mu=-\lambda}^{+\lambda}\alpha_{\lambda\mu}(t)Y_{\lambda\mu}(\theta,\varphi)\right\}, \tag{2.10}$$

where $R(t)$ is the nuclear radius at time t, as illustrated in Figure 2.7, R_{av} is the average spherical equilibrium shape calculated from Eq. 2.3, and $\alpha_{\lambda\mu}$ is the amplitude of the spherical harmonics $Y_{\lambda\mu}$ as a function of time. The multipolarity of the shape is designated by λ, while μ describes the projection of the λ vector ranging from $-\lambda$ to λ. The vibrational energy is called phonon and it is quantised in units of $\hbar\omega_\lambda$, where ω_λ is the oscillation frequency of the nucleus. For an ideal vibrator, the ratio of the one and two phonon excitations is $\frac{E(4^+)}{E(2^+)} = 2$. Disregarding the monopole vibration $\lambda = 0$, where the nucleus is incorporated into R_{av}, the first two vibrational modes are given below:

- The dipole vibration

  $\lambda = 1$, $\mu = 0, \pm 1$; the nucleus moves its displacement forward and backward with respect to the centre of mass. The $\mu = 0$ mode describes the nucleus movement along the z direction, while the other two modes correspond to the movement perpendicular to the z axis.

- The quadrupole vibration,

  - $\lambda = 2$, $\mu = \pm 2$

    The nuclear matter changes its distribution as a function of time such that; oblate-spherical-oblate-spherical, etc. This mode is called 'Gamma' vibration.

  - $\lambda = 2$, $\mu = \pm 1$

    This mode violates the parity and, therefore, it cannot be allowed.

– $\lambda = 2$, $\mu = \pm 0$

This mode is called 'Beta' vibration, and the shape transition follows, prolate-spherical-oblate, etc.

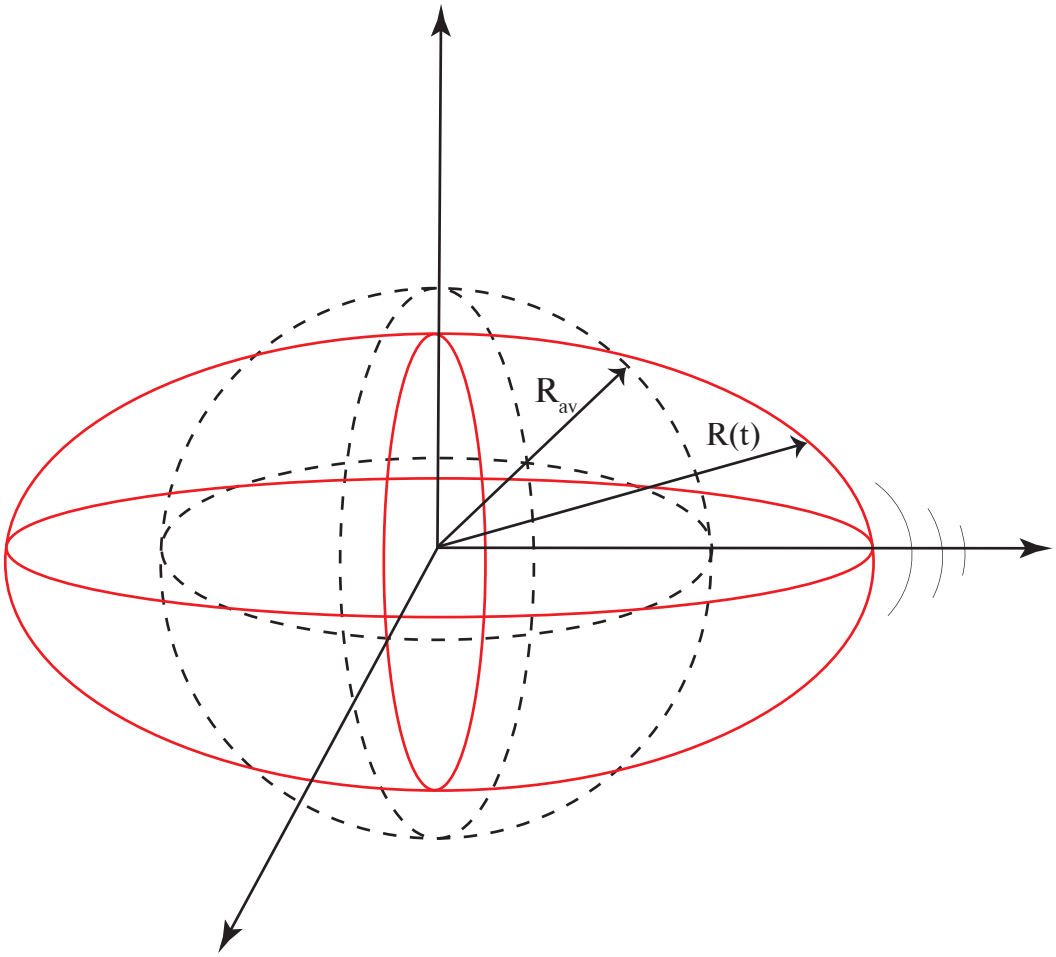

Figure 2.7: The nuclear vibration with a spherical equilibrium shape.

Nuclear Rotation

A statically deformed shape can occur in the nucleus and this can undergo rotational motion. Note that the rotation of a spherical nucleus is quantum mechanically forbidden. The total angular momentum of a nucleus I is obtained by adding the rotational angular momentum vector, R, and the sum of the intrinsic angular mo-

mentum of the individual valence nucleon $J = \sum j$.

$$I = R + J \tag{2.11}$$

Figure 2.8 shows a schematic single-particle total angular momentum J coupling with the core angular momentum R, and the projection of J and I onto the symmetry axis is denoted by K for axially symmetric nuclei.

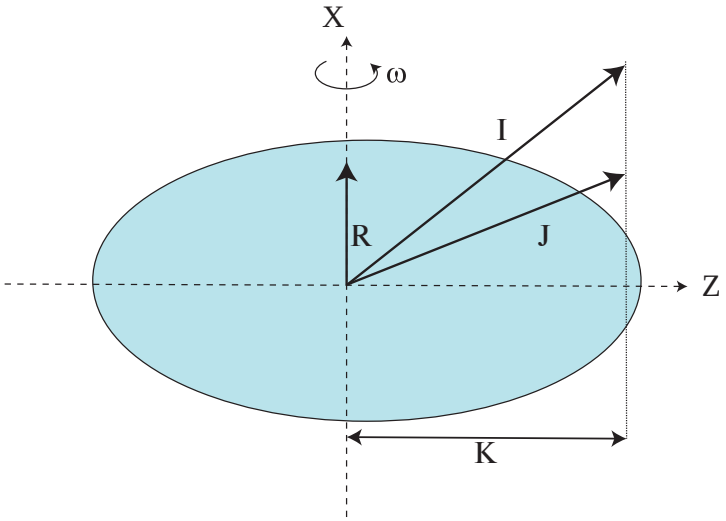

Figure 2.8: Schematic showing the components of a rotating nucleus. The total angular momentum I results from the coupling of the rotating nuclear core R with the valence nucleons J.

The general expression that describes a deformed system is

$$R(\theta, \varphi) = R_{av} \left\{1 + \beta Y_{20}(\theta, \varphi)\right\} \ , \tag{2.12}$$

where $R(\theta, \varphi)$ is the radius of the nucleus as a function of polar angles. The deformation parameter, β, describes the extent to which the nucleus has changed from the spherical shape as

$$\beta = \frac{4}{3}\sqrt{\frac{\pi}{5}\frac{\Delta R}{R_{av}}} \ , \tag{2.13}$$

where ΔR is the difference between the semi-minor and semi-major axes of the ellipse. Thus, if $\beta > 0$, the shape is called prolate; whereas, if $\beta < 0$, the shape is

an oblate.

The kinetic energy of a rotating rigid object is given by

$$E_{rot} = \frac{1}{2}\mathcal{I}\omega^2 = \frac{I^2}{2\mathcal{I}}; \quad \omega = \frac{I}{\mathcal{I}}\,, \tag{2.14}$$

where $\mathcal{I}$ is the moment of inertia, and I is the total angular momentum quantum number. The rotation of the nucleus is proportional to the energy states in terms of $I(I+1)$:

$$E_{rot} = \frac{\hbar^2}{2\mathcal{I}} I(I+1) \tag{2.15}$$

From equation 2.15, it can be observed that the signature of rotational behaviour in a nucleus is the ratio of the energies of first 2^+ and 4^+ states, $\frac{E4^+}{E2^+} \sim 3.33$.

2.4 Nuclear Decay Modes

Radioactive decay is the process of an unstable nucleus losing energy by emitting particles or undergoing electromagnetic decay. The radioactive decay law describes the decay of a nuclear as state as a function of time

$$\lambda = -\frac{1}{N}\frac{dN}{dt}\,, \tag{2.16}$$

where λ is the decay constant and N the number of nuclei at time t. The integration of Equation 2.16 yields the 'exponential law of radioactive decay' as

$$N(t) = N_0 e^{-\lambda t}\,, \tag{2.17}$$

where N_0 is the original number of nuclei at time $t = 0$. The half-life, $t_{1/2}$, is the

time required for half of the nuclei ($N_0/2$) to decay:

$$t_{1/2} = \frac{ln2}{\lambda} \tag{2.18}$$

In the following sections, different nuclear decay modes are discussed, including alpha, beta, and gamma decays.

2.4.1 Alpha Decay

The process of an alpha decay is the emission of a charged particle identical to the atomic nucleus of helium, ${}^{4}_{2}\mathrm{He}^{2+}_{2}$. The repulsive Coulomb force is responsible for the emission of the particle.

Nature requires the nuclei to get rid of as much excess energy as feasible, as quickly as possible. The α particle is the most suitable candidate for emission in proton-rich heavy-nuclei for several reasons. It is light compared to the heavy nucleus and considered have high binding energy (28.3 MeV) [Mar06], as it is a doubly magic nucleus.

The mechanism of the decay is presented as follows:

$$ {}^{A}_{Z}\mathrm{X}_{N} \rightarrow {}^{A-4}_{Z-2}\mathrm{Y}_{N-2} + \alpha \,, \tag{2.19}$$

where X and Y are the mother and daughter nuclei respectively. The condition for α decay to occur spontaneously is when the net energy released in the reaction, Q_α-value, is greater than 0 (or exothermal), where Q_α-value is the difference between the binding energy, B, of the mother decaying nucleus and the binding energy of the products (daughter + α particle). The Q_α-value is the total kinetic energy of the products ($T_Y + T_\alpha$), and it is shared between the α particle and the recoiling daughter. However, since the atomic mass of the heavy recoiling daughter is much higher than the atomic mass of α ($m_Y \gg m_\alpha$), the recoiling energy is normally neglected.

$$
\begin{aligned}
Q_\alpha &= (m_X - m_Y - m_{^4\mathrm{He}})c^2 = T_Y + T_\alpha \\
&= \overbrace{B(Z-2, A-4) + B(2,4)}^{\text{Products}} \quad - \quad \underbrace{B(Z,A)}_{\text{Decaying nucleus}}
\end{aligned}
\tag{2.20}
$$

Typical α particle energies are between $4 - 8$ MeV, and it can be treated as non-relativistic. Thus, classical mechanics can be used to relate the Q_α-value with the T_α in the following manner:

$$
\begin{aligned}
Q_\alpha &= T_\alpha \left[1 + \frac{m_\alpha}{m_Y} \right] \\
&\approx T_\alpha \left[\frac{A}{A-4} \right]
\end{aligned}
\tag{2.21}
$$

The total angular momentum carried by an α particle from the mother nucleus, ℓ_α, is purely orbital since the intrinsic spin of the α particle is zero. The α particle carries ℓ_α from the initial state, i, to the final state, f, from the mother nucleus in the range $|I_i - I_f| < \ell_\alpha < I_i + I_f$, and the parity may change to $(-1)^{\ell_\alpha}$. The parity selection rules are responsible for populating different final states in the daughter nucleus after an α decay, which is sometimes referred to as the '*fine structure*' of α decay. If the parity is the same in the initial and the final states, ℓ_α is even; whereas, if there is a change in the parity, ℓ_α is odd.

From classical mechanics point of view, the α decay process is forbidden. This fact is best illustrated in Figure 2.9, in which the nuclear potential is represented by the finite square well. The potential well in this case is a combination of a Coulomb force and a centrifugal term. The magnitude of the Coulomb term is proportional to the number of protons squared.Inside the well, the α particle interacts with the square well potential, while outside the nuclear surface (r>R), the potential is governed by the Coulomb repulsion force only with contribution from the centrifugal barrier if $\ell \neq 0$. Typically, Q_α is much lesser than the potential barrier (B); therefore, the emission of the α particle from a nucleus occurs by penetrat-

ing it via 'quantum tunnelling'. This explanation was first introduced by Gamow [Gam28], and by Gurney and Condon [GC28], in 1928, where the probability of the emission of an α particle from a nucleus depends on three terms [ZRL11]:

$$\lambda_\alpha = f.P_{preform}.P_{tunnel} \ , \tag{2.22}$$

where f is the α particle assault frequency on the potential barrier, $P_{preform}$ is the probability of forming the α cluster inside the mother nucleus, and P_{tunnel} is the probability of the α particle penetrating the Coulomb barrier through quantum tunnelling. The assault frequency is often calculated by presuming that the α particle moves classically back and forth inside the mother nucleus.

The probability of the α particle tunnelling through the barrier is calculated as

$$P_{tunnel} \approx exp\left(\frac{-4a\pi}{h}\sqrt{2m(V-E)}\right) \ , \tag{2.23}$$

where m is the reduced mass of the daughter nucleus and α particle, V is the potential barrier, a is the thickness of the barrier, E is the kinetic energy carried by the particle and h is Planks Constant.

The reduced α width, δ^2, describes the pre-formation probability of the α particle inside the mother nucleus, and also includes the overlapped wave-functions of the initial and final states. The different α-decay rates are compared using the following expression:

$$\delta^2 = \frac{\lambda h}{P_{tunnel}} \tag{2.24}$$

The α-decay rates can be compared using what is known as the '*reduced hindrance factor*' HF. The HF is extremely sensitive to spin and parity changes

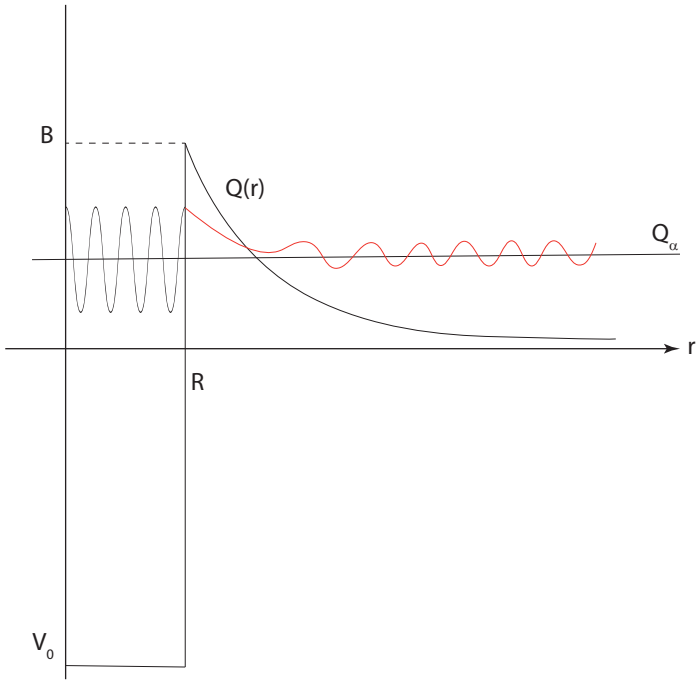

Figure 2.9: A schematic image illustrating a one-dimensional α particle wave-function at energy Q_α and daughter-nucleus potential energy. The α particle tunnels from the daughter-nucleus square well through the Coulomb barrier formed by the charge of the daughter nucleus.

between the initial and final state of α decay. The hindrance factor is calculated as

$$HF = \frac{\delta^2_{gs}}{\delta^2_{es}}\,, \tag{2.25}$$

where δ^2_{es} and δ^2_{gs} are the reduced α width for the α decay fine-structure (ground state to excited state) as compared to the un-hindered α decay (ground sate to ground state), respectively.

Experimentally, the δ^2 can be deduced directly by knowing, the α energy, E_α, half-life $t_{1/2}$, the branching ratio of the fine-structure α decay b_α, the intensity of the α decay I_α, and the penetration probability P [VH00], as illustrated below:

$$\delta^2 = \frac{h \times I_\alpha \times ln(2) b_\alpha}{t_{1/2} \times 100 \times P} \tag{2.26}$$

2.4.2 Beta and Electron Capture Decays

The β decay produces a continuous energy spectrum of β particles in the range $0 < E_\beta < Q_\beta$, where the maximum energy is the Q-value of the β decay. In general, a heavy radioactive nucleus with excess neutrons may experience a β^- decay as follows:

$$ {}^{A}_{Z}X_N \rightarrow {}^{A}_{Z+1}\,Y_{N-1} + e^- + \overline{\nu}e + Q_{\beta^-}\ , \tag{2.27} $$

where X, Y are the mother and daughter nuclei respectively, $\overline{\nu}e$ is the electron antineutrino and Q_{β^-} is the decay Q-value.

The small electron binding energy differences between the mother and daughter nuclei can be neglected; therefore, the Q_{β^-} can be calculated from the energy difference of the mother and daughter nuclei, such that

$$ \begin{aligned} Q_{\beta^-} &= M({}^{A}_{Z}X_N)c^2 - Zm_ec^2 - M({}^{A}_{Z+1}Y_{N-1})c^2 + (Z+1)m_ec^2 - m_ec^2 \\ &= M({}^{A}_{Z}X_N)c^2 - M({}^{A}_{Z+1}Y_{N-1})c^2\ , \end{aligned} \tag{2.28} $$

where the masses are expressed in atomic masses.

Analogous to β^- decay, a nucleus with an excess number of protons may convert a proton into a neutron, hence undergoing β^+ decay as

$$ {}^{A}_{Z}X_N \rightarrow {}^{A}_{Z-1}\,Y^-_{N+1} + e^+ + \nu e + Q_{\beta^+}\ , \tag{2.29} $$

where the negative charge of the daughter nucleus is due to an extra electron created in the reaction. Therefore, the decay Q-value, Q_{β^+} must include this electron in the following manner:

$$\begin{aligned} Q_{\beta^+} &= M(^A_Z X_N)c^2 - Zm_e c^2 - M(^A_{Z-1}Y_{N+1})c^2 + (Z-1)m_e c^2 - m_e c^2 \\ &= M(^A_Z X_N)c^2 - M(^A_{Z-1}Y_{N+1})c^2 - 2m_e c^2 \ , \end{aligned} \tag{2.30}$$

where the masses are expressed in atomic masses unit. Electron capture (EC) is the competing process with β^+ decay, where the condition of the reaction is that the energy difference between the daughter and parent nuclei should be at least double the electron's rest mass. In this decay mode, the wave-function of a deeply bound electron overlaps greatly (compared with electrons from other shells) with the mother nucleus, resulting in the 'capturing' the electron by the nucleus and the emission of a neutrino:

$$^A_Z X_N + e^- \rightarrow ^A_{Z-1} Y_{N+1} + \nu \tag{2.31}$$

The Q-value of the EC process is given by the following equation:

$$\begin{aligned} Q_{EC} &= M(^A_Z X_N)c^2 - (Z-1)m_e c^2 - M(^A_{Z-1}Y_{N+1})c^2 + (Z-1)m_e c^2 - E_B(e^-) \\ &= M(^A_Z X_N)c^2 - M(^A_{Z-1}Y_{N+1})c^2 - E_B(e^-) \ \ , \end{aligned} \tag{2.32}$$

where $E_B(e^-)$ is the electron binding energy.

The vacancy of the captured electron may be occupied by an electron from a higher orbital. During this process, a characteristic X-ray (usually K-shell) is emitted from the atom with an energy equal to the difference between the two orbital states.

The spin-parity selection rules involved in the β decay are summarised in Figure 2.10.

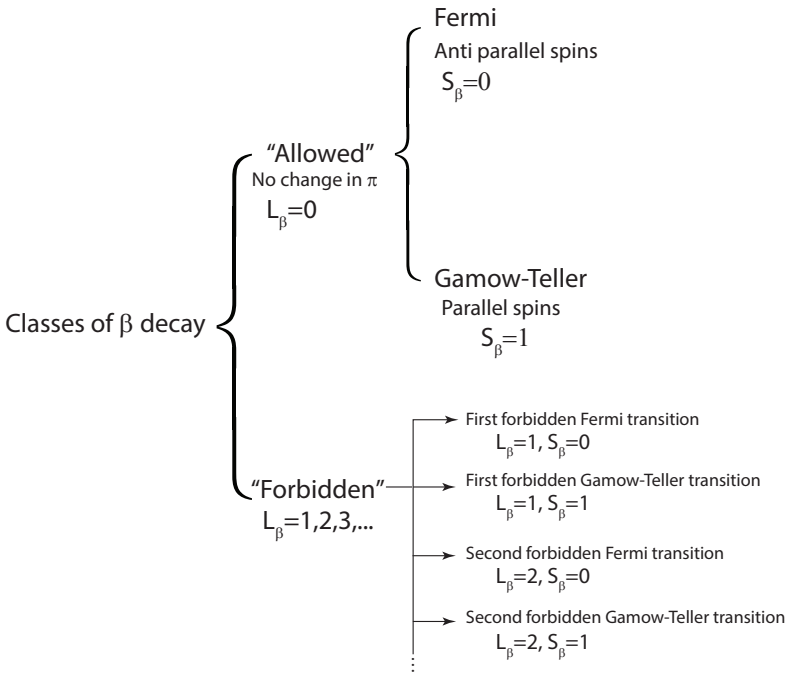

Figure 2.10: β decay selection rules. L_β, is the change in the spin, and S_β is the total spin of the coupled $\beta - \nu$ fermions pairs. Allowed transitions occur when there is no angular momentum transferred from the parent nucleus, $L_\beta = 0$. Forbidden transitions occur when at least one unit of angular momentum is carried away from the mother nucleus. The degree of *forbiddeness* depends on the amount of angular moment removed from the mother nucleus.

2.4.3 Electromagnetic Decay

An excited state in a nucleus can depopulate by emitting electromagnetic photons called gamma (γ), rays in order to reach a lower state. The γ transition does not change the number of nucleons, as

$$ {}^{A}_{Z}X^{*}_{N} \rightarrow {}^{A}_{Z}X_{N} + \gamma \,, \tag{2.33} $$

with ${}^{A}_{Z}X^{*}_{N}$ representing the nucleus in its excited state. In such a transition, energy, E_γ, and angular momentum, ℓ_γ, are removed from the nucleus. The energy of this photon, E_γ, is the energy difference between an excited state, E_i, and a lower state, E_f, while neglecting the extremely small recoiling energy of the nucleus, which is in the order of 10^{-7} MeV (for A=180 and $E_\gamma \sim 0.5$ MeV); therefore, $E_\gamma = E_i - E_f$.

As the γ ray is an electromagnetic radiation, it can be described in mul-

tipole moment expansion. The charge and current distributions generate electric and magnetic fields, which are converted into an emission of an electromagnetic radiation.

The γ-ray transition probability from an initial state to a final state, is expressed as

$$\lambda(\sigma\ell_\gamma; I_i \to I_f) = \frac{8\pi(\ell+1)}{\hbar\ell_\gamma[(2\ell_\gamma+1)!!]^2}\left(\frac{E_\gamma}{\hbar c}\right)^{2\ell_\gamma+1} B(\sigma\ell_\gamma; I_i \to I_f), \quad (s^{-1}), \quad (2.34)$$

where $B(\sigma\ell_\gamma; I_i \to I_f)$ is the '*reduced transition probability*' of the γ ray. The reduced transition probability provides information about the nuclear structure regarding the two states connected by the γ transition. The reduced transition probability is classified in two types- electric transition

$$B(E\ell_\gamma; I_i \to I_f) = (2I_i+1)^{-1}\left|\left\langle f \left\| \hat{M}(E\ell_\gamma) \right\| i \right\rangle\right|^2, \quad (2.35)$$

and magnetic transition

$$B(M\ell_\gamma; I_i \to I_f) = (2I_i+1)^{-1}\left|\left\langle f \left\| \hat{M}(M\ell_\gamma) \right\| i \right\rangle\right|^2, \quad (2.36)$$

where the electric and magnetic multipole operators are designated by $\hat{M}(E\ell_\gamma)$ and $\hat{M}(M\ell_\gamma)$ respectively. The calculation of $B(\sigma\ell_\gamma; I_i \to I_f)$ requires information about the nuclear wave-function. However, by assuming the transition between two states is the result from a single nucleon (proton) changing its orbit, an estimate for $B(\sigma\ell_\gamma; I_i \to I_f)$ can be made , which is called '*Weisskopf estimates*' or "*single particle estimates*" [Wei51], and expressed in unit per time. Table 2.3 illustrates the calculated transition rates and reduced transition probabilities for the first four electric and magnetic multipole orders. The strength of a transition can be expressed in units of Weisskopf, W.u, using the ratio $t_{1/2}^{Weisskopf}/t_{1/2}^{experimental}$. Typical experimental values are listed in Table 2.4.

Table 2.3: The calculated transition rates in terms of reduced transition probabilities $B(EL)$ (e^2fm^{2L}) and $B(ML)$ $\mu_N^2 fm^{2L-2}$ (top), along with the Weisskopf estimates (bottom), for the first four multipole γ transition. The transition energy E is in MeV.

Multipolarity	Transition Probability (s^{-1})
E1	$\lambda(E1) = 1.587 \times 10^{15}.\ B(E1).\ E^3$
E2	$\lambda(E2) = 1,223 \times 10^{9}.\ B(E2).E^5$
E3	$\lambda(E3) = 5.698 \times 10^{2}.\ B(E3).E^7$
E4	$\lambda(E4) = 1.694 \times 10^{4}.\ B(E4).E^9$
M1	$\lambda(M1) = 1.779 \times 10^{1}3.\ B(M1).E^3$
M2	$\lambda(M2) = 1.371 \times 10^{7}.\ B(M2).E^5$
M3	$\lambda(M3) = 6.387 \times 10^{0}.\ B(M3).E^7$
M4	$\lambda(M4) = 1.889 \times 10^{6}\ B(M4).E^9$
Multipolarity	**Weisskopf Estimates (s^{-1})**
E1	$B_{sp}(E1) = 1.03 \times 10^{14}.A^{2/3}.E^3$
E2	$B_{sp}(E2) = 7.3 \times 10^{7}.A^{4/3}.E^5$
E3	$B_{sp}(E3) = 3.33 \times 10^{1}.A^{2}.E^7$
E4	$B_{sp}(E4) = 1.1 \times 10^{-5}.A^{8/3}.E^9$
M1	$B_{sp}(M1) = 5.6 \times 10^{13}.E^3$
M2	$B_{sp}(M2) = 3.5 \times 10^{7}.A^{2/3}.E^5$
M3	$B_{sp}(M3) = 1.6 \times 10^{1}.A^{4/3}.E^7$
M4	$B_{sp}(M4) = 4.5 \times 10^{-6}.A^{2}.E^9$

Table 2.4: Typical experimental values of $t_{1/2}^{Weisskopf}/t_{1/2}^{experimental}$ for A $\geq$ 150.

B(E1)	$\sim$	10^{-2}	W.u
B(M1)	$\sim$	10^{-1}	W.u
B(E2)	$\sim$	10^{2}	W.u

The γ-ray transition obeys two selection rules

- The total angular momentum of the gamma transition is restricted between two values

$$|I_i - I_f| \leq \ell_\gamma \leq I_i + I_f \tag{2.37}$$

The ℓ_γ is an integer, and its lower limit, $I_\gamma = |I_i - I_f|$, is favourable because the γ-ray emission probability is proportional to $(\frac{R}{\lambda})^{2\ell_\gamma}$ [Eva55].

- The parity selection rule stated that, for an electric transition, the parity is even $(+)$ when the angular momentum is even; whereas, for a magnetic transition, the parity is odd $(-)$ when the angular momentum is even. The electromagnetic field's parity is

$$\begin{aligned} \Delta\pi(E\ell_\gamma) &= (-1)^{\ell_\gamma} \,, \\ \Delta\pi(M\ell_\gamma) &= (-1)^{\ell_\gamma+1} \end{aligned} \tag{2.38}$$

Transitions with, $E2, M3, E4, M5, \ldots$ multipolarities do not alter their parities, while it is vice versa for the transitions $E1, M2, E3, M4, \ldots$ Mixed transitions of the same parity (e.g. $M1/E2$) are allowed as well.

A monopole transition between two states of 0^+, resulting in no change in angular momentum ($\ell_\gamma = 0$), is forbidden for a single γ emission process, as the photon must carry at least $\ell_\gamma = 1$ angular momentum. In this case, the process can only proceed through what is known as '*Internal Conversion*', where in one of the atomic electrons is emitted from its shell, or by internal pair formation, for energies higher than 1.022 MeV, which is equivalent to twice the rest mass of an electron. The wave-function overlap among the bound electrons and the nucleus is responsible for this phenomenon. The probability of emitting an electron from the K-shell is higher than other shells on account of it being closer to the nucleus; hence, its higher overlap wave-function. The kinetic energy of the emitted electron, T_e, then is

$$T_e(K, L, M, ...) = (E_i - E_f) - B_e(K, L, M, ...) \,, \tag{2.39}$$

where $B_e(K, L, M, ...)$ is the electron binding energy in its $(K, L, M, ...)$ electronic shell.

The emitted conversion electron creates a vacant hole and, as a consequence, an electron from a higher orbit fills its place. This process leads to the emission of an $X-$ray, which could be detected in coincidence with the conversion electron.

The internal conversion process competes with the γ emission; therefore, the total internal conversion coefficient is defined as

$$\alpha_{ICC} = \frac{I(e_{K,L,M,...})}{I_\gamma} \,, \tag{2.40}$$

where $I(e_{K,L,M,\ldots})$ is the total number of the conversion electrons from the atomic shells $(K, L, M, \ldots)$, and I_γ is the number of γ rays per excited nucleus. Furthermore, the total conversion coefficient is the sum of all sub-coefficients from each atomic shell, i.e. $\alpha_{ICC} = \alpha_K + \alpha_L + \alpha_M + \ldots$

2.5 Shape Coexistence in the Atomic Nucleus

Nuclear configurations having different deformations or shapes within a similar energy range at low spin states is called 'shape coexistence'. Shape coexistence was first observed in the doubly-close shells ^{16}O [Mor56], where the first two 0^+ states have different shape configurations.

The appearance of the '*intruder states*' concept is one of the interpretations of shape coexistence in the atomic nuclei [HW11], where the state (which is supposed to lie high in energy in the next major shell) intrudes into the lower shell. The intruder state will be of opposite parity since it comes from a different major shell. The intruder states are obtained by exciting a pair of nucleons across a shell gap, as seen in the top of Figure 2.11. The excitation energies of the intruder state are lower than the one predicted by the shell model, which can be calculated as

$$E_{intr} = 2(\varepsilon_{j\pi} - \varepsilon_{j'\pi}) - \Delta E^{\pi\pi}_{pair} + \Delta E^{\pi\nu}_{M} + \Delta E^{\pi\nu}_{Q} \,, \tag{2.41}$$

where the $2(\varepsilon_{j\pi} - \varepsilon_{j'\pi})$ term describes the unperturbed energy to create a $2p-2h$ configuration, which is defined by the proton energy in the single-particle orbitals. The second term, $\Delta E^{\pi\pi}_{pair}$, describes the pairing energy gain as the coupling of protons or holes increases the binding energy of the nucleus, thus lowering the excitation energy. The third term, $\Delta E^{\pi\nu}_{M}$, describes the monopole correction to the proton single-particle energy (depends on the neutron number) in which it can be attractive or repulsive, and the last term describes the proton-neutron quadrupole binding energy.

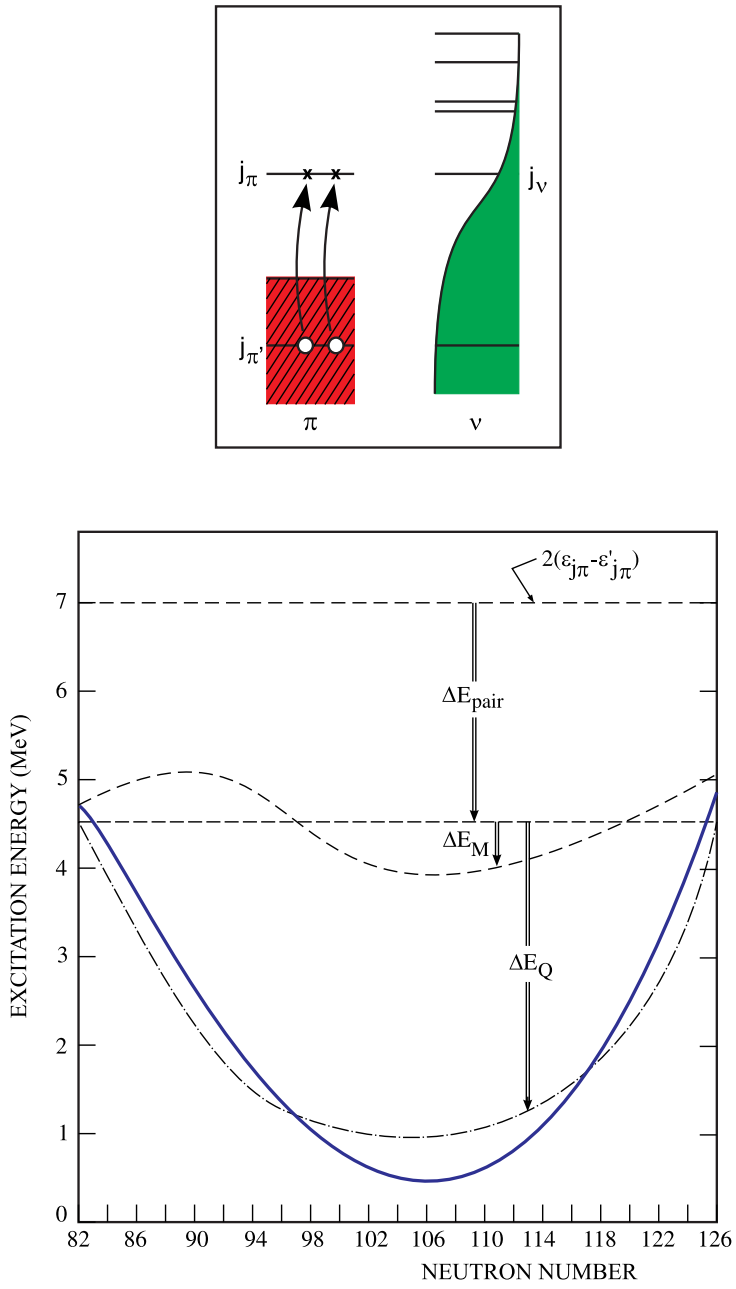

Figure 2.11: The contributing energy terms of the lowest proton $2p-2h$ intruder state for heavy nuclei. (Top), a schematic view of the excitation process. (Bottom), a schematic view of the individual energy terms contributing to Equation 2.41. The figure is produced from reference [HW11].

Chapter 3

Experimental Setup and Analysis Techniques

This chapter contains a brief introduction to the fusion-evaporation reactions were used to produce the nucleus under investigation. The equipment used in the experiment will be presented along with the primary analysis techniques.

3.1 Heavy-ion Fusion Evaporation Reactions

In order to study nuclear structure at the extremes from the beta stability line, fusion evaporation reactions are established to produce a neutron-deficient nuclei. For the fusion reaction to occur, a beam and a target are fused together to form a compound nucleus, where they must overcome the Coulomb barrier, B_c,

$$B_c \approx 1.44\text{MeV.fm.}\frac{Z_b.Z_t}{r_b + r_t}\,, \tag{3.1}$$

where $Z_{b(t)}$ is the proton number of the projectile (target) and $r_b(t)$ represent the projectile (target) radius. The time scale sequence of the process is presented in Figure 3.1.

Usually, fusing two stable nuclei will result in the production of a neutron-

deficient compound nucleus, since the nuclear stability line falls below the Z=N line. The highly-excited compound nucleus at approximately 10^{-21} s from the formation, undergo particle (proton, neutron, *etc.*) evaporation in order to lose excitation energy of the system. After this stage, where the threshold of particle emission is reached, γ ray decay dominated the decay mode in the vicinity of $^{-13}$ s from forming the compound nucleus. These γ rays emitted in a continuum spectrum range due to the high density of states of their origin. Once the evaporation residues reach the yrast line[1] , γ rays emitted in a cascade from discrete energy states.

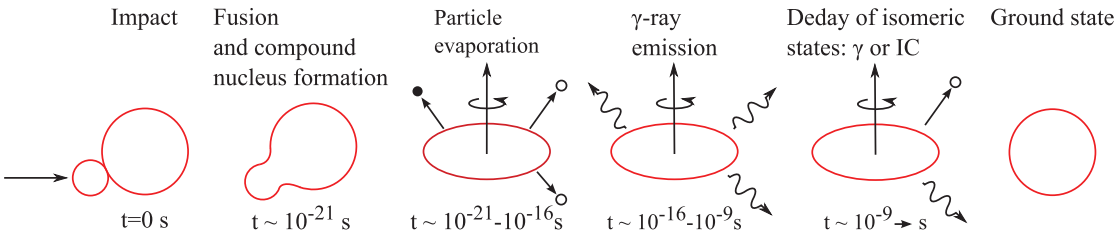

Figure 3.1: A schematic illustration of the fusion-evaporation reaction as it evolves with time. Time advances from the left, with the initial impact, to the right, where the product nucleus is in its ground state. The figure is reproduced from [Aur15].

3.2 Experimental Apparatus

The experiment consist of three main areas- the target position, the gas separator, and the focal plane of RITU. Each of these locations consists of numerous different radiation detectors. In the following sections, the setup apparatus along with the analysis techniques used in the present work are described.

3.2.1 The JUROGAM II γray Spectrometer Array

Prompt γ rays emitted from excited energy states were detected by the JUROGAM II γ-ray spectrometer (Figure 3.2). The detector array was placed at the target position upstream of the gas-filled separator. The JUROGAM II detector consists of twenty four EUROGAM Clover detectors [Duc+99] and fifteen EUROGAM phase

[1]The yrast line represent the states with the lowest energies for given spins.

one [Bea+92] or GASP-type germanium detectors [Alv93] arranged in four rings around the target chamber, as illustrated in Figure 3.2. The EUROGAM and GASP detectors have tapered edges to maximise the solid angle coverage. Each Clover detector comprised four individual crystals. The position of each detector is defined via two angels- θ and ϕ. Table 3.1 shows the arrangement of each detector of the JUROGAM II Array.

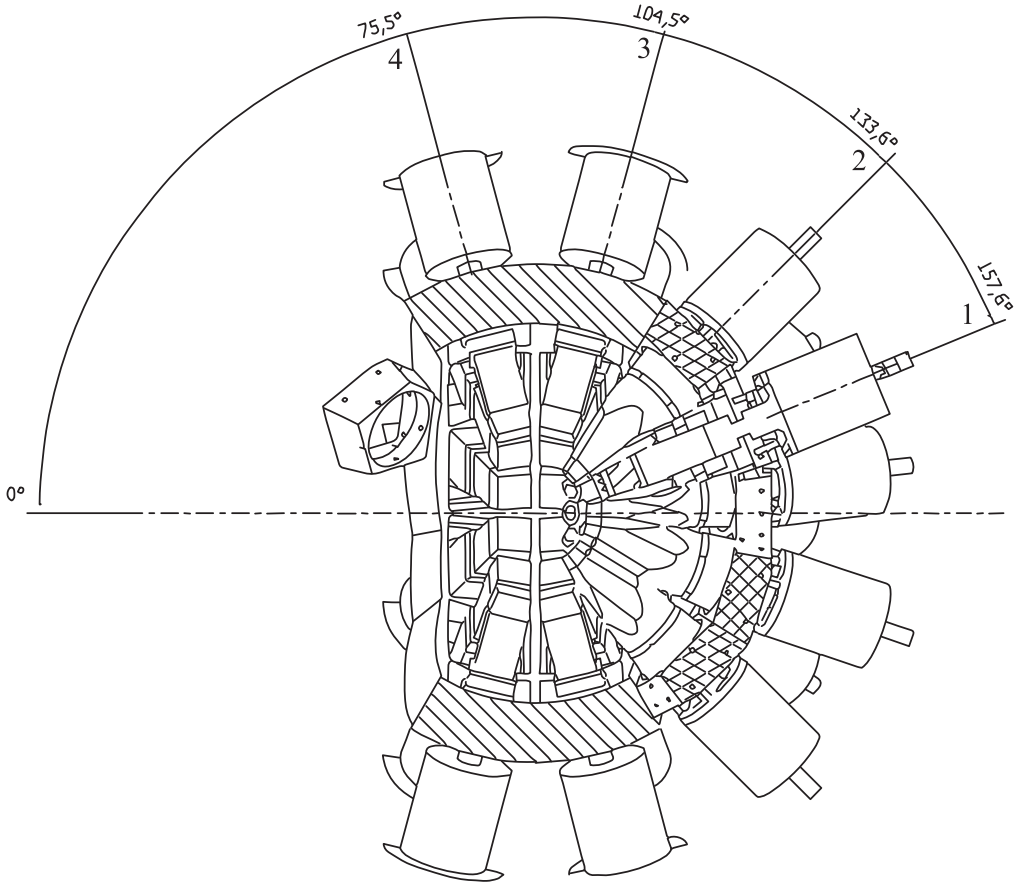

Figure 3.2: Schematic drawing of the JUROGAM II array γ-ray spectrometer. The detectors arranged in 4 rings where the angles defines the position of the detector with respect to the beam direction.

Furthermore, all the Ge detectors of the JUROGAM II were surrounded by anti-Compton bismuth germinate (BGO) shields. These BGO's act as anti coincidence detectors to improve the peak-to-background ratio of the γ-ray spectrum. The signals were discarded if there was a signal in the detectors that is in coincidence with the BGO signal, where the γ rays could arise from Compton scattered that

have not deposited their full energy in the germanium crystals.

Table 3.1: The position of each detector of the JUROGAM II spectrometer array. T represents tapered detector and Q is a Clover detector. θ is the angle with respect to the beam direction, while ϕ is the angle with respect a vertical line that increase in a clockwise direction when viewing the spectrometer from an upstream position.

Ring Number	Detector type	θ°	ϕ°
1	T01	157.6	0
1	T02	157.6	72
1	T03	157.6	144
1	T04	157.6	216
1	T05	157.6	288
2	T06	133.57	18
2	T07	133.57	54
2	T08	133.57	90
2	T09	133.57	126
2	T10	133.57	162
2	T11	133.57	198
2	T12	133.57	234
2	T13	133.57	270
2	T14	133.57	306
2	T15	133.57	342
3	Q01	104.5	15
3	Q02	104.5	45
3	Q03	104.5	75
3	Q04	104.5	105
3	Q05	104.5	135
3	Q06	104.5	165
3	Q07	104.5	195
3	Q08	104.5	225
3	Q09	104.5	255
3	Q10	104.5	285
3	Q11	104.5	315
3	Q12	104.5	345
4	Q13	75.5	15
4	Q14	75.5	45
4	Q15	75.5	75
4	Q16	75.5	105
4	Q17	75.5	135
4	Q18	75.5	165
4	Q19	75.5	195
4	Q20	75.5	225
4	Q21	75.5	255
4	Q22	75.5	285
4	Q23	75.5	315
4	Q24	75.5	345

3.2.2 The Recoil Ion Transport Unit

The **R**ecoil **I**on **T**ransport **U**nit [Uus+03; Lei+95] (RITU) gas-filled separator is used to separate the fusion products from the unreacted beam. It consists of four strong magnets in the configuration Q_V-D-Q_H-Q_V, where Q is a quadrupole magnet and D is a dipole magnet, while the subscripts, V and H, represent vertical and horizontal focusing, respectively. A schematic figure of the RITU gas-separator and the arrangement of its magnets is shown in Figure 3.3. The first quadrupole magnet,

located directly after the target chamber, is used to vertically focus the recoils for better acceptance by the dipole magnet. The purpose of the dipole magnet D is to separate the unwanted unreacted beam from the fusion evaporation reaction products. The last two quadrupole magnets are exploited to first focus the recoils horizontally then vertically for better acceptance in the focal plane detectors.

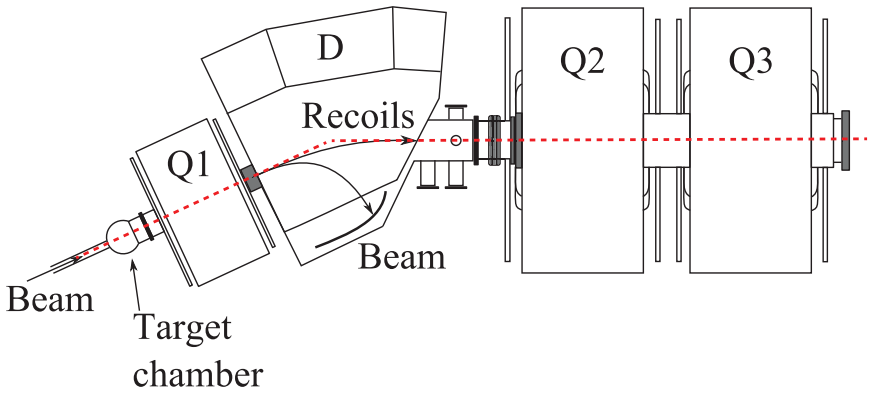

Figure 3.3: The gas-filled recoil separator RITU that is used to separate the fusion-evaporation residues from the projectile beam. D and Q represent the focusing dipole and the separating quadrupole magnets respectively. RITU is typically filled with $\sim$ 1 mbar of helium. The figure is adopted from [Aur15].

The separator is filled with helium gas, with an average pressure $\sim$ (0.5 — 1) mbar. The collisions between the recoils moving inside the RITU and the gas atoms result in charge state fluctuations due to electron capture and loss. The beneficial aspect of this technique is that it allows for a great transmission efficiency as compared to the vacuum mode. The negative aspect is that it does not distinguish between different recoils due to the removal of the mass-to-charge ratio information. These two features are shown in Figure 3.4.

The average charge state q_{avr} is expressed using the Thomas-Fermi model [Boh41] of an atom

$$q_{avr} = eZ^{1/3}(\frac{v}{v_B}) \, , \tag{3.2}$$

where v is the velocity of the recoil, v_B is the Bohr velocity:

$$v_B = 2.19 \times 10^6 \mathrm{m/s}$$

The electron electrical charge is determined by e, and Z is the proton number.

The magnetic rigidity, $B\rho$, of the first dipole magnet D is the main feature that separates the beam from the recoil products such that

$$B\rho = \frac{mv}{eq_{avr}}\,, \tag{3.3}$$

where B is the magnetic field flux density, m is the mass of the particle, and ρ is the radius of the curvature of the ions path. The magnetic field B must be adjusted to obtain the best selectivity of the nucleus under investigation. The magnetic rigidity is measured in units of Tesla-meters (Tm) and can reach up to 2.2 Tm.

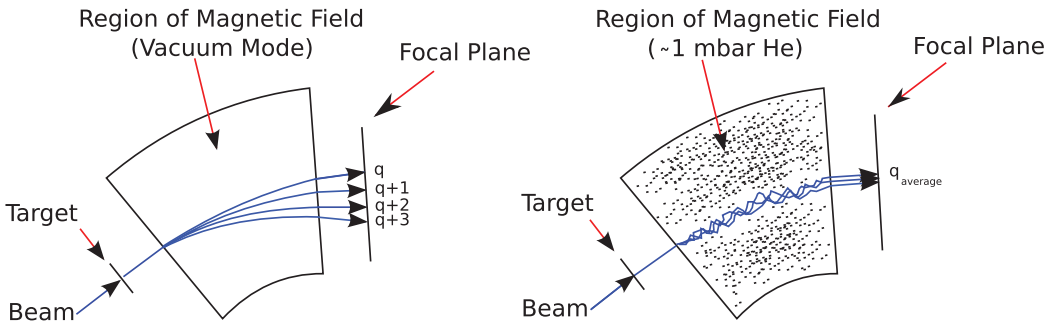

Figure 3.4: A schematic view showing the primary difference between the gas-filled and vacuum separators. In both modes, the magnet is perpendicularly out of the page. Due to the charge state of the recoils is taken from the gas in the gas-filled separator, the focussing and the transmission of them is higher than the vacuum mode. The figure is taken from [Ang12].

3.2.3 The GREAT Spectrometer

The **G**amma **R**ecoil **E**lectron **A**lpha **T**agging (GREAT) spectrometer [Pag+03] was designed to detect recoils and their decay products following a nuclear implantation. The spectrometer system is located at the focal plane downstream of the RITU. The GREAT spectrometer consists of different nuclear-decay detectors that together aim to measure and explore the isomeric and ground states for nuclei. The GREAT spec-

trometer consists of **M**ulti-**W**ire **P**roportional **C**ounter (MWPC), **D**ouble-**S**ided **S**ilicon **S**trip **D**etector (DSSSD), silicon PIN-diode detectors (not used in the analysis), a **P**lanar **G**ermanium **D**etector (PGD), and Clover detectors. Figure 3.5 shows a photograph of the GREAT system. These different detectors and their properties are described in the subsequent sections.

Figure 3.5: The location of the GREAT detector chamber relative to the Clovers. The PGD, PIN-diodes, and the DSSSDs are located inside the chamber detector.

Multi-Wire Proportional Counter (MWPC)

The multi-wire proportional counter is a type of gas-filled transmission detector. The recoils pass through the MWPC before being implanted into the DSSSD. The grid in the detector provides a position and energy loss signals of the recoils with their time-stamps. The MWPC window covers an active area of 131 mm (horizontal) × 50 mm (vertical). The MWPC detector contains two Mylar windows- one separates the isobutane gas from the helium gas in that RITU, and the other isolates the detector from the GREAT spectrometer vacuum.

The main purpose of the MWPC is to differentiate between the fusion reaction products passing through it and their radioactive decays. This is achieved by placing a two-dimensional gate on a two-dimensional plot of the energy loss of the

recoils versus the time-of-flight (ToF) of the recoils as detected in the MWPC and implanted into the DSSD. Time to Amplitude Converter (TAC) measures the ToF between the MWPC and the DSSSD (Section 3.2.3) detectors, since the distance between the two detectors is short. More details about the discrimination method are given in Section 3.6.1.

Double-Sided Strip Detector

Flexible degrader foils are used to slow down the recoils before they are implanted into a pair of 300-μm-thick double-sided silicon strip detectors (DSSSD) (Fig 3.6) that are located 240 mm downstream of the MWPC. The dimensions of each DSSSD are 60 mm $\times$ 40 mm, resulting in an effective area of 4800 pixels in total. The pair of DSSSDs are mounted side by side with a 4 mm gap in between. The DSSSD detectors are cooled to around -25°C using a liquid ethanol circulation system in order to improve detector resolution. The detector is used to identify the implanted recoils and their subsequent decays such as alpha particles and protons. The efficiency of the detector is $\sim 50\%$ for detecting α particles, which is because of the shallow implantation of the recoils in the detector $\sim (1 - 10)$ μm from the surface.

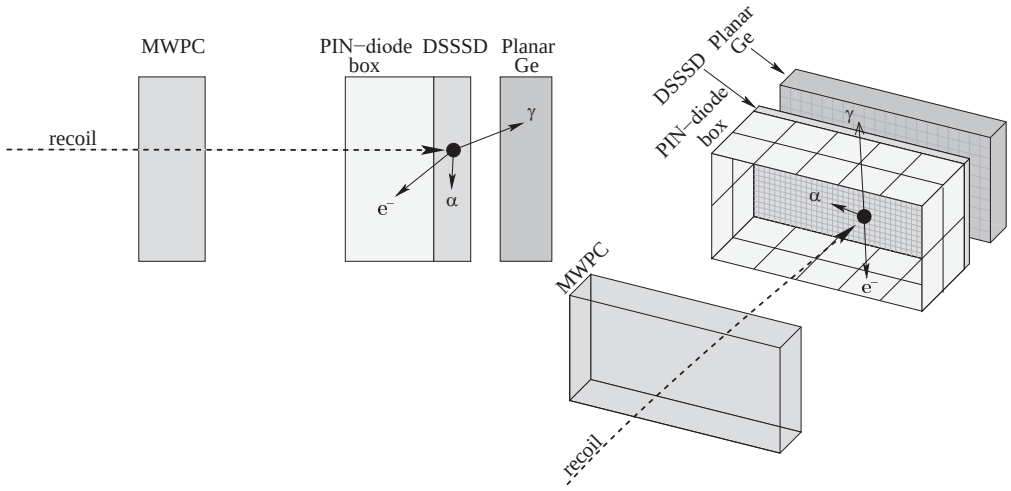

Figure 3.6: A schematic drawing of the GREAT spectrometer and its components.

Planar Germanium Detector

The PGD was placed directly downstream behind the DSSSD detector with a 10 mm gap separating the two detectors. The detector is a double-sided strip detector with a total active area of 120 mm × 60 mm. The thickness of the detector is 15 mm, containing 24 vertical (facing the DSSSD) × 12 horizontal (on the backside of the detector) strips that lead to a strip pitch of 5 mm on each of the two faces for position sensitive of the recoil subsequent decays. Therefore, a correlation between the events [2] detected in the detector and the events in other detectors of GREAT can be established. The detector is designed to detect X-rays, low-energy γ rays, and high-energy β particles ($E_\beta \gg 2$ MeV). Figure 3.6 shows the position of the detector relative to the DSSSD.

Segmented Clover Detectors

The high-energy γ rays detected in the focal plane are measured using large volume Clover germanium detectors. Three Clovers are mounted in the GREAT spectrometer, of which one is located on the top while the other two are placed on the sides of the spectrometer chamber. The detector has better energy efficiency at energies higher than 200 keV than PGD. With the aim of improving the signal-to-noise ratio, a BGO Compton suppression shield surrounds each of the Clovers, similar to the Clover detectors in JUROGAM II. Jointly, the Clovers and PGD are used to identify the delayed and isomeric γ-ray transitions at the focal plane of the RITU.

3.3 Calibration of the Detectors

Calibration of the detectors is essential for ensuring that the outcome energy values match the actual ones. In the following section, energy and efficiency calibrations are discussed.

[2] The term event is used to describe the detection of a decay using JUROGAM II and GREAT spectrometers.

3.3.1 Energy Calibration

In order to identify an unknown energy transition, we must calibrate the detectors using well-known energy transitions. The output signals of the detector are at a voltage that is proportional to the deposited energy detected. The quadratic equation 3.4 relates the channel number of the ADC to energy in units of eV:

$$E = a + bx + cx^2 \,, \tag{3.4}$$

where a, b, and c are the fitting parameters and x is the channel number. The resulting energy does not correspond to the real energy unless it has been calibrated to a known reference.

The JUROGAM II array and the focal plane germanium detectors were calibrated 'externally' using a compound source ^{133}Ba^{152}Eu as a stationary γ-ray emitter. The ^{133}Ba covers a range of gammas - from 80 keV to 384 keV [SDW77]. The energy range is narrow, but it is important since it covers a large variation in the energy efficiency of JUROGAM II. The mother ^{152}Eu nucleus β-decays into excited states of ^{152}Sm and ^{152}Gd nuclei daughters [Gri+02]. The origin of the γ rays arises from the β decay of the nucleus to the excited states in ^{133}Cs. The ^{152}Eu γ source has a wide range coverage (122–1408 keV).

Calibrating the DSSSD detectors at the focal plane required the implementation of two procedures. The first method was calibrating the detectors 'externally' using a stationary triple-alpha source (^{239}Pu, ^{241}Am, and ^{244}Cm). Since there is a dead layer on the DSSSD detectors, an 'energy loss' is present in the surface of the detectors. Therefore, the detected energy is lower than the actual energy. The external calibration was used in the online analysis during the experiment. The error in the calibration was covered by adding the missing energy manually in the analysis code.

An 'internal' calibration was used in the offline analysis. Different nuclei were implanted in DSSSD after being deflected in the RITU. These unstable nuclei decay inside the DSSSD, and the measured α energies represent the real ones. These

reference α particles were identified using their energies and by using the RDT technique (section 3.6.1). The main benefits of using internal calibration is that the calibration energies are higher and cover a wider region of interest as compared to external calibration.

3.3.2 Efficiency Calibration

The detected γ rays do not represent the number of emitted decays. Therefore, it is essential to calculate the efficiency of the detectors for accurate measurements. The absolute photopeak efficiency at a given energy, ε_{abs}, is defined as the ratio between the recorded number of γ rays, N_{FPE}, and the emitted γ rays, $N(E)$, from the radioactive source, such that

$$\varepsilon_{abs} = \frac{N_{FPE}}{N(E)} \times 100 \tag{3.5}$$

Knowing the activity of the reference source (A_{ref}), the duration of the measurement (Δt), and the tabulated branching ratio of the transition (I_γ), Equation 3.5 can be rewritten as

$$\varepsilon_{abs} = \frac{N_{FEP}}{A_{ref} I_\gamma \Delta t} \times 100 \tag{3.6}$$

The determination of the absolute efficiency of JUROGAM II was established by placing a compound radioactive source ^{133}Ba^{152}Eu at the target position.

As for the focal plane germanium detectors, it not possible to calculate the efficiency using a stationary source, as it requires placing the source inside the DSSSD detector in order to simulate the implantation of the recoils. Therefore, Monte Carlo simulations have been performed to calculate the efficiency of the focal plane germanium detectors [And+04]. The result of the simulation is shown in Fig. 3.7.

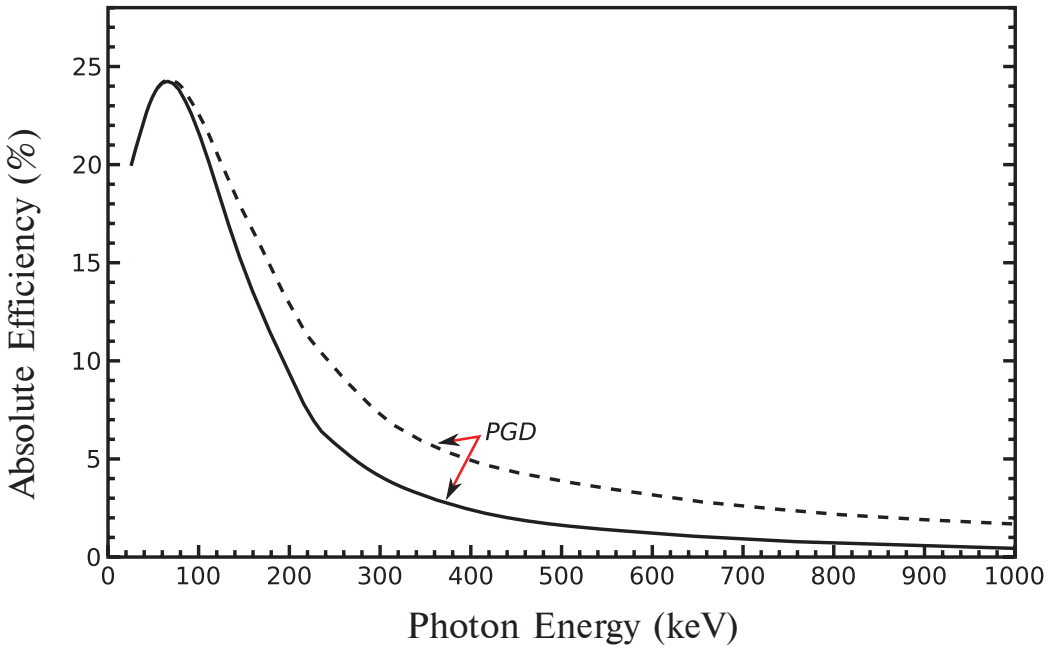

Figure 3.7: The absolute efficiency as a function of energy of the GREAT spectrometer using GEANT Monte Carlo simulations. The solid and dashed lines are for the data with and without 'add-back' modes, respectively. The figure is recreated from [And+04].

3.4 The Non-Relativistic Doppler Effect

The fusion-evaporation nuclei products at the target position moves at high velocity. Therefore, the measured gamma rays emitted from excited states of the nuclei at this point experience what is called the 'Doppler effect'. The shifted photon E'_γ, which is emitted from the compound nucleus that is traveling at velocity v and is detected at an angle θ with respect to the beam direction is calculated as

$$E'_\gamma = E_\gamma \frac{\sqrt{1-\beta^2}}{1-\beta cos(\theta)}\,, \tag{3.7}$$

where E_γ is the true photon energy and $\beta = v/c$. Equation 3.7 can be reduced to the non-relativistic form:

$$E'_\gamma \approx E_\gamma[1+\beta cos(\theta)] \quad \text{for} \quad c \gg v \tag{3.8}$$

In our experiment, the β value was derived using two methods. The first was by using the software 'RITU' which the extracted value of β to be 0.04. The second

and more accurate method used in the present work was plotting $cos(\theta)$ versus $(E'_\gamma - E_\gamma)/E_\gamma$. Therefore, the gradient of the plot is β. The measured value from the gradient is 0.04249.

3.5 Total Data Read-out

In standard data acquisition systems (DAQ), triggered signals from the detectors are collected after placing a defined time gate. This could lead to missing useful events since there is a dead-time formed in the system during which no data is registered in a given period. The conventional trigger method is useful when the triggering rate is low or the desired events have a higher occurrence rate as compared to the background events. On the other hand, if the high-triggering event rate or the desired events are low as compared to the background events, which leads to the acquisition system missing useful events that are not recorded.

Total **D**ata **R**ead-out (TDR) [Laz+01] overcomes the limitation of the conventional data acquisition systems. The TDR system (the one used in the present work) records all the signals from all the detectors separately without the requiring the use of a triggering condition. The signals are then assigned a time stamp from the DAQ 100 MHz clock, leading to a precision of 10 ns.

Events are then reconstructed in the software, where correlations and trigger conditions can be performed. The main advantage of this is that the long period of the time-triggering condition can occur without missing meaningful events within this time condition.

Figure 3.8 presents the logic behind the TDR method. The signals from all the detectors are converted to energy and time stamps using shaping amplifiers and constant fraction discriminators (CFDs). The output energy and time signals are then fed to the analog-to-digital converter (ADC) cards, where the signals are read and a time-stamp is applied. The ADC cards data are synchronised by the metronome unit. The collection and merging units arrange the time-stamped events from all the detectors by time according to the 100 MHz clock. Reconstructing the

data is the duty of the event builder, where it will pre-filter the data as per the pre-set software trigger condition and set temporal and spatial conditions.

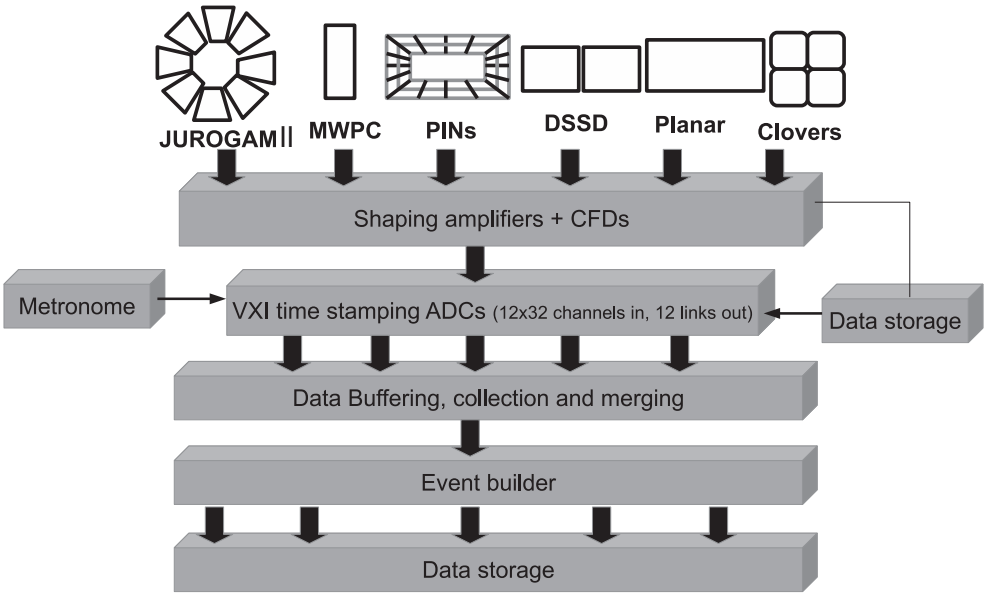

Figure 3.8: A schematic diagram of the GREAT TDR system's electronics and data acquisition. The figure is reproduced from [Ali14] in which the logical sequence adopted from [Laz+01].

3.6 Analysis Techniques

A range of techniques were used in this work. These are detailed in the following subsections.

3.6.1 Recoil-Decay Tagging Technique

The study of the nuclei produced from the fusion evaporation reaction is challenging. The various possible exit channels makes establishing correlations between the delayed focal plane events and the prompt target position events a complex procedure.

The **R**ecoil-**D**ecay **T**agging (RDT) method [Pau+95] is a technique used to create a series of logic chains and connect the events detected from GREAT and JUROGAM II. Figure 3.9 illustrates the logic operation of the method, where the goal is to distinguish between a recoil or a decay event being detected in the DSSSD based on its adherence to the given conditions, such as the energy and time limit wherein it is detected. When the signal has been confirmed, the correlations can be made between the decay of the desired nucleus and any other decay in the system (JUROGAM II and GREAT).

Two examinations need to be performed before the RDT technique is established:

(i) Confirmation of a recoil event detected in a DSSSD pixel.
(ii) Confirmation of a decay event detected in the same DSSSD pixel.

For the first point, it is important to distinguish between a recoil and a scattered beam detected in the DSSSDs. A recoil is transmitted through the RITU and detected in the MWPC, where energy loss and time-of-flight (between the MWPC and the DSSSD) are recorded. The recoil is then implanted into the DSSSD. The same goes for the scattered beam. The difference is that the recoils (usually) have a higher Z numbers than the scatter beam. Therefore, it takes more time for them to travel from the formation area to the DSSSD. Moreover, since the recoils have higher Z numbers, more energy is deposited in the MWPC than the unreacted beam. As noted in Section 3.2.3, the recoils are treated differently from the scattered beam by placing a two-dimensional gate on a two-dimensional plot of the energy loss versus the time-of-flight detected in the MWPC and implanted into the DSSSDs. The recoil identification is illustrated in Figure 3.10.

Regarding the second point, identifying a nucleus decay is done by detecting an event in the DSSSDs followed by another event in the same detector pixel within a finite time range, without observing an event simultaneously in the MWPC.

To this point, all the information needed is prepared to begin processing the RDT method. A three-dimensional array called ‘tagger’ is used by the software

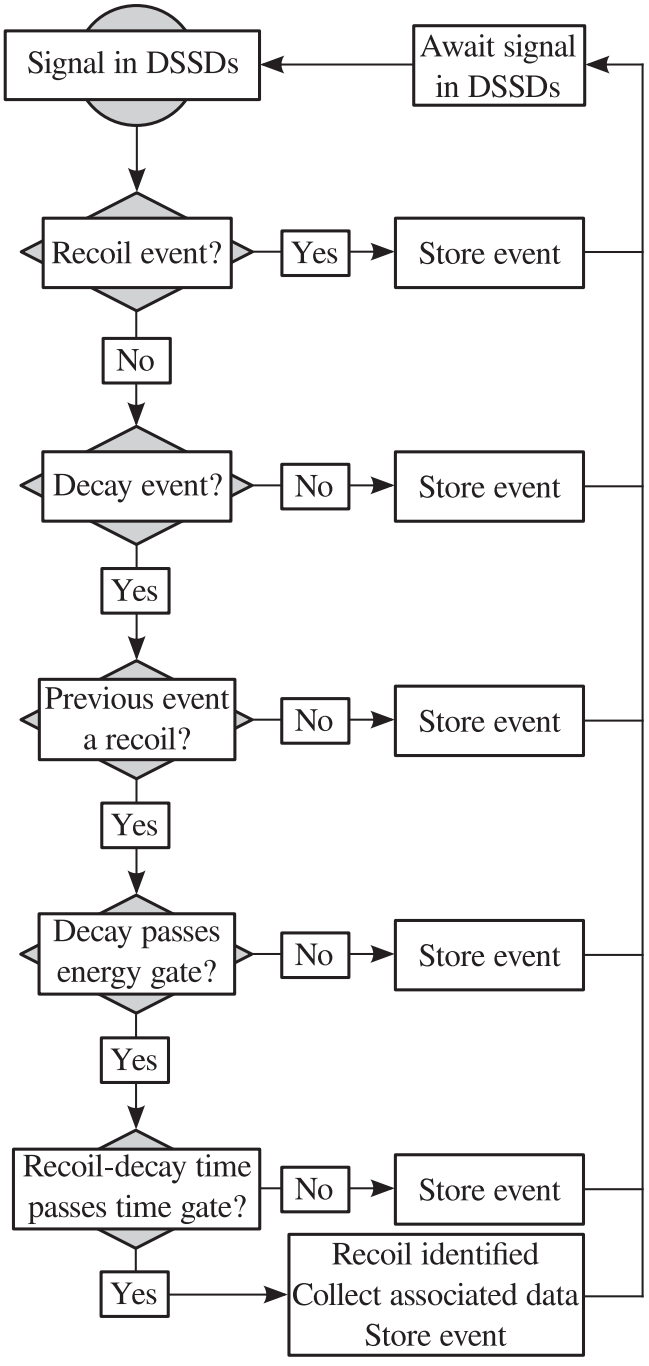

Figure 3.9: Flowchart shows the logic behind the RDT technique. The processed events are placed in the tagger as illustrated in Figure 3.11. The figure is from [Car12].

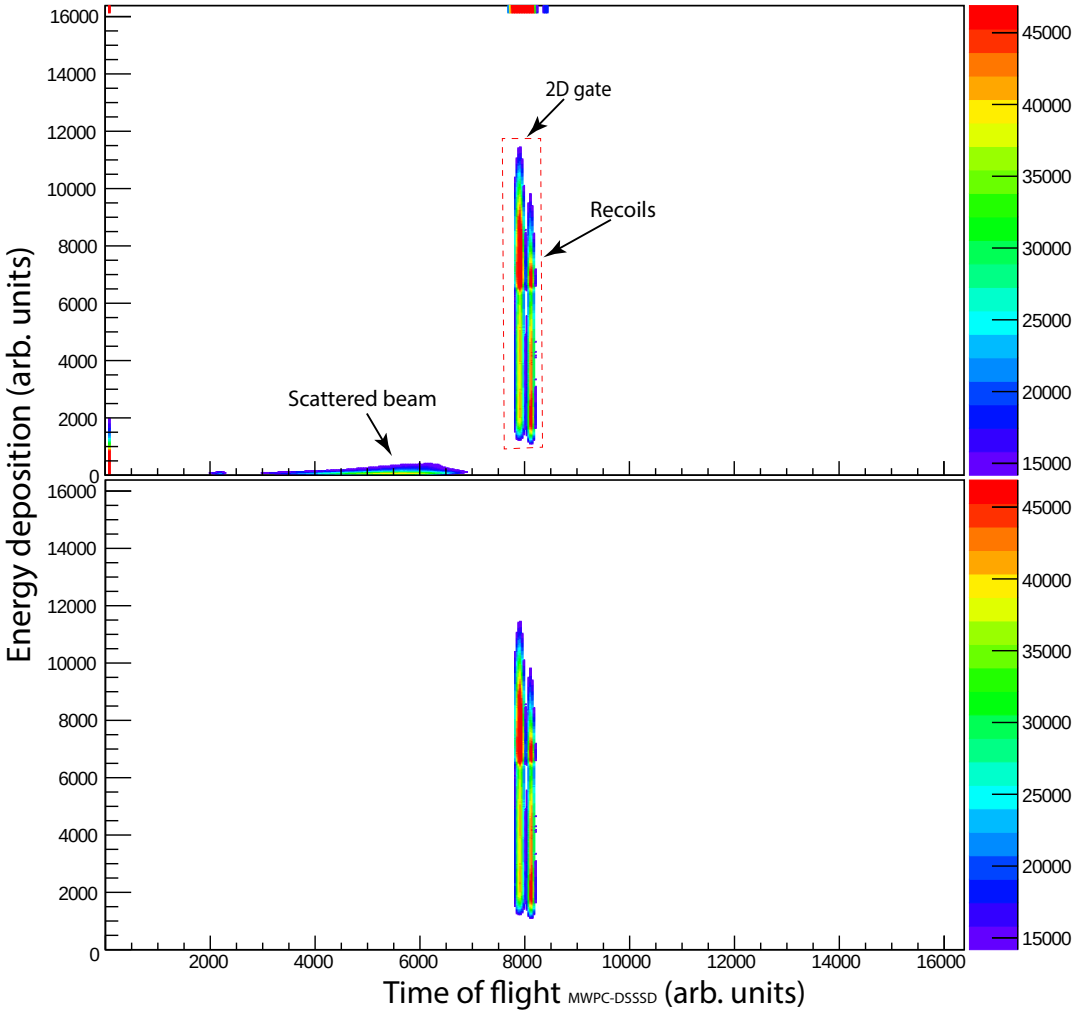

Figure 3.10: (upper panel) Two dimensional matrix of energy loss versus the time-of-flight detected in the MWPC and implanted in the DSSSD. (lower panel) The selection of the recoil after placing a two-dimensional gate.

package GRAIN, where two of the dimensions correspond to the DSSSD pixel (x and y) and the third dimension represents the time t. When an event is detected in a DSSSD pixel, it is identified (recoil or a decay) and stored in the tagger for a pre-defined time. Usually, the pre-defined time is set to $3\times t_{1/2}$, where $t_{1/2}$ is the half-life of the state. The subsequent detected events will be identified and stored in the tagger as well. Once a decay is detected in the same DSSSD pixel within a certain time, the energy and time gates are applied prior to sorting the event. Figure 3.11 illustrates the operation used in the tagger. Once the recoil-decay correlation is confirmed, prompt γ decays at JUROGAM II can be selected from the data.

The above description can be modified. For example, the correlation can be

between an isomeric γ decay (detected in the focal plane Clovers or the PGD) and prompt γ transition, which is called **I**someric **D**ecay **T**agging (IDT) [Sch+03].

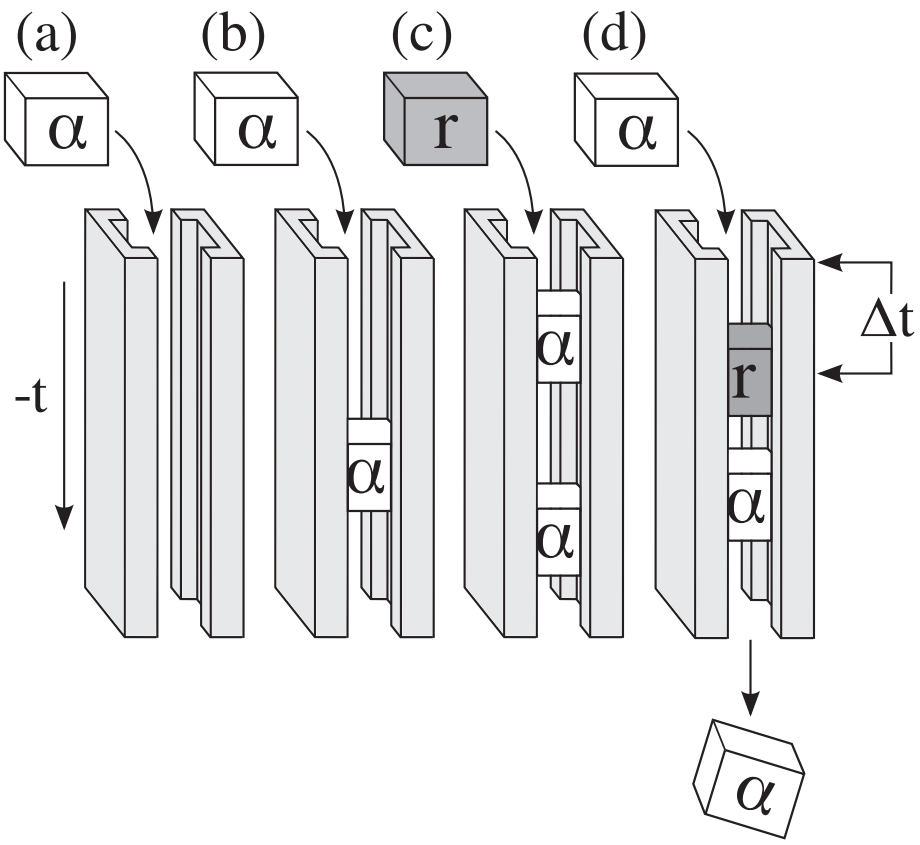

Figure 3.11: The logic of correlating events in one DSSSD pixel using the three-dimensional tagger. (a) A decay is identified and stored in the tagger. (b) Another event is detected and stored in the tagger. As the previous event is a decay, it is only stored. (c) A recoil is detected and identified and stored in the tagger. (d) A decay event is detected. As the previous event is a recoil, time and energy gates are applied to correlate the decay with the recoil. The figure adopted from [Car12].

3.6.2 Sorting the Raw Data

The GRAIN software package [Rah08] was used to sort the raw data from the TDR stream in order to construct the final histograms. The software is java-based and allows the user to write and modify their own code in order to build their desired meaningful events. The GRAIN software was used on line and off line to analyse the data.

The software allows the user to modify two parameters- the *trigger width*

and the *trigger delay*- in units of the clock cycle or 'ticks' where one tick is 10 ns. The trigger delay offsets the starting point of the triggering, while the size of the trigger is determined by the trigger width initiated from the starting value of the trigger delay up to a maximum time of *trigger delay+trigger width* ticks. Increasing the value of the trigger width leads the detector observing the isomeric transition but simultaneously detecting more random events.

3.6.3 Background Subtractions

The hostile environment at the target position produces a tremendous amount of background radiation that needed to be considered and removed from the measured γ-ray energy spectra. As mentioned earlier in Section 3.2.1, Anti-Compton Bismuth Germanium Oxide (BGO) scintillator detectors surrounded the High Purity Germanium detector in order to increase the peak-to-background ratio. The BGO shield is not enough to remove the background events from the spectrum. The primary method used in this work to subtract the background events from the desired spectra can be defined as [Sma13]

$$S_p = S_t - B \,, \tag{3.9}$$

were S_p is the resulted spectrum, S_t is the histogram containing the resulted data, and B is the scaled background spectrum. The scaled background can be calculated as

$$B = S_b . \frac{N_t b_g}{N_b} \,, \tag{3.10}$$

where S_b is the background spectrum, N_t is the total counts in the gated spectrum S_t, b_g is the fraction of the background events in the gated spectrum, and N_b is the total count in the spectrum S_b. The background fraction b_g is calculated as

$$b_g = 1 - \frac{A_{gated}}{A_{sum}} \,, \tag{3.11}$$

where A_{gated} is the peak area within the gate, and A_{sum} is the peak area that includes the background beneath it.

Chapter 4

Decay Studies of ^{178}Au

In this study, the ^{178}Au nucleus was produced via the fusion-evaporation reaction, ^{92}Mo(^{88}Sr,pn)^{178}Au. Excited states in ^{174}Ir and ^{178}Au were studied along with the α decay of their long-lived ground and isomeric states. In the following three chapters, the analysis of experimental data taken in the experiment at JYFL will be presented. In particular, Chapter 5 will deal with the alpha decay of two long-lived states (ground and isomer) in ^{178}Au. Chapter 6 will discuss the identification of two sub-microsecond isomeric states, build on top of the above mentioned alpha-decaying states in ^{178}Au. Finally, Chapter 7 will present the by-product alpha-decay data for ^{174}Ir, being the daughter of ^{178}Au after alpha decay.

4.1 The Complementary IS534 ISOLDE Experiment on ^{178}Au

As mentioned in Section 1.1, our complementary laser spectroscopy IS534 experiment [Cub17], which was performed at ISOLDE CERN facility, provided the first proof of the existence of two alpha-decaying isomers in ^{178}Au. A brief overview of the experiment is provided next. The ^{178}Au nuclei were produced by bombarding a thick target of UC_x with 1.4 GeV protons. The spallation reactions produced a wide range of different nuclei including Au. The **R**esonance **I**onisation **L**aser **I**on **S**ource (RILIS) [Mis+93; Fed+00] comes to action, where multi-step resonant photo-ionisation process took place to produce an ion beam of ^{178}Au in 1^+ charge state. The laser-ionized ions were then accelerated by an electrostatic potential of 30–60 kV. The ion beam was then fed to on-line mass ISOLDE, to select specific mass, A=178, in this case (there are no surface-ionized admixtures in this case, ^{178}Tl is very weak, to interfere). Subsequently, the beam was delivered to a decay station called Windmill. The conversion electrons, β and α particles, were detected by four silicon detectors, while two germanium detectors detect the γ rays. Based on complementary mass-measurements with ISOLTRAP, the masses of both alpha-decaying states could be measured, which allowed to determine their relative positions, and thus to assign the lower-lying one as the ground state, and the other one as the isomeric states. In this work, they will be denoted as ^{178gs}Au and ^{178is}Au, respectively.

Figure 4.1 shows the decay scheme for ^{178,gs,is}Au deduced from the IS534 experiment [Cub17]. The measured half-lives were 3.4 s and 2.7 s for the ground and isomeric states, respectively. The main α-decay transitions from ^{178gs}Au are at 5922 keV and 5843 keV, while several α-γ coincidences are detected as well; such as 5840-90.4 keV, 5811-116.0 keV and 5753-175.0 keV. As for ^{178is}Au, several fine structure decays, feeding excited states in the daughter ^{174}Ir were observed. The findings from the IS534 experiment were further discussed in the following sections. The author of the present work has also participated in these experiments at ISOLDE.

A much higher statistics was collected in our experiment for ^{178}Au at RITU in comparison to ISOLDE study. Together with much more efficient detection sys-

tem for γ-rays in this study, improved data could be obtained, as shown in Chapter 4.4.1.

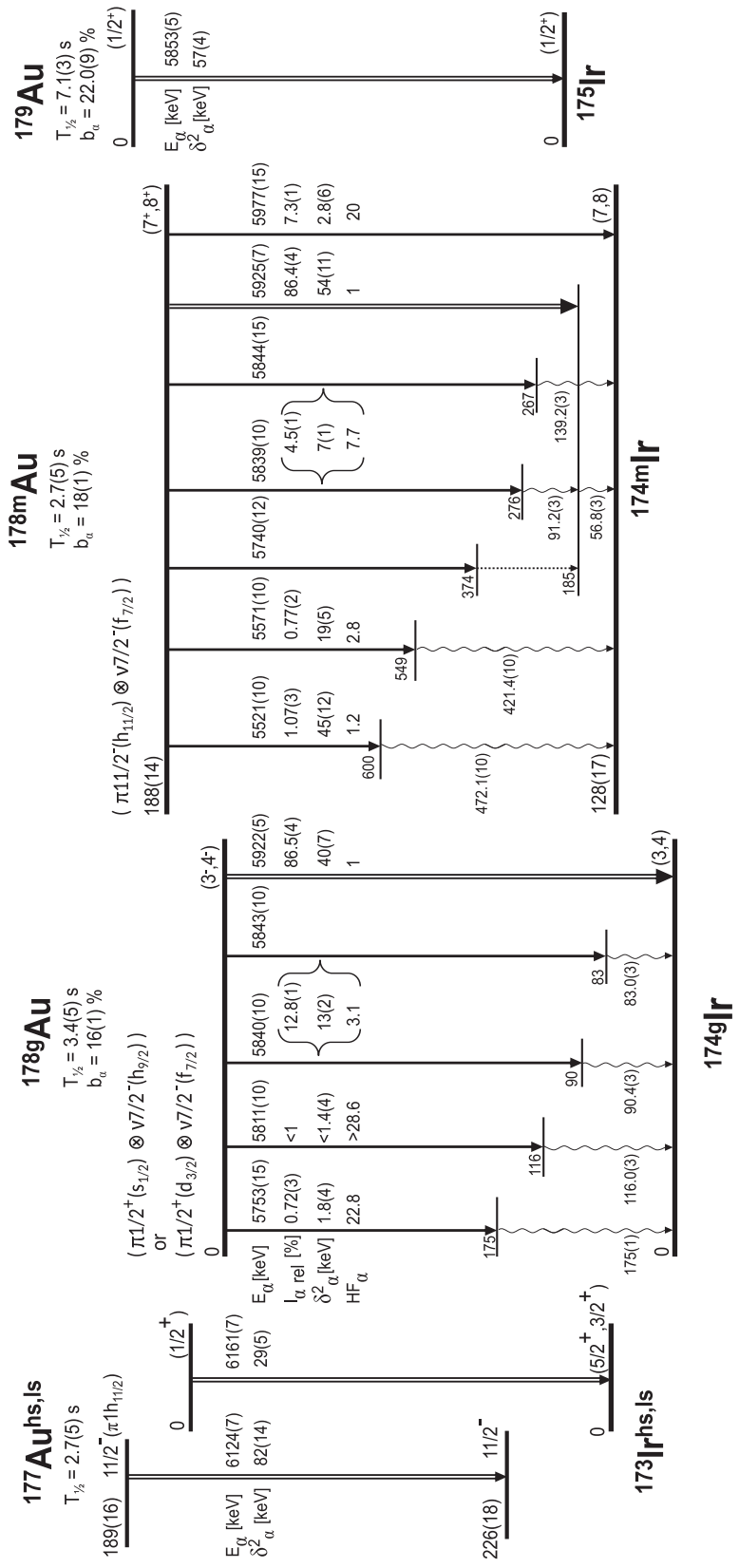

Figure 4.1: Decay scheme deduced for ^{178gs,is}Au from [Cub17]. Shown are the α-decay energies, E_α, relative intensities, $I_{\alpha,rel}$, reduced α-decay widths, δ^2 and hindrance factors , HF_α.

4.2 The Production of ^{178}Au at JYFL

The experiment was conducted at the Accelerator Laboratory of the University of Jyväskylä, Finland, in the period of 5th–15th June 2015. A beam of ^{88}Sr provided by the K-130 cyclotron with intensity in the range of $\sim$ 30-140 pnA impinged on a target foil of ^{92}Mo (0.6-mg/cm^2-thickness), mounted on a rotating wheel at the center of JUROGAM II (JR). The prompt γ-rays were detected at the target position using JR array after the fusion reaction.

The mixture of unreacted beam and the recoils then passes through RITU, where recoils are separated in flight from the beam and implanted into one of the two DSSSDs. Recoiling nuclei are distinguished from the scattered beam by measuring the energy loss and time-of-flight information.

The total data readout (TDR) acquisition system processed the signals from all the detectors individually and assigned a time-stamp for each signal with an accuracy of 10 ns. GRAIN [Rah08] and ROOT [BR97] software packages were used to analyse and process the data.

4.3 Singles Alpha Decay

As mentioned in Section 3.6.1, a dedicated procedure is required to distinguish a decay event in the DSSSD from implantation of a recoil or a scattered beam particle. A decay is identified by detecting an event in the DSSSD without observing any coincident (within finite time range) signal in MWPC. On the other hand, a recoil is identified if an event is detected in the MWPC in coincidence with a signal in the DSSSD. Figure 3.10 shows the two-dimensional, ToF vs ΔE, plot and the two-dimensional gate used to select the recoils. The two bumps in the recoils region resulted from slight difference of timing signals between the two DSSSDs.

Figure 4.2 shows the singles α-decay spectrum overlapped with a recoil-gated α spectrum detected in the focal plane DSSSDs within 8 seconds of the implantation of a recoil into the same DSSSD pixel. The time condition was chosen to be 3$\times$

the measured α-decay half-life of ^{178}Au ground state, $T_{1/2} = 2.7$ s. Many α-decay peaks are seen in the spectrum originating from different evaporation channels of the studied reaction. The three main reported α decays from ^{178}Au [Kel+86] are seen in the spectrum with energies of 5850, 5930 and 5980 keV. The recoil-gated condition did not enhance the ^{178}Au alphas due to the high average implantation rate and the relatively long half-lives of the nuclei which resulted in a large number of random recoil-alpha correlations. Despite this, the recoil-alpha correlations could still be used for some of the data analysis, see examples further in the text. Unlike the ISOLDE experiment, our study cannot physically separate the two alpha-decaying states in ^{178}Au. Therefore, we will rely on the measured α-γ coincidence data for their distinction and rely on decay scheme of ^{178gs,is}Au from ISOLDE experiment.

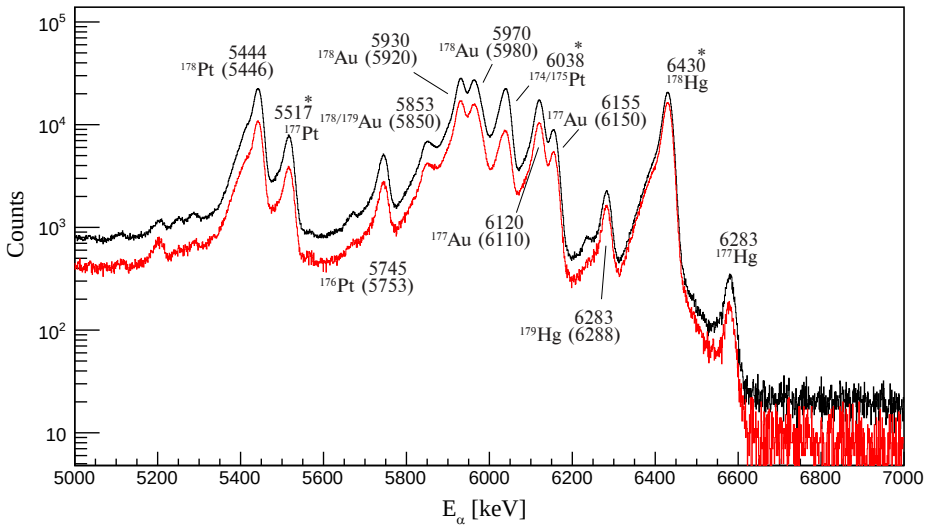

Figure 4.2: Singles α-decay spectrum (black) overlapped with a recoil-gated α spectrum (red) detected in the focal plane DSSSDs within 8 seconds of the implantation of a recoil. Measured energies of the peaks are marked where the energies in parentheses are from the literature. The asterisk shows the α-decay energies used for the off-line DSSSD energy calibration.

4.4 Fine Structure Alpha Decay Analysis

The RITU focal plane detection system allows the investigation of fine structure alpha decays of ^{178}Au and ^{174}Ir. Decay of ^{178}Au and ^{174}Ir. Figure 4.3 (a) shows the recoil-gated α-decay spectrum, where the α lines are marked with energies and the isotope they originate from, whereas Figures 4.3 (b) and (c) illustrate the prompt α-γ coincidence matrix detected between the signals in the DSSSD and γ rays observed

in PGD or Clover detectors, respectively. DSSSD and correlated to PGD and the Clover detectors, respectively. In Figure 4.3 (c), a bigger dot size was used for better identification of the groups.

A proper prompt α-γ time gate has to be used in order to ensure that most of the time random events are removed from the analysis. Figure 4.4 demonstrates the examples of time distributions DSSSD-PGD and DSSSD-Clover for several known α-γ coincident pairs, seen in Figure 4.3 (b) and (c). The time distribution of the Clovers is somewhat broader for most of the chosen γ rays. The time gates of 200 ns $\leq \Delta t(DSSSD\text{-}PGD) \leq$ 270 ns and 210 ns $\leq \Delta t(DSSSD\text{-}Clover) \leq$ 310 ns were chosen as the prompt gates, respectively. Analysing Figure 4.3 (b) and (c) shows the presence of a rather larger background even after placing a narrow α-γ time gate.

For a better representation, Figure 4.3 (b) is reproduced in Figure 4.5 with a condition of suppression single counts per channel, which helps to visually reduce the background and enhance the observation of α-γ groups.

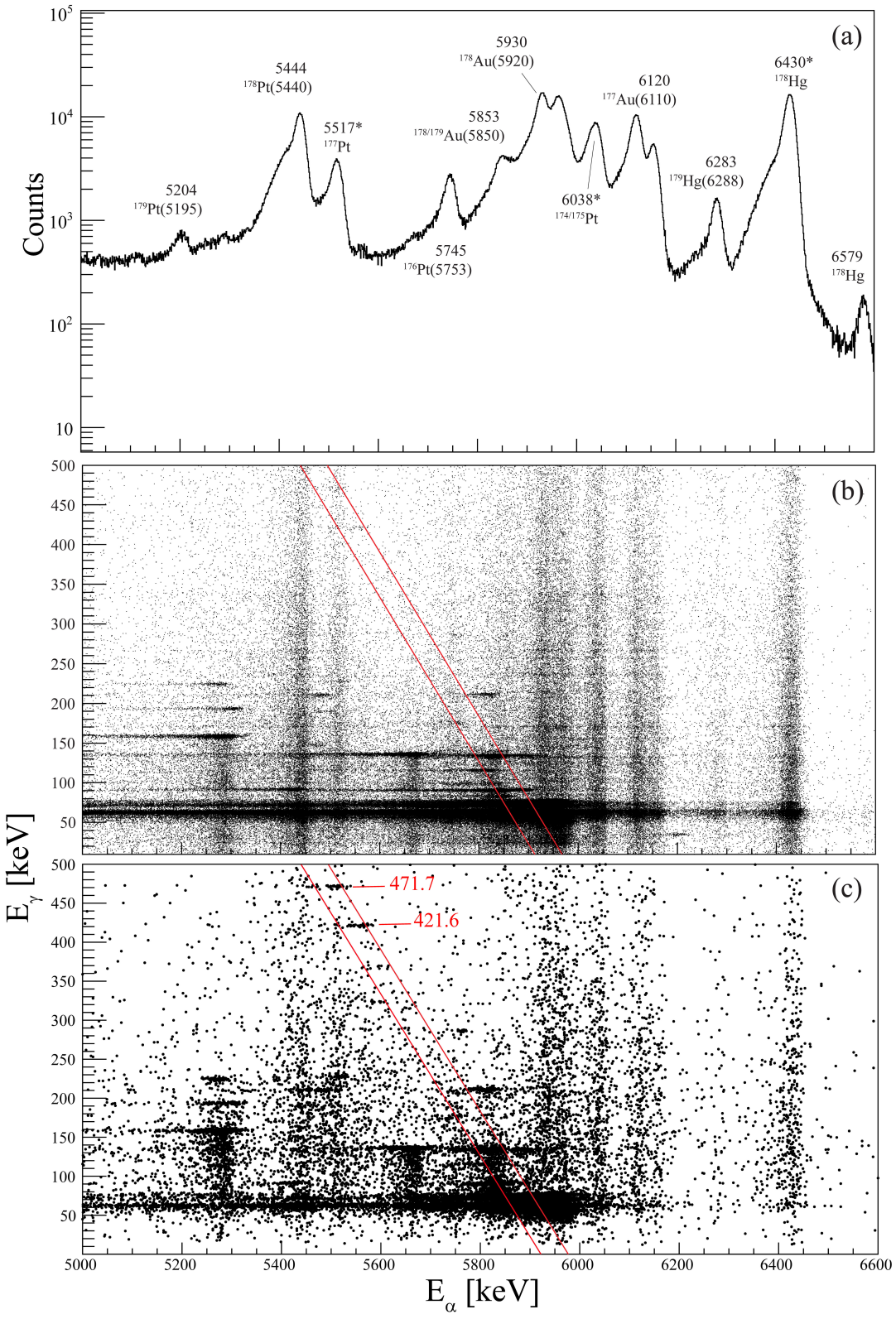

Figure 4.3: Singles α-decay energies and α-γ coincidence spectra. The red lines represent the region of constant $Q_{\alpha,tot}$ (more details are shown in Figure 4.5). (a) Singles recoil-gated α decay measured in the DSSSD within 8 s of a recoil. (b) α-γ matrix for DSSSD-PGD events with time condition ΔT(α-γ)=200-270 ns. (c) α-γ matrix for DSSSD-Clover events with time condition ΔT(α-γ)=210-310 ns. See text for details.

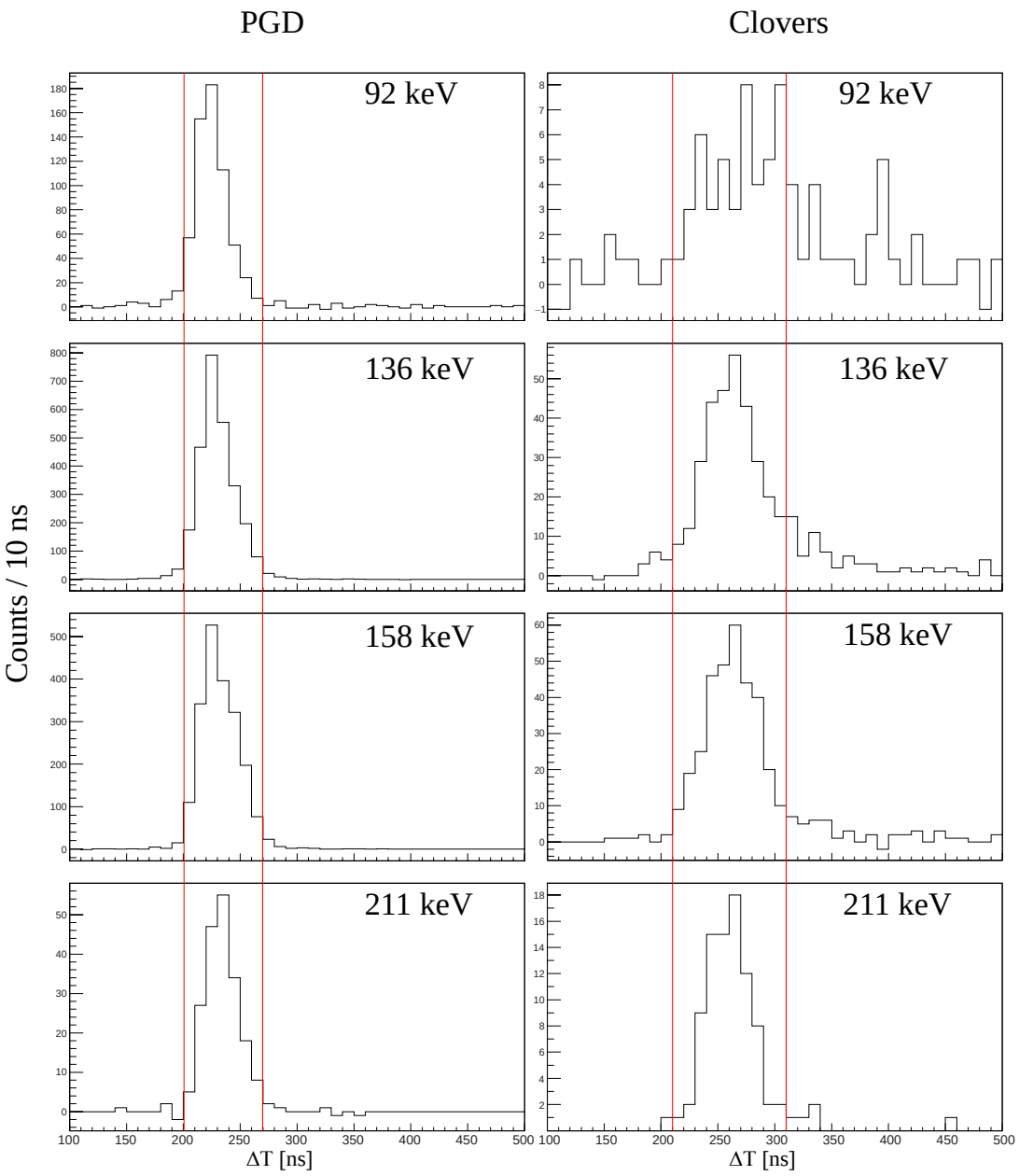

Figure 4.4: Comparison of the time distribution for the PGD and the Cloves for some of the known prompt γ-ray transitions (see Figure 4.5).

4.4.1 Ground State Decay of ^{178}Au

As aforementioned, it was not possible to physically separate the production of ground and isomeric states in this work. In our study, based on the analysis of Figure 4.5, we confirmed the presence of 4 α-γ coincidence groups, assigned to ^{178gs}Au by the

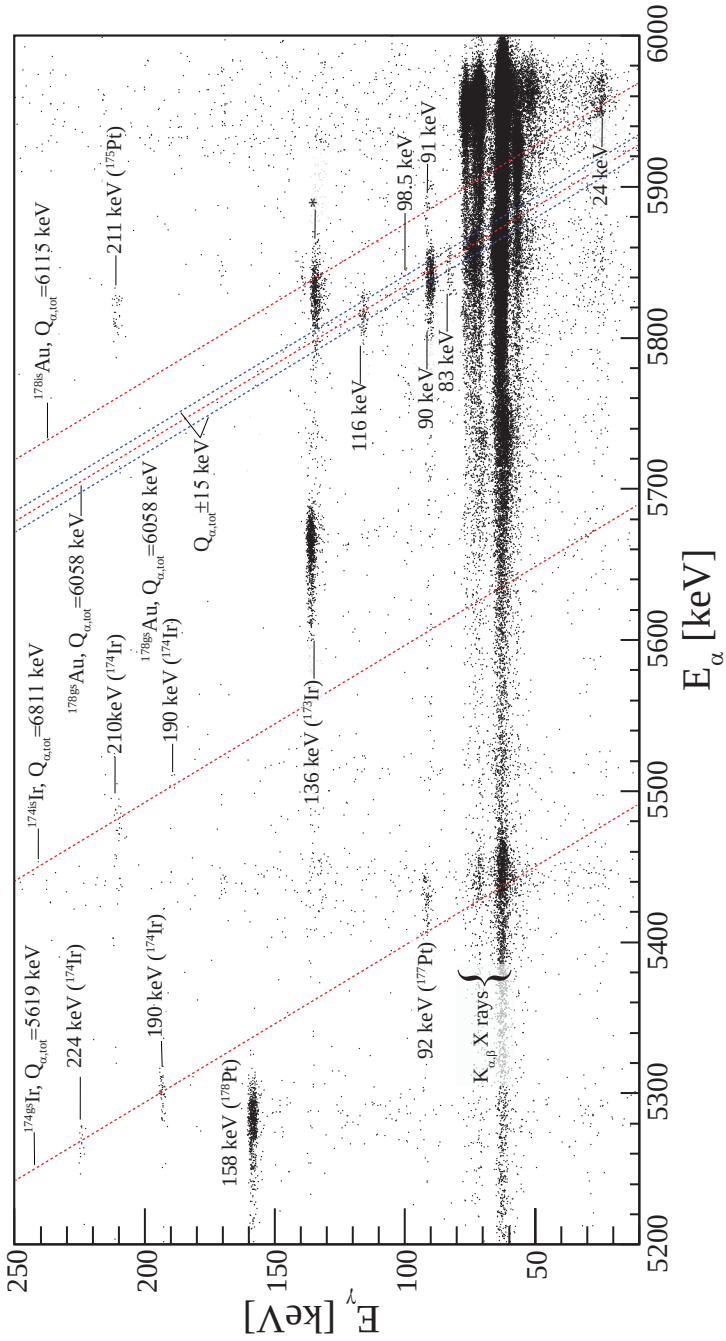

Figure 4.5: Reproduction of Figure 4.3 (b) where any single event was disregarded for better presentation. The 4 red dashed lines represent the regions of constant Q_α, tot constant line for f.s. ^{174gs,is}Ir and ^{178gs,is}Au from the left to the right, respectively. The time gate condition used is ΔT(α-γ)=200-270 ns.

ISOLDE experiment: 5848(4)–83.0(3) keV, 5840(10)–90.3(2) keV, 5812(4)–115.9(1) keV and 5758(8)–175.1(2) keV. Figure 4.6 (a-e) illustrates α decays in coincidence with 83.0, 90.3, 98.5, 115.9 and 175.1 keV γ rays.

By referring to the decay scheme in Figure 4.1, it can be observed that the

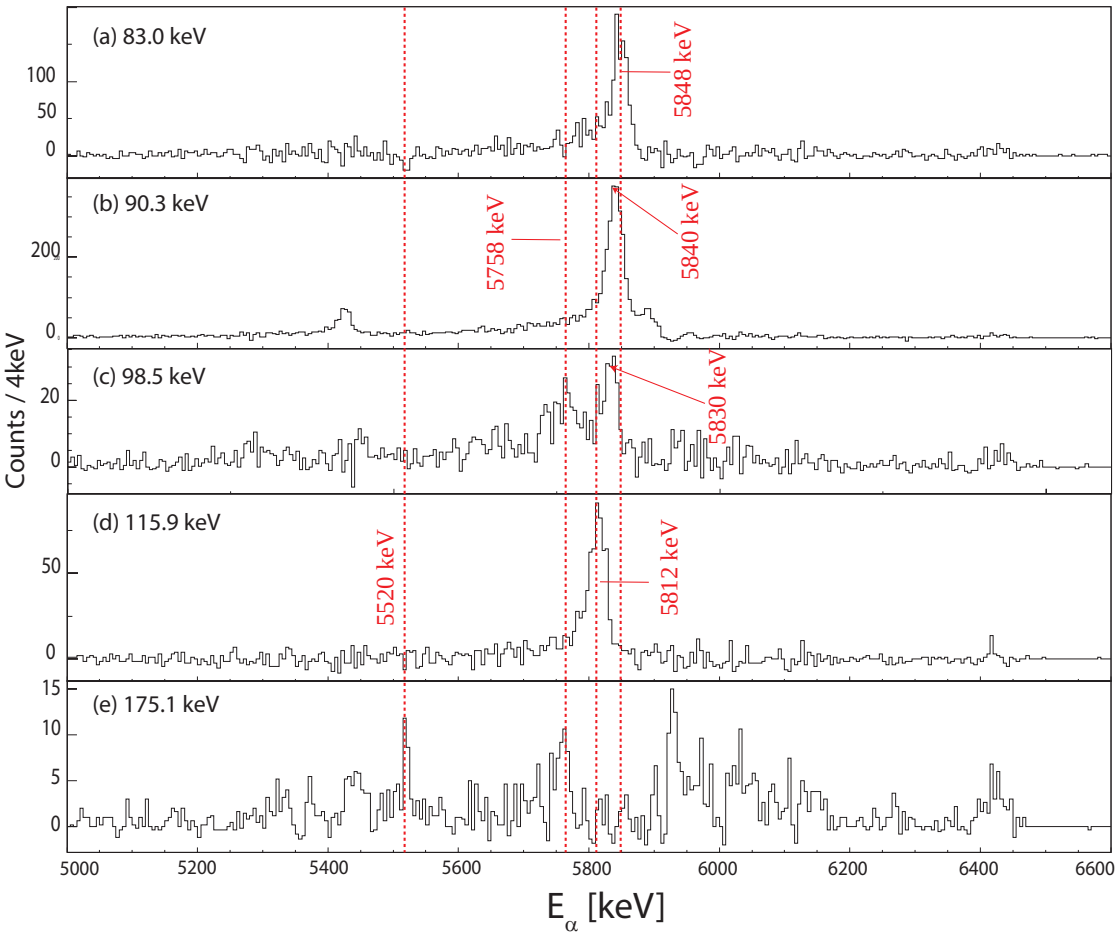

Figure 4.6: E_α projections spectra from the α-γ matrix of ^{178gs}Au illustrated in Figure 4.5 gated on E_γ = (a) 83.0, (b) 90.3, (c) 98.5, (d) 115.9 and (e) 175.1 keV. The E_γ gating condition used in the alpha-gamma matrix is ± 1.5 keV. The spectra are background subtracted.

5922 keV is the strongest α decay of ^{178gs}Au. Therefore, one could justify if these groups belong to the fine-structure decay of the same state in ^{178}Au, by checking their total Q_α-value; $Q_{\alpha,tot}$ should be close to or the same (within energy uncertainty) as the $Q_\alpha = 6058$ keV for the highest energy g.s.→g.s. state 5922 keV α decay. The $Q_{\alpha,tot}$ is calculated as follows:

$$Q_{\alpha,tot} = Q_\alpha + \sum_{i=1}^{n} E_\gamma(i) \tag{4.1}$$

where Q_α is the net energy released in the particular f.s. alpha decay to an excited state, and the second term is the total γ-ray energies following the alpha decay from this state. Table 4.1 demonstrates the calculated $Q_{\alpha,tot}$ values of these α-γ

coincidence groups.

E_α [keV]	E_γ [keV]	$Q_{\alpha,tot}$ [keV]
5922(4)	0	6058(4)
5848(4)	83.0(3)	6065(4)
5840(10)	90.3(2)	6064(10)
5830(9)	98.5(3)	6064(9)
5812(4)	115.9(1)	6062(4)
5758(8)	175.1(2)	6065(8)

Table 4.1: The $Q_{\alpha,tot}$ values for α-γ groups assigned to ^{178gs}Au. The constant $Q_{\alpha,tot}$ signify that all α decays originate from the same state in ^{178}Au.

Figure 4.7 illustrates a projection of the α-γ matrix from Figure 4.5 to the γ-ray axis of the region between the two dotted red lines limited by $Q_{\alpha,tot} \pm 15$ keV of the ground state in order to identify the single-step γ-ray transition. The deduced decay scheme of ^{178gs}Au from this work is shown in Figure 4.8. The red coloured lines represent the α transitions seen for the first time, whereas the dashed wavy lines illustrate the unseen γ transitions. Both the much higher statistics and higher γ-ray efficiency for the RITU experiment in comparison to ISOLDE are the reasons for observation of improved f.s. data in our study. Table 4.2 displays a comparison between JYFL and ISOLDE data regarding the number of counts for selected α-γ groups. We can conclude from the results that JYFL's data contain $\sim$ 10-20 times higher statistics than ISOLDE's. The energy resolution of PGD and the Clovers are similar to each other. Another noticeable feature seen in the table is that the Clovers' efficiency at high energy is much higher than that of PGD. This is in agreement with efficiency simulations with GEANT in study [And+04].

In parallel with reducing the time random events from the spectrum by applying a prompt time gate, another method used to suppress the background in

Table 4.2: Statistical comparison for the selected α-γ coincidence groups for DSSSD-PGD and DSSSD-Clover from the RITU run and for Silicon-Ge detectors from the ISOLDE study. The detectors resolution for ISOLDE's experiment is not given.

E_γ	PGD FWHM (keV)	Clover FWHM (keV)	PGD counts	Clover counts	ISOLDE counts
472	2.8	2.8	15	28	4
422	2.8	2.8	18	56	4
224	2.7	2.7	107	52	-
158	3	3	1006	242	-
116	3.5	3.5	300	41	28
83	2	-	259	-	26
24	3	-	146	-	-

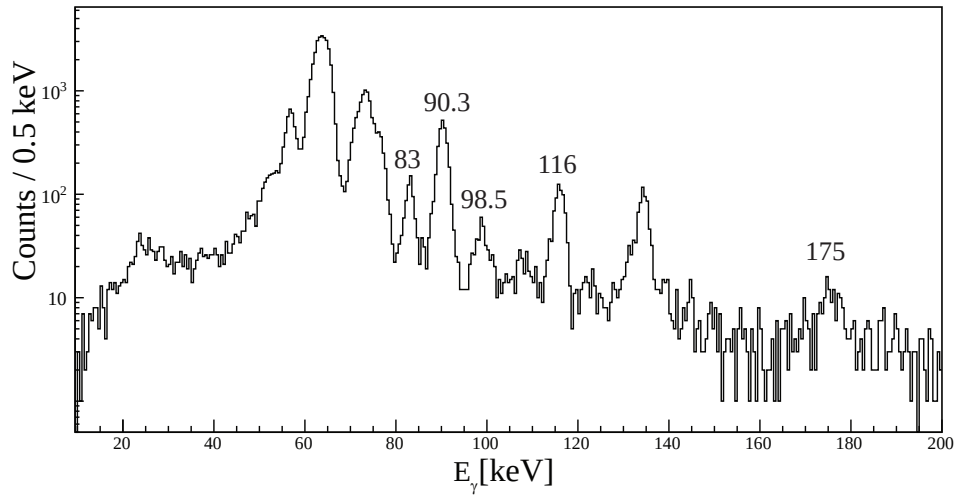

Figure 4.7: Projection on the γ energy axis between the two dotted blue lines in Figure 4.5. The marked peaks were identified as a single-step γ transition in ^{178gs}Au.

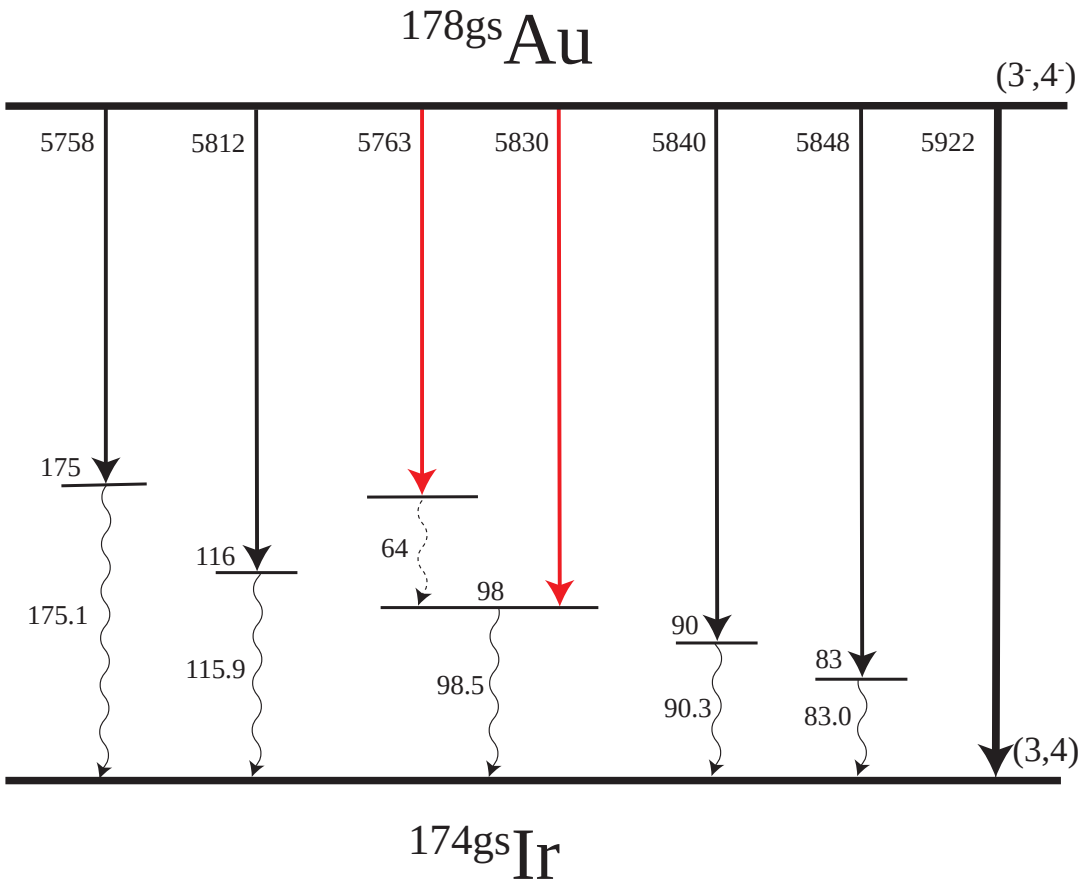

Figure 4.8: Decay scheme of ^{178gs}Au deduced in this work, the energies are in keV. The red lines shows the new transitions, while the dashed lines are the ones were not observed in the data. The nuclear spins adopted from [Cub17].

the α-γ analysis is by choosing an appropriately-selected background energy gate and subtracting it from the desired one. This method is used in the following analysis.

Two alpha lines feeding the 98.5 keV state were observed in the data (5763 and 5830 keV), Figure 4.6 (c). Both the α-γ groups are seen for the first time. The calculated $Q_{\alpha,tot}$ of the α-γ group 5830–98.5 keV is 6064, which is in a good agreement with the $Q_{\alpha,tot}$ of the ground-ground alpha decay transition (5922 keV), 6058 keV. However, the Q-value of the α-γ group 5763–98.5 keV is 5994 keV, which lead to $\sim$ 64 keV energy missing from the full-energy fine-structure decay of the 5922 keV ($Q_{\alpha,tot}$ = 6058 keV). This 64 keV γ-ray energy could not be observed individually in the data because it is lying in the region of high-intensity Ir K_α X rays (E_x = 63-65 keV) [Fir+96].

The 5840–90 keV and 5848–83 keV are single-step transitions where only one γ ray followed by each α decay, Figure 4.6 (a and b). These two α-γ groups were seen previously in ISOLDE's data.

The unmarked α peaks in Figure 4.6 (b,c,e) are random background from other competing reaction channels.

It is not possible to calculate the reduced α decay widths, δ^2, in the present work. It is because the most intense α peaks from the two states have an energy difference of $\sim$ 1 keV, which is far beyond the resolution of the DSSSD. Therefore, these α decays cannot be used to calculate δ^2 .

4.4.2 Isomeric State Decay of ^{178}Au

The α-decaying isomeric state in ^{178}Au was first identified in the ISOLDE IS534 experiment [Cub17] and a number of α-γ coincidence groups were identified, see Figure 4.1. In our study, due to a much larger statistics, we were able to confirm these results, and crucially -to confirm the presence of α(5573)-421.6 keV and α(5516)-471.7 keV groups, which were weakly seen at ISOLDE, see Table 4.2.

In this work, except for higher-energy 421 and 471 keV γ rays (see further), the whole α-γ analysis was performed with the use of data from PGD. This is because most of γ rays of ^{178}Au are low-energy (below 200 keV), for which the PGD provided a much higher detection efficiency than the Clovers. Based on the calculated $Q_{\alpha,tot}$ for the strong α-γ group 5923-56.9 keV, Figure 4.5 demonstrates the diagonal red line of α-γ groups having the same $Q_{\alpha,tot}$. Seven α-γ groups were observed in the data: 5961–24.1 keV, 5890–91.0 keV, 5843–139.4 keV, 5923–56.9, 5516–471.7 keV and 5573–421.6 keV. The α decay in coincidence with the γ transition are shown in Figure 4.10. The confirmation of the isomeric-isomeric α-decay energy (5978 keV) is discussed in Chapter 5.2 as this α decay cannot be seen individually in Figure 4.3. Table 4.3 displays the calculated $Q_{\alpha,tot}$ for the detected groups. The decay scheme of the isomeric state is presented in Figure 4.9. The new α and γ transitions are marked with red lines.

Two α-decay lines are seen for the first time: 5961–24.1 keV, and 5890–91.0 keV. On the other hand, the 5839–91.2 keV, 5740–56.8 keV and 5839–56.8 keV were not clearly observed in the present data. Figure 4.9 shows the proposed decay scheme of ^{178is}Au, where the red lines symbolise the first time seen α decays and the dashed curvy lines are the unseen γ rays.

The 5840 keV α-decay peak seen in coincidence with the 91 keV γ transition is due to unavoidable background subtraction from the neighbour 5840-90.3 keV α-γ group.

The 56.9 keV γ transition is in coincidence with the 5923 keV α decay, see Figure 4.10 (b). The $Q_{\alpha,tot}$ of the α-γ group, 5923–56.9 keV, is 6116 keV.

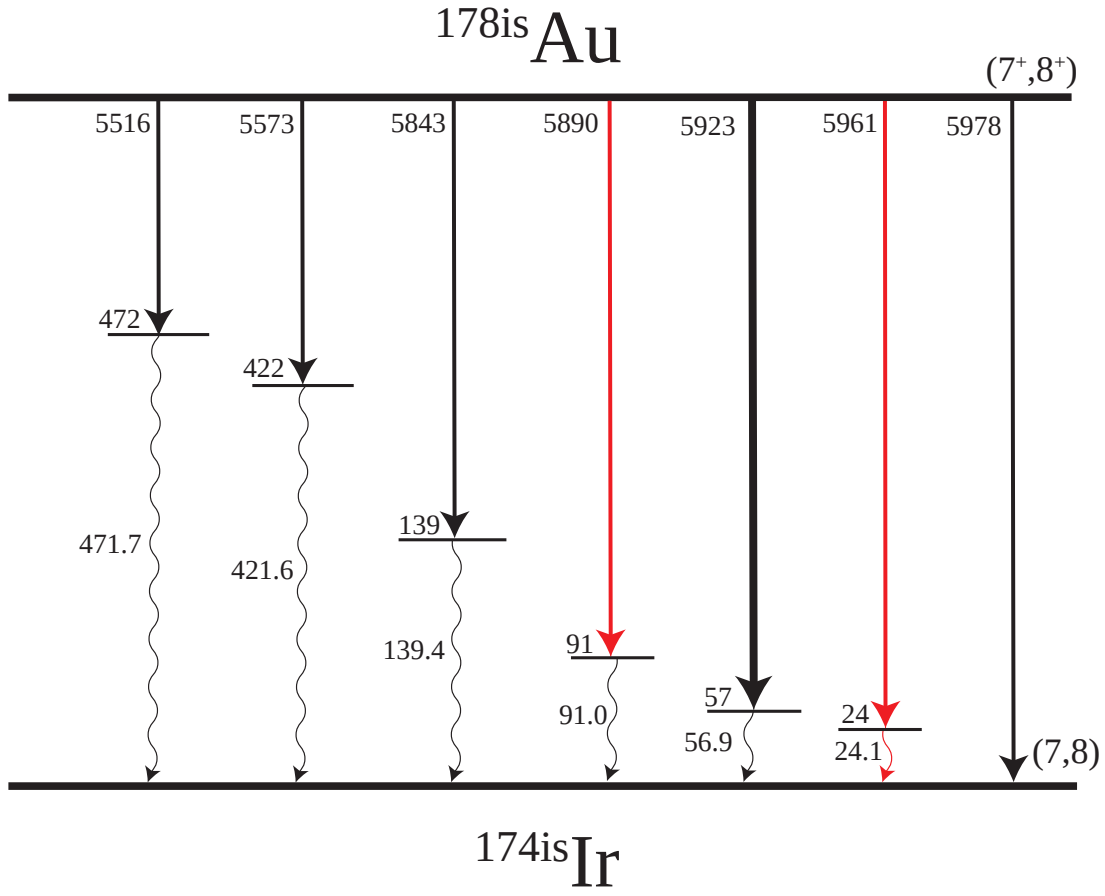

Figure 4.9: Decay scheme of ^{178is}Au deduced in this work, the energies are in keV. The red lines shows the new transitions, while the dashed lines are the ones were not observed in the data. The nuclear spins adopted from [Cub17].

The unmarked α peaks noticed in Figure 4.10 (c) resulted from an unavoidable background.

Two high-energy γ rays at 421.6 and 471.7 keV were detected in coincidence with two separate α lines, Figure 4.10 (e, f). These high-energy γ rays were seen in ISOLDE's experiment with very low statistics, four counts for each of the 5521 keV and 5573 keV α lines.

E_α [keV]	E γ [keV]	$Q_{\alpha,total}$ [keV]
5978(8)	0	6115(8)
5961(10)	24.1(3)	6122(10)
5890(6)	91.0(3)	6116(6)
5843(6)	139.4(2)	6117(6)
5923(7)	56.9(2)	6116(7)
5516(7)	471.7(4)	6115(7)
5573(12)	421.6(4)	6123(12)

Table 4.3: The $Q_{\alpha,tot}$ values for α-γ groups assigned to ^{178is}Au. The constant $Q_{\alpha,tot}$ signify that all lines originate from the same state in ^{178}Au

To conclude this section, it can be noted that despite the RITU study being unable to separate the decays of the two, long-lived states in ^{178}Au as cleanly as in the ISOLDE study, some important results were still obtained in the present work. One of the main conclusions being the confirmation of the 5516-471.7 keV and 5573-421.6 keV $\alpha - \gamma$ coincidence groups with about ten times the statistics of the ISOLDE study, for which only four counts in each group were observed.

The ISOLDE study suggested that the corresponding α decays of these coincidence groups should be unhindered, which – together with the unhindered 5927-keV decay of ^{178is}Au leads to three unhindered α decays from a single state. To our knowledge this is a unique situation, unseen in any other nuclide. Therefore, the unambiguous confirmation of these fine-structure decays in the data from the RITU experiment will crucially contribute to the final analysis of the alpha-decay scheme of ^{178}Au, presently being finalised.

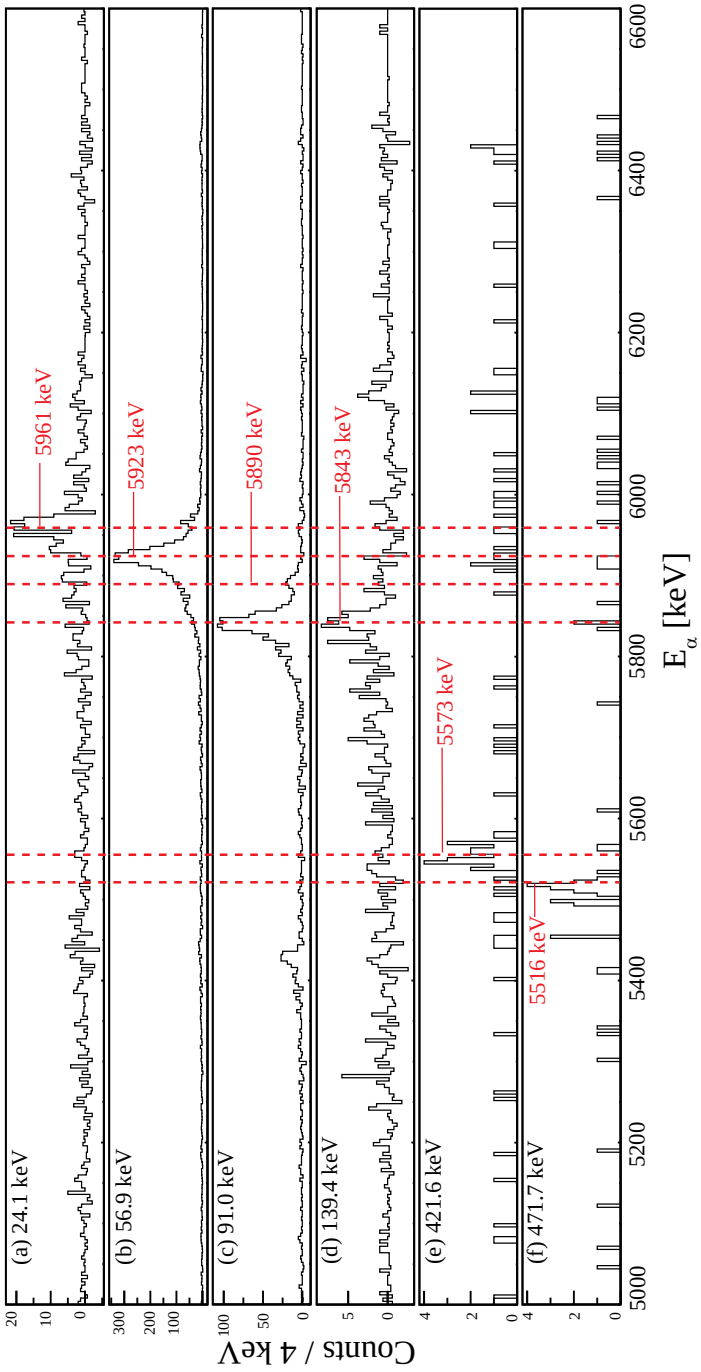

Figure 4.10: E_α projections spectra from the α-γ matrix of ^{178is}Au illustrated in Figure 4.5 gated on E_γ = (a) 24.1, (b) 56.9, (c) 91.0, (d) 139.4, (e) 421.6 keV and (f) 471.7. The E_γ gating condition used in the alpha-gamma matrix is ± 1.5 keV. The spectra are background subtracted.

Chapter 5

Detection of μs Isomers in ^{178}Au

This chapter describes the first identification of two sub-μs isomeric transitions in ^{178}Au. These results will be particularly important for the follow-up analysis of prompt in-beam data for ^{178}Au, as they will allow the Recoil-Isomer Tagging technique to be applied, instead of Recoil-Decay tagging. The corresponding analysis is being performed by the author of this thesis, some examples of it are shown in this chapter, but the discussion of final results is out of scope of the present thesis work.

The decay of a nucleus which has an isomeric state with half-life comparable to or greater than its flight time through a separator, could be observed at the focal plane of the separator. Figure 5.1 (a) illustrates recoil-gated γ-ray singles detected in the focal plane PGD (x-side) within 1μs of a recoil implantation in the DSSSD ($0 < \Delta T(ER - \gamma) < 1\mu$s). The time random events in red are the γ rays detected within 1μs before a recoil implantation in the DSSSD ($-1 < \Delta T(ER - \gamma) < 0\mu$s). The PGD background-subtracted spectrum is shown in Figure 5.1 (b). Several γ-ray peaks were observed, whereby some of them could be readily attributed to known nuclides, e.g. ^{177}Pt and ^{179}Au. These nuclei were produced as by-products in the studied reaction, ^{88}Sr + ^{92}Mo $\rightarrow$ ^{180}Hg*. The previously known isomeric transitions are 62.4(2) and 89.5(3) keV in ^{179}Au [Ven+11] and 147.4(10) keV in ^{177}Pt [Hag+79]. Two new isomeric transitions were detected and unambiguously identified for the first time in this study, with energies of, 50.3(2) and 56.6(4) keV in ^{178}Au.

The half-lives of isomeric states were deduced in the present work by fitting the time distribution between the implantation of a recoil and subsequent decay in the PGD, such that: $T = P_t - R_t$, where P_t and R_t are the PGD and recoil timestamps respectively. The half-life of the isomeric γ-ray transition is extracted from the time distribution fit by using an exponential functions and a constant background;

$$N(t) = Ne^{-\lambda t} + C\,, \tag{5.1}$$

where $N(t)$ is the remaining counts at time t, the first term is the remaining counts of the gated peak and the last term C is the flat time distribution.

The deduced half-lives of the isomeric transitions are shown in Table 5.1. The good agreement of our values for the known isomeric transitions confirms the validity of our method. The following discussion is constrained on the 50.3 and 56.6 keV isomers.

Table 5.1: Comparison of half lives extracted in this work with previous results.

		$T_{1/2}$	
Isotope	γ transition (keV)	Present work	Previous work
^{177}Pt	147.2	2.35(4) μs	2.2(3) μs [Hag+79]
^{178}Au	50.3(2)	300(10) ns	-
^{178}Au	56.6(4)	390(10) ns	-
^{179}Au	62.4(2)	304(9) ns	328(2) ns [Ven+11]
^{179}Au	89.5(3)	304(9) ns	328(2) ns [Ven+11]

The isomeric ratios for the two isomers (50 keV : 57 keV) where measured to be 1:6, which is in agreement with systematic analysis for nuclei having two isomeric states.

5.1 Identification of 50 keV isomeric transition in ^{178}Au

By using the same method as for known 62, 89 and 147 keV γ decays, the half-life values were determined for the new isomeric transitions at 50 and 57 keV. Figure 5.2 shows the (ER-γ) time distribution resulted for a time window of ($0 < \Delta T(ER{-}\gamma) <$

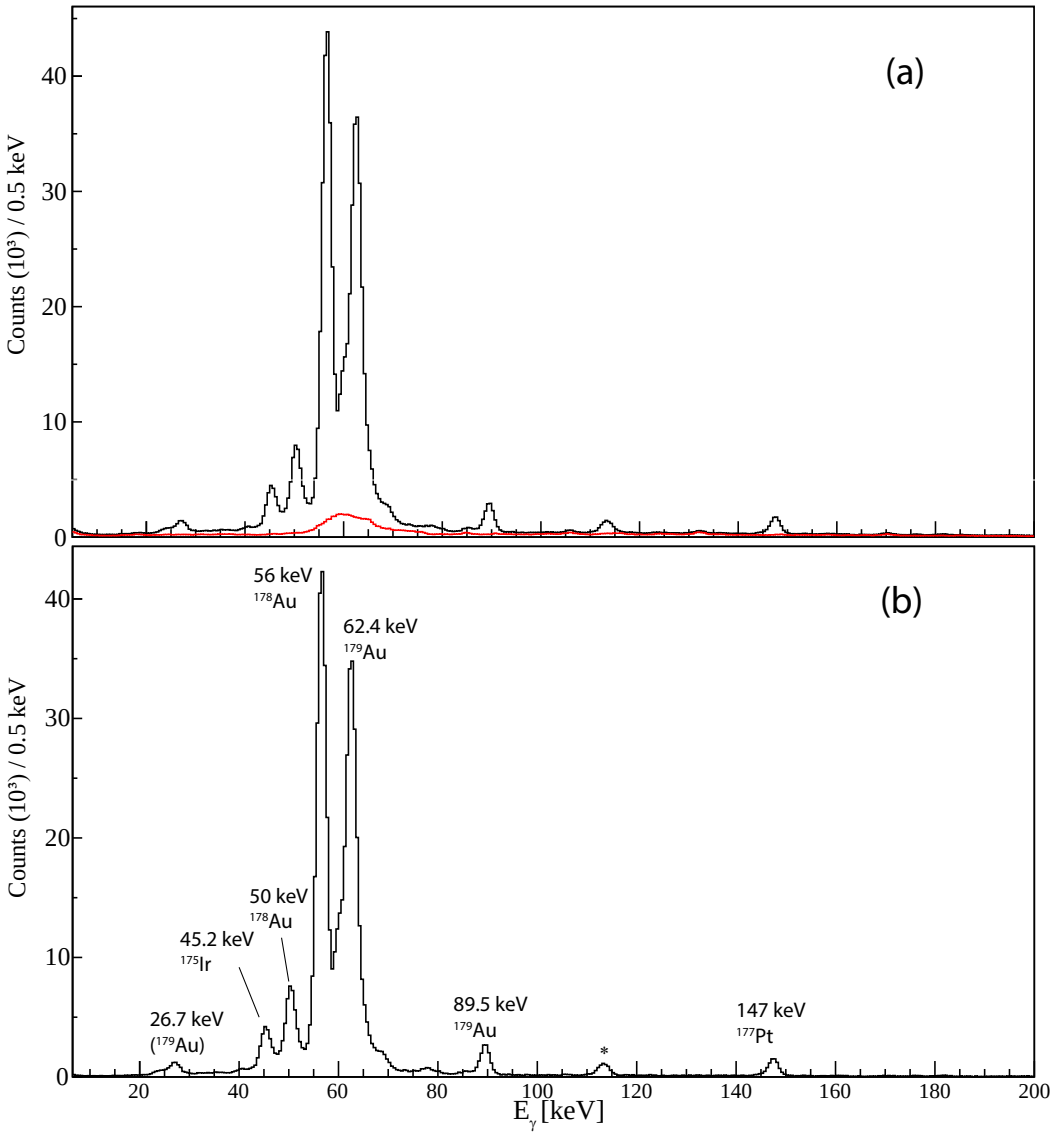

Figure 5.1: (a) Recoil-gated γ-ray singles detected in the PGD within 1μs of a recoil implantation in the DSSSD. In red are the time random γ rays detected within -1 $-$ 0 μs. (b) Recoil-gated γ-ray singles with time random events subtracted. See text for details.

4μs) for the 50.3 γ-ray peak. The inset in the figure illustrates the position of the energy gate used to project the time distribution. The half-life value of $T_{1/2}$(50 keV)=300(10) ns was deduced.

As mentioned in Section 4.3, due to the long half-lives of ground states of the studied nuclei and high implantation rates, the use of RDT method was hampered in this case to determine the origin of this isomeric transitions. Instead, the use of Isomer Decay Tagging technique (IDT) [Sch+03] is much more effective in this

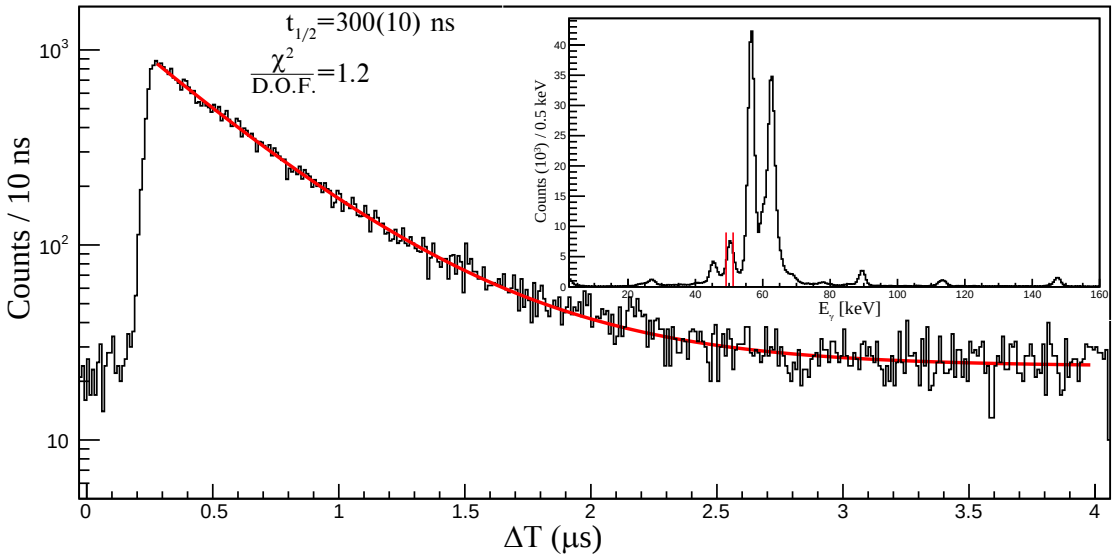

Figure 5.2: The decay curve of the 50.3 keV γ-ray transition fitted with an exponential function plus a constant background. The inset shows PGD energy spectrum observed within 1μs of an implantation of a recoil. The vertical red lines shows the position of the energy gate used.

case. Figure 5.3 shows the recoil-gated singles γ-rays in JG observed with gates on 50.3 keV 56.6 (see later) and 62.4 keV isomeric transitions, the last belonging to ^{179}Au. We note that the γ-rays in JG seen with a gate on 62.4 keV (shown by black spectrum) all belong to known decay of excited states in ^{179}Au, which also confirms the validity of our method. This spectrum shows that the observed $K_{\alpha,\beta}$ X rays are all from Au, thus this proves that all three isomeric transitions happen in gold isotopes. It is important to stress that none of the 50.3 and 56.6 keV isomeric transitions was observed earlier dedicated studies of in ^{177,179}Au. Furthermore, as ^{178}Au is the strongest-produced gold isotope in the studied reaction, one can suspect that 50.3 and 56.6 keV originate from this nucleus.

As the next step in the analysis, we produced spectrum of alpha particles observed in the DSSSD within 8 s after the detection of the 50 keV isomeric decay in the PGD, with a time gate of ΔT(ER-50 keV)$<$ 1 μs, , see Figure 5.4.

The background subtraction method used in this spectrum is discussed in Section 3.6.3. The two main α lines at 5927 keV and 5444 keV match well to the known alpha decays of ^{178gs}Au and its daughter after β decay, ^{178}Pt respectively. This fact reliably establish that the 50 keV isomeric transition feeds to the ground state of ^{178}Au.

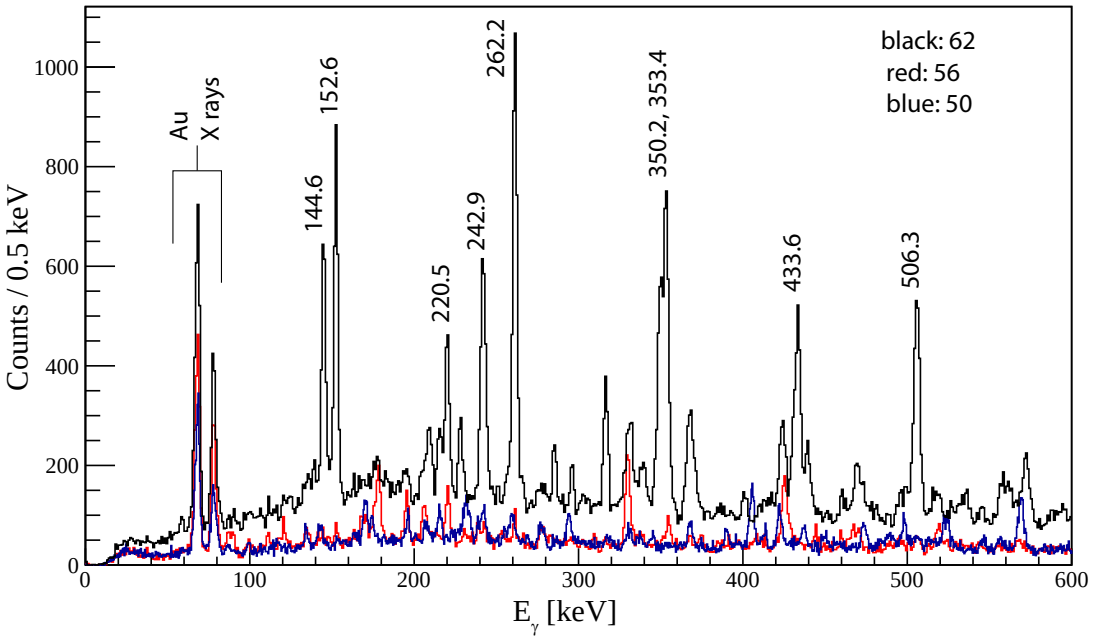

Figure 5.3: IDT spectra in JG with a gate on isomeric transitions at 62,4 keV (black), 56.6 keV (red) and 50.3 keV (blue) in PGD. The marked energy peaks are from the know γ-ray transitions in ^{179}Au [Mue+04].

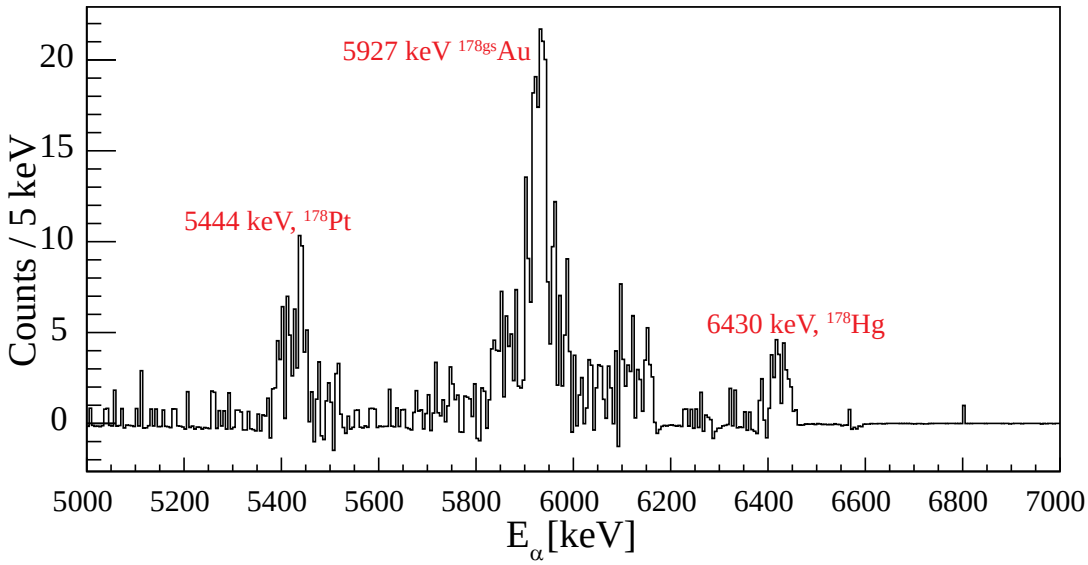

Figure 5.4: Background subtracted α-decay spectrum gated by the 50.3 keV isomer. see text for details.

The total conversion coefficient for a transition following an isomeric state can be calculated from:

$$\alpha_{exp,tot} = \left(\frac{N_\gamma}{N_{\gamma\gamma}} \times \varepsilon \right) - 1 \,, \tag{5.2}$$

where N_γ is the number of events in a specific γ-ray peak in JG, $N_{\gamma\gamma}$ is the number of counts in the same peak in JG with an extra gate on the isomeric decay at 50 keV, and ε is the PGD efficiency at 50 keV. Figure 5.5 (a) shows the JG recoil gated spectrum, while the same spectrum with a gate on the isomeric 50 keV is shown in Figure 5.5 (b).

Only one γ ray at 206 keV considered as 'clean' in JG as it gives the exact γ ray peaks as seen in the Isomer Decay Tagging of the 50 keV γ-ray transition. The number of counts N_γ and $N_{\gamma\gamma}$ in the 206 keV peak in Figures 5.5 (a) and (b) were calculated and compared using two different routines, ROOT [BR97] and RADWARE [Rad95] software packages and then the Eq. 5.2 was used to extract the experimental value of $\alpha_{exp,tot}$(50 keV).

Table 5.2 shows the calculated $\alpha_{exp,tot}$ using the 206 keV transition. The measured value is within 2 σ from the theoretical conversion coefficient for $E2$ multipolarity, and about 3 times lower than the next possible $M2$. Based on this, we assign $E2$ multipolarity to the 50.3 keV transition.

Table 5.2: The deduced multipolarity (ρl) for the 50.3 keV γ transition. See the text for explanation of the used method.

		$\alpha_{theory,tot}$ [Kib+08]						
E_γ (keV)	$\alpha_{exp,tot}$	$E1$	$M1$	$E2$	$M2$	$E3$	$M3$	deduced ρl
206	157(19)	0.5442	9.853	125.5	433.1	6936	20940	$E2$

Another way to test the validity of the conversion coefficient calculated above, is by comparing JG[ER-γ-γ(220)] with [JG(ER-γ-γ(220))]-PGD(50) keV spectra. Figure 5.6 (a) and (b) illustrates these two spectra, respectively. The choice of 220 keV γ-ray in this case was used to its unmixed nature, which is also proved by IDT spectrum in Figure 5.6

The deduced value of $\alpha_{exp,tot}$=120(36) is compared with theoretical values in Table 5.3.

Table 5.3: The deduced multipolarity for the 50.3 keV γ transition by using the 2nd method. See the text for explanation of the used method.

		$\alpha_{theory,tot}$ [Kib+08]						
E_γ (keV)	$\alpha_{exp,tot}$	$E1$	$M1$	$E2$	$M2$	$E3$	$M3$	deduced ρl
220	120(36)	0.5442	9.853	125.5	433.1	6936	20940	$E2$

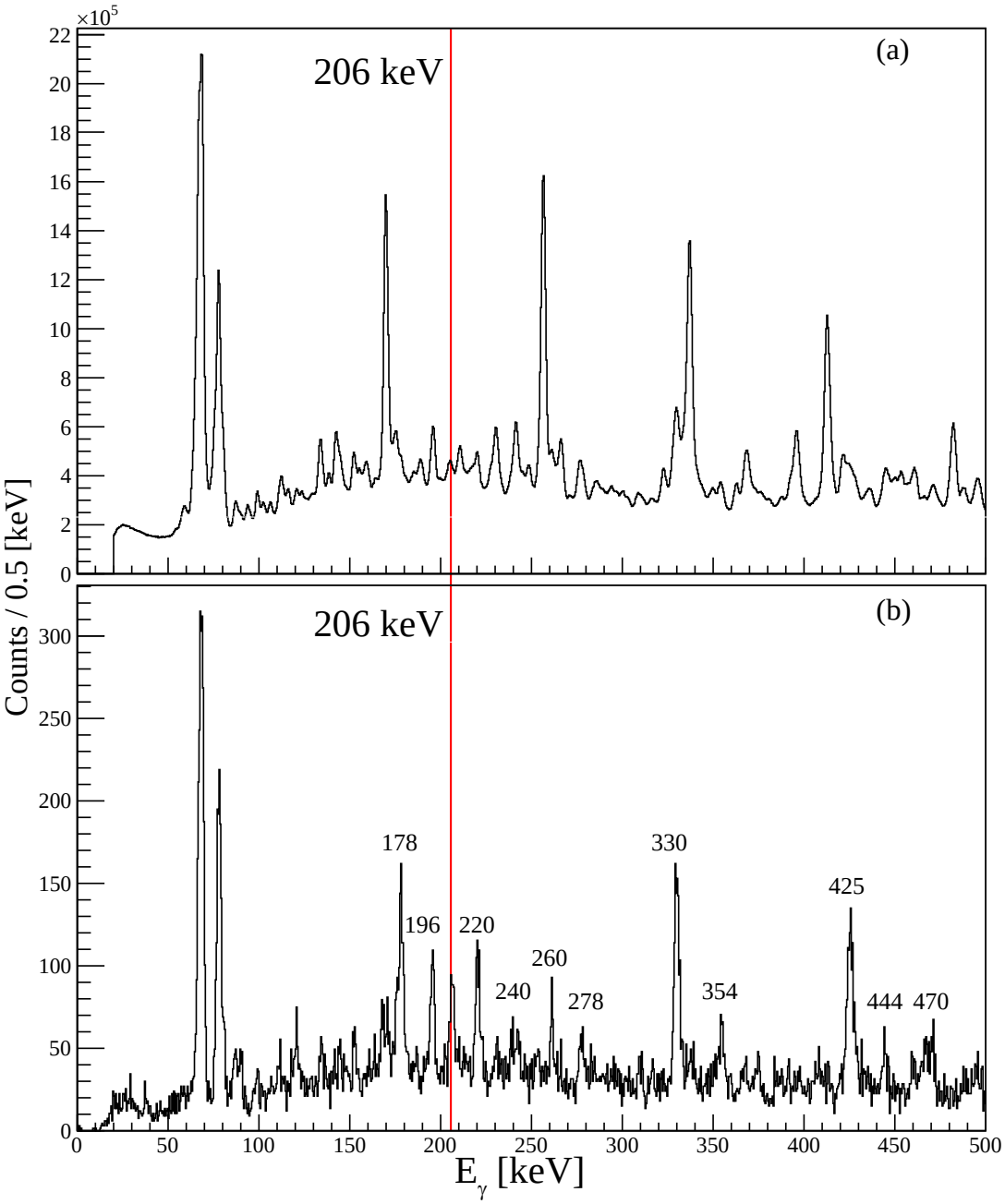

Figure 5.5: Energy spectrum of (a) γ rays of JG[ER-γ] and (b) γ rays of JG[ER-γ]-PGD(50).

By comparing the results from Tables 5.2 and 5.3, the deduced $\alpha_{exp,tot}$ are in good agreement within the experimental errors. Therefore, an $E2$ multipolarity is proposed for the 50.3 keV γ-ray transition.

The reduced transition strengths in Weisskopf units are calculated from;

$$B(EL;ML) = \frac{T_{1/2}(EL;ML)_{sp}}{T_{1/2}(EL;ML)_{exp}} \tag{5.3}$$

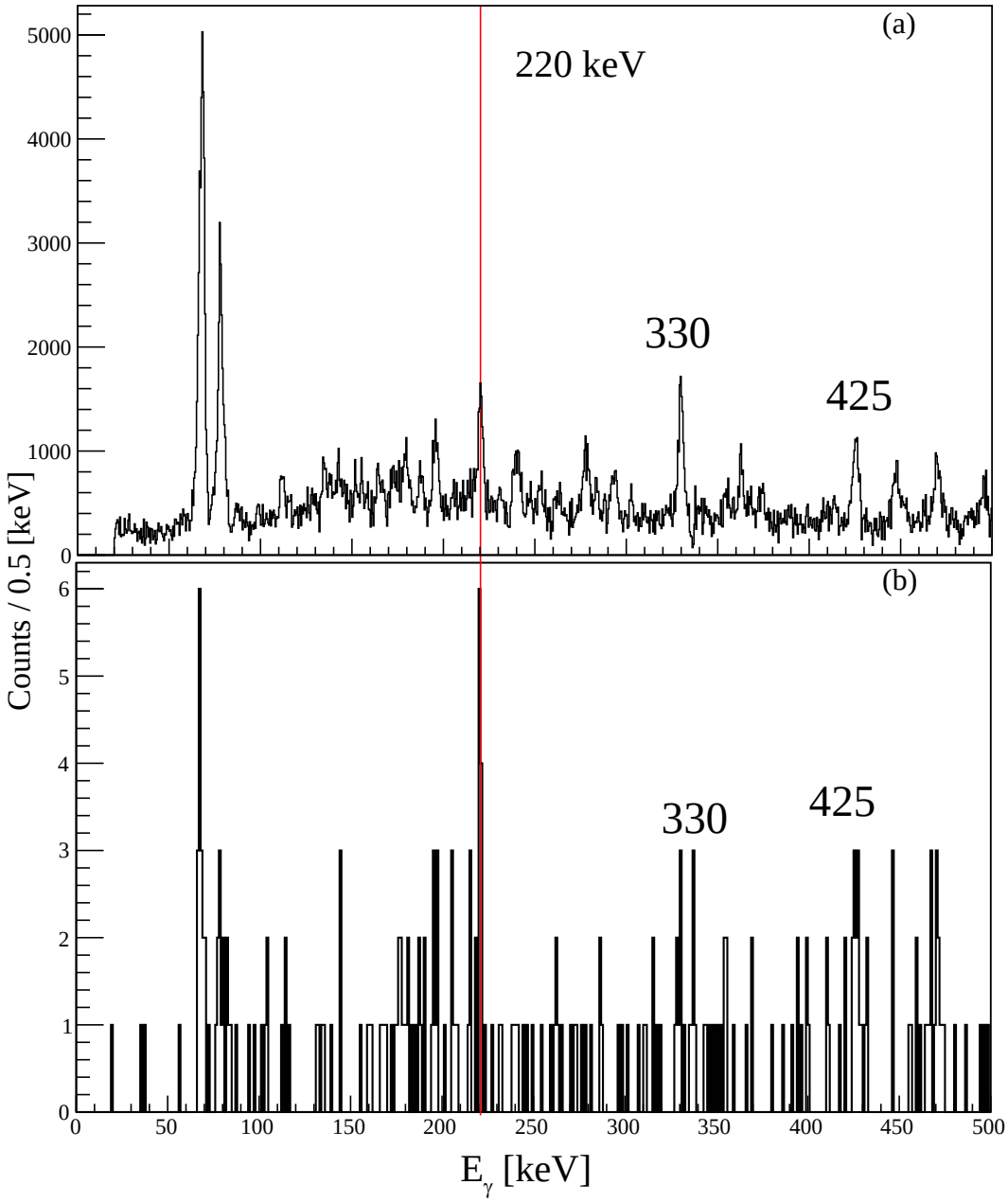

Figure 5.6: Energy spectrum of (a) γ rays of [ER-γ-γ(220)] and (b) γ rays of [ER-γ-γ(220)]-PGD(50).

where the single-particle half-life estimates, $T_{1/2}(EL;ML)_{sp}$, for the first four lower multiple orders can be calculated from [Fir+96];

$$
\begin{aligned}
T_{1/2}(E1) &= \frac{6.76 \times 10^{-6}}{E_\gamma^3 A^{2/3}} &&= 2.4 \times 10^{-12}\text{s} \\
T_{1/2}(E2) &= \frac{9.52 \times 10^{6}}{E_\gamma^5 A^{4/3}} &&= 5.27 \times 10^{-5}\text{s} \\
T_{1/2}(M1) &= \frac{2.20 \times 10^{-5}}{E_\gamma^3} &&= 1.73 \times 10^{-10}\text{s} \\
T_{1/2}(M2) &= \frac{3.10 \times 10^{7}}{E_\gamma^5 A^{2/3}} &&= 3.04 \times 10^{-3}\text{s} \\
T_{1/2}(M3) &= \frac{6.66 \times 10^{19}}{E_\gamma^7 A^{4/3}} &&= 8.16 \times 10^{4}\text{s}
\end{aligned}
\tag{5.4}
$$

and the experimental half-life is calculated from;

$$T_{1/2}(EL;ML)_{exp} = T_{1/2}(1 + \alpha_{exp}) \tag{5.5}$$

Table 5.4: The calculate single particle half-lives for the 50.3 keV γ transition, $T_{1/2}(EL;ML)_{sp}$, the deduced experimental half-life, $T_{1/2}(EL;ML)_{exp}$ and the single particle estimates, $B(EL;ML)$, for different multipolarities.

	$\rho; E, M$						
	$E1$	$M1$	$E2$	$M2$	$E3$	$M3$	deduced ρl
$T_{1/2}(EL;ML)_{sp}$	2.40×10^{-12}	1.73×10^{-10}	5.27×10^{-5}	3.04×10^{-3}	3.12×10^{-1}	8.16×10^{4}	
$T_{1/2}(EL;ML)_{exp}$	5.59×10^{-7}	2.50×10^{-6}	2.88×10^{-5}	9.89×10^{-5}	1.57×10^{-3}	4.72×10^{-3}	$E2$
$B(EL;ML)$ (W.u)	4.67×10^{-6}	6.92×10^{-5}	1.03	3.08×10^{1}	1.99×10^{2}	1.73×10^{7}	

Table 5.4 combines the $T_{1/2}(EL;ML)_{exp}$, $T_{1/2}(EL;ML)_{sp}$ and $B(EL;ML)$ along with the expected typical $B(EL;ML)$ values for $A \geq 151$ nuclei [Fir+96]. These values also suggests an $E2$ multipolarities for the 50.3 keV γ-ray transition, where the $T_{1/2}(EL;ML)_{sp}$ is the closest value to $T_{1/2}(EL;ML)_{exp}$.

5.2 Identification of the 57 keV Isomeric Transition in ^{178}Au

The second μs isomeric transition was detected with an energy of 56.6(4) keV, see Figure 5.1. The fact that K$_\alpha$, β X rays in Figure 5.3 for the three transitions at 50.3, 56.6 and 62.4 keV match each other well confirms that the 57 keV γ-ray transition should also originate from a gold isotope.

Using the same procedure that was used for the 50.3 keV isomer, the extracted half-life of the 56.6 keV γ-ray transition is 390(10) ns. Figure 5.7 shows the time distribution fitted with an exponential line plus constant background and the inset shows the energy (red).

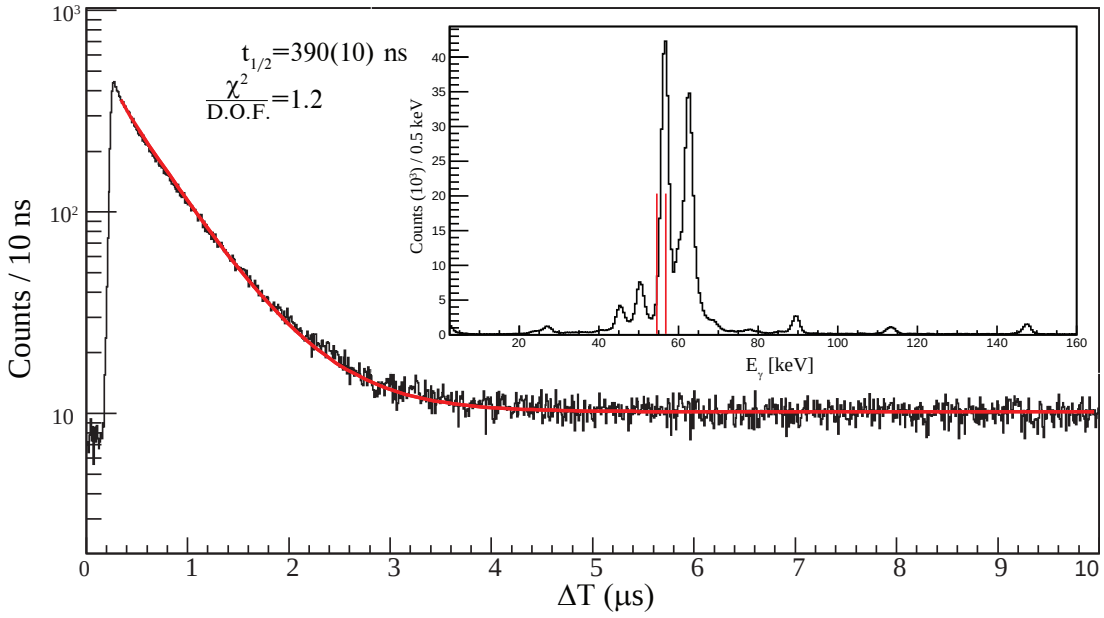

Figure 5.7: The decay curve of the 56.6 keV γ transition fitted with an exponential function plus a constant background. The inset shows the PGD energy spectrum observed within 1μ of an implantation of a recoil. The vertical red lines shows the position of the energy gate used.

Figure 5.8 shows overlay of the background subtracted α-decay spectra gated by the 50.3 (red) and 56.6 (black) keV isomers. The α-decay energies gated by the 56.6 keV are in good agreement with the ^{178is}Au. The different relative intensity balance between the 5925 and 5978 keV lines, in comparison to ISOLDE data, see Figure 4.1 is due to the α+e summing in the DSSSD. In this case, the 5925 keV alpha-decay is summed with conversion electron from 57 keV transition, thus producing the higher energy peak.

Based on observation of the 5978 keV transition, which is a signature for the alpha decay of isomeric states, we assign the 56.6 isomer as built on top of ^{178is}Au.

The procedure used to extract the total conversion coefficient for 57 keV transition is the same as one used for the 50.3 keV. Table 5.5 shows the calculated $\alpha_{exp,tot}(56.6)$ using the 276 keV γ transition which is seen the recoil-gated JG singles and gated by 56.6 keV. The measured value is within 2 σ from the theoretical conversion coefficient for $E2$ multipolarity and an $M2$ multipolarity is about 4 times higher than the $E2$. Therefore, we assign an $E2$ multipolarity to the 56.6 keV transition.

Table 5.5: The deduced multipolarity for the 56.6 keV γ transition. See the text for explanation of the used method.

		$\alpha_{theory,tot}$ [Kib+08]						
E_γ (keV)	$\alpha_{exp,tot}$	$E1$	$M1$	$E2$	$M2$	$E3$	$M3$	deduced ρl
276	40(12)	0.388	6.846	68.7	248.7	3359	9886	$E2$

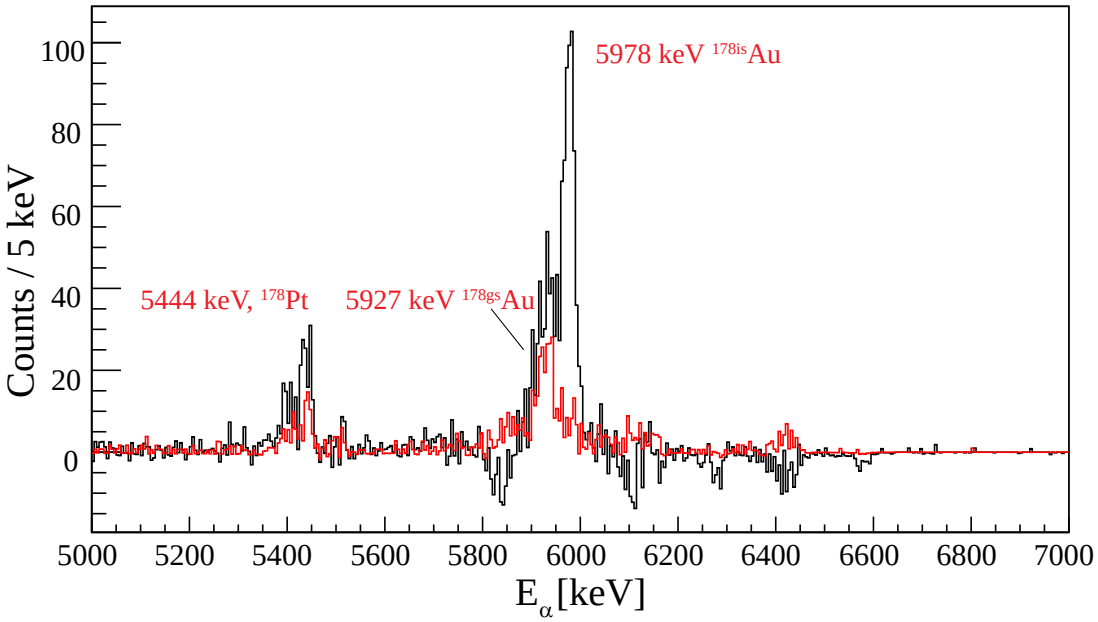

Figure 5.8: Background subtracted α-decay spectrum gated by the 56.6 keV isomer.

To summarize this chapter, the identification of two, sub-microsecond isomeric transitions, one built on top of the ground state, the other on top of the isomeric state in ^{178}Au will considerably simplify the next step in the data analysis – the construction of rotational bands in these nuclei. As the usage of RDT technique is somewhat hampered in this case, the use of IDT can provide the initial

identification of band members, which can then be followed by a $\gamma - \gamma$ coincidence analysis of the JUROGAM-II data.

Furthermore, the knowledge of excited states in ^{178}Au will help clarify the recent decay studies of two, long-lived α-decaying states in ^{182}Tl, performed by the same ISOLDE collaboration [Van+16]. In the case of ^{182}Tl to ^{178}Au decay, several fine-structure α decays were observed, followed by several γ rays. However, no consistent decay scheme could be constructed, due to the expected complexity of excited states in the deformed odd-odd nucleus, ^{178}Au

Chapter 6

Decay Studies of ^{174}Ir

6.1 Previous α-decay Study of ^{174}Ir

In our study, we could also observe α decay of the daughter nucleus ^{174}Ir, which is produced by α decay of the parent ^{178}Au. Figure 6.1 illustrates the decay scheme deduced by Schmidt-Ott *et al.* [Sch+92] In their experiment, the complete fusion reaction ^{36}Ar + ^{141}Pt $\rightarrow$ ^{174}Ir + 3n was used, in which ^{174}Ir was the main product. Thus, this study could obtain high-statistics data, both for α and γ decays. Schmidt-Ott *et al.* reported two long-lived states, a low-spin $I = (3^+)$, $T_{1/2} = 9$ s state and a high-spin $I = (7^+)$, $T_{1/2} = 4.9$ s state. Both states have a weak alpha decay branching ratios.

One α decay from the low-spin ground state of ^{174}Ir with an energy of 5275 keV fed the 225 keV excited state above the ground state of the α daughter nucleus ^{170}Re. Three γ-ray transitions with energies of 224.6, 193.5 and 31.4 keV were observed in coincidence with 5275 keV α decay.

The high-spin state decays by two α decays, 5478 keV and 5316 keV feeding excited states at 370.2 and 210.4 keV, respectively. The 5316 keV α decay was seen in prompt coincidences with four γ rays, 159.8, 210.3, 190.2 and 20.2 keV. The 210.3, 190.2 and 20.2 γ transitions were also seen in the coincidence with the 5478 keV α decay.

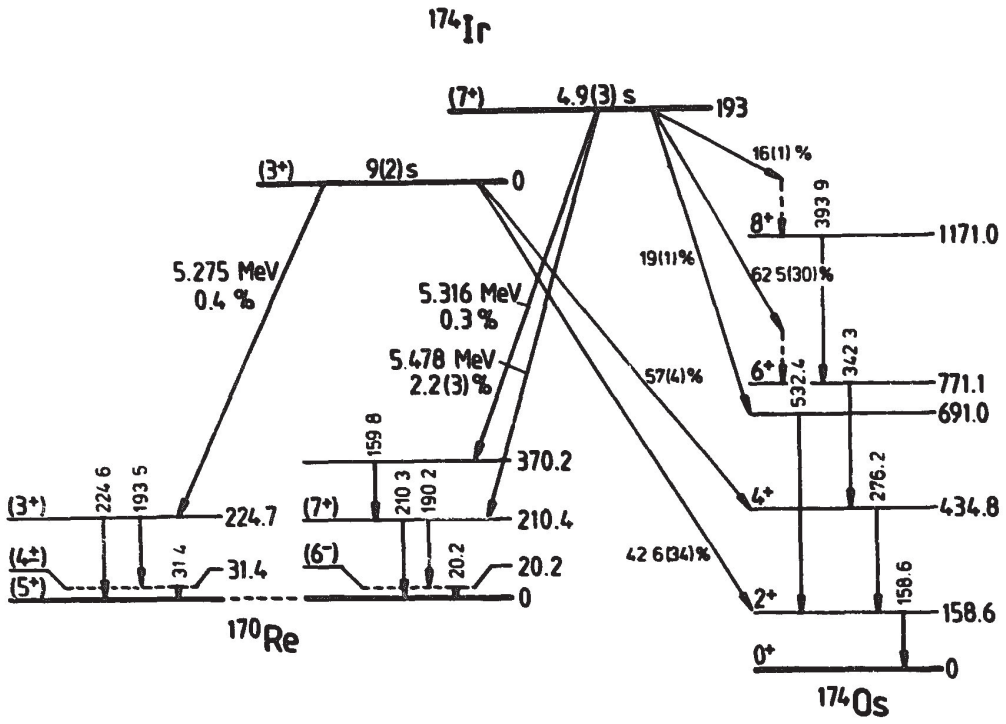

Figure 6.1: ^{174}Ir decay scheme produced from [Sch+92].

As ^{174}Ir nucleus is only a by-product of α decay of ^{178}Au in our study, our statistics are much lower in comparison to [Sch+92] and ^{174}Ir is just a small fraction of our data. Due to this, only α-γ data could be reliably observed in our experiment. Moreover, the extraction of β-decay data was strongly hampered by much more strongly produced channels.

In the following sections, we will discuss our α-γ data for ^{174}Ir.

6.2 Alpha Decay of ^{174gs}Ir

Figure 4.5 illustrates two α-γ groups, which belong to the decay of ^{174is}Ir: α(5271)-γ(224.2) and α(5301)-γ(193.1) keV. The energy of the first α decay and energies of γ rays match well to the study [Sch+92], but the 5301 keV line was not reported in the previous work. The projections on the E_α axis for events in coincidence with the 224.2 and 193.1 keV γ rays are shown in Figures 6.2 (a) and (b), respectively.

Both groups have the same $Q_{\alpha,tot}$ value, see Table 6.1. Based on these grounds, we propose a new decay scheme of ^{174gs}Ir, as shown in Figure 6.3, whereby

the two alpha decays feed respective excited states at 224 and 193 keV. The energy difference between the two states is 29(9) keV, which matches well to the energy of the γ ray of 31.0(4) keV, which was proposed by [Sch+92], see Figure 6.1. We could not observe this decay in our study, which is most probably due to its low relative intensity of 3.6(16)% relative to the strongest γ ray, 193.1(4) keV. This decay must then be placed between the 224 and 193 states, which differ from its placement in Figure 6.1.

Intensities $I_{\alpha 1}$ and $I_{\alpha 2}$ for 5271 and 5301 keV α decay were determined based on the following equation , applied to each group of α-γ coincidences 5271-224 and 5301-193 keV:

$$N_\alpha = \frac{N_{\alpha\gamma}}{\epsilon}(1+\alpha, tot)\,, \tag{6.1}$$

where N_α is the expected number of α counts in specific α decay, $N_{\alpha\gamma}$ is the measured f.s α counts, ϵ is the PGD efficiency for a given γ-ray energy, and α, tot is the calculated conversion coefficient for the γ ray in coincidence with the α decay (). The calculated values are: $I_{\alpha 1}$(5301 keV)=75(4)% and $I_{\alpha 2}$(5271 keV)=25(4)%.

E_α [keV]	E_γ [keV]	$Q_{\alpha,total}$ [keV]
5271(5)	224.2(3)	5619(5)
5301(8)	193.1(4)	5619(8)

Table 6.1: The $Q_{\alpha,tot}$ values for α-γ groups assigned to ^{174gs}Ir. The constant $Q_{\alpha,tot}$ signify that both alpha decays originate from the same state in ^{174}Ir.

6.3 Alpha Decay of ^{174is}Ir

Alpha decay of the isomeric state in ^{174}Ir was also observed in our data. Figure 6.4 shows the α-γ matrix with time condition ($310 \leq \Delta t(\alpha\text{-}\gamma) \leq 600$ ns) which was used to remove the prompt coincidence events, and highlight only longer-lived γ-ray decays.

Two α-γ groups were detected and assigned to ^{174is}Ir, in the present data, 5489-189.7 keV and 5480-210.1 keV. Figures 6.5 (a) and (b) shows the two α decays

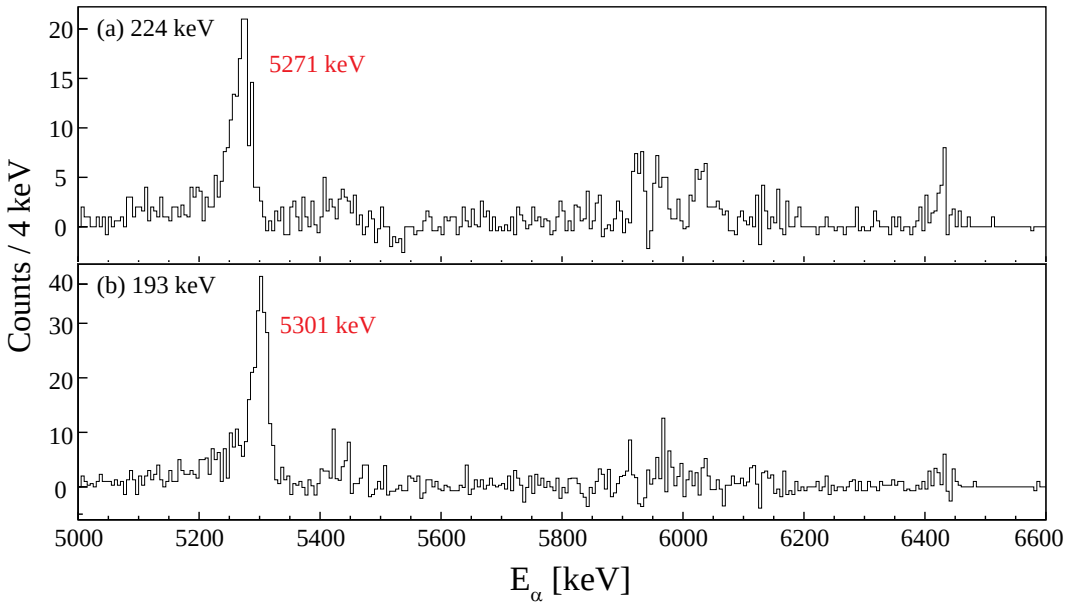

Figure 6.2: Projection on the E_α axis produced from α-γ matrix shown in Figure 4.5, for (a) E_γ = 224.2 keV and (b) E_γ = 193.1 keV.

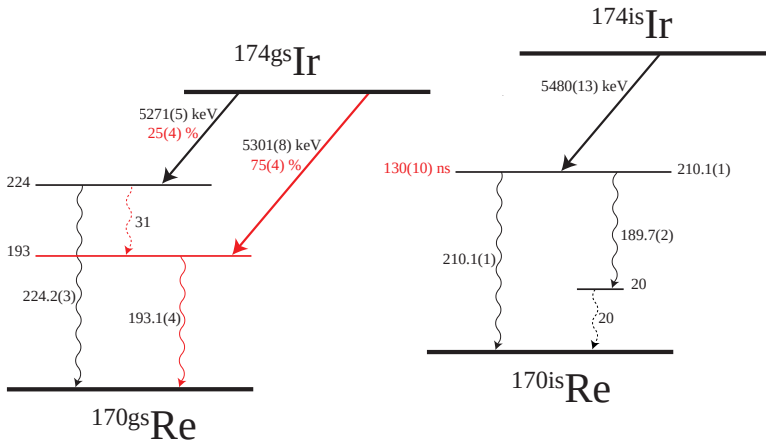

Figure 6.3: Partial decay scheme of ^{174}Ir deduced in this work. The red lines represent the transitions seen for the first time or repositioned. The dashed lines is the ones which not been observed in the data due to lower statistics in our study in comparison to [Sch+92]. The rest of the data, such as half-lives of the states and branching ratios for ^{174is}Ir are not shown here, as we could not measure them in our study and they should be taken from [Sch+92]

in coincidence with 189.7(2) keV and 210.1(1) keV γ rays respectively. The 5480 keV α decay is in a good agreement with study [Sch+92], while the 5489 keV is produced by α-electron summing, as explained below.

The 20 keV $E1$ γ ray (the multipolarity was proposed by Schmitt-study [Sch+92]) has a calculated conversion coefficient of α_{tot}=6.2, with predominantly L-conversion. This produced an L-shell conversion electron of 8 keV energy. Due

to implantation of recoils in the DSSSD, there will be summing of 5480 keV alpha decay energy with the energy of coincident conversion electron, resulting in artificial summing peak of $\sim$ 5489 keV, seen in our data. This peak will be observed in coincidence with the 189 keV γ ray, as indeed seen in Figure 6.4. Thus, we confirm the presence of 5480 keV decay in $^{174is}Ir$, feeding the excited state at 224 keV. The 20 keV γ ray is not observed in the data due to lower statistics and low branching ratios $I_\gamma = 2.6(10)\%$ relative to the total γ decays following the α decays from ^{174is}Ir [Sch+92].

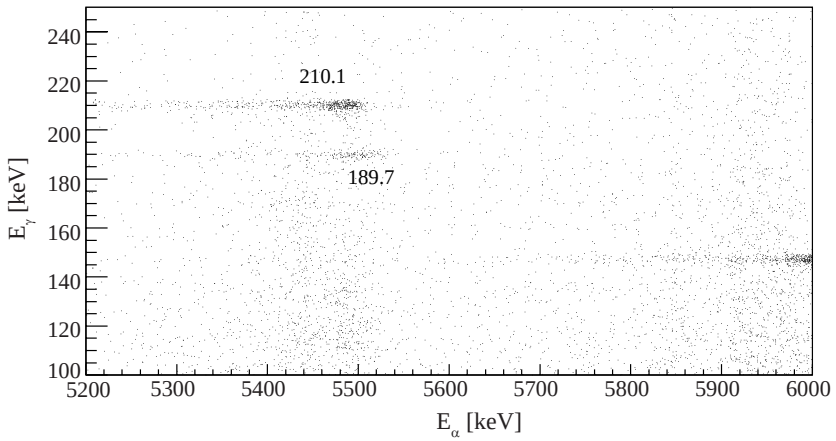

Figure 6.4: The α-γ matrix with ($310 \leq \Delta t$ (α-γ) ≤ 600 ns) time condition. The two groups seen at 210 and 190 keV were assigned as following the α decay of the isomeric state in ^{174}Ir.

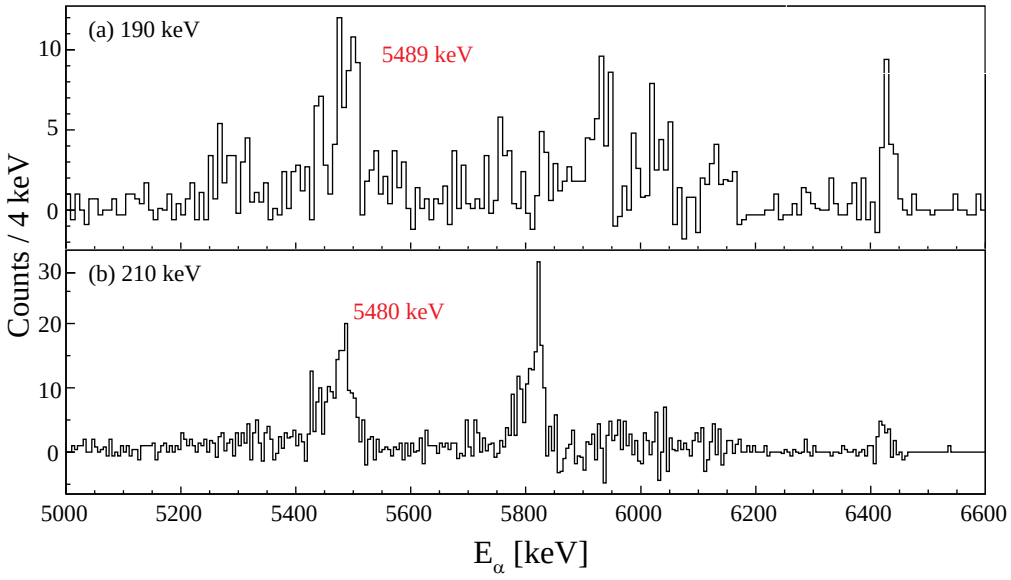

Figure 6.5: Projection on the E$_\alpha$ axis produced from α-γ matrix shown in Figure 4.5, for (a) E$_\gamma$ = 189.7 keV and (b) E$_\gamma$ = 210.1 keV.

Figure 6.6 illustrates the time difference between a PGD event and an α decay detected in the DSSSD, for 210 keV (a) and (b) 189.7 keV γ-ray transitions.The time behavior clearly shows an exponential decay, which is in contrast to the sharp, Gaussian-like pattern for the known prompt $\alpha(5291)$-$\gamma(158.7)$ coincidences originating from ^{178}Pt [Hil+92], which is also seen in Figure 4.5.

The extracted half-lives are 133(9) ns for the 210 keV and 122(15) ns for the 189.7 keV γ transitions respectively. Combining statistics for the two transitions, a half-life value of 130(10) ns was deduced for the 210 keV state, shown in our decay scheme in Figure 6.3.

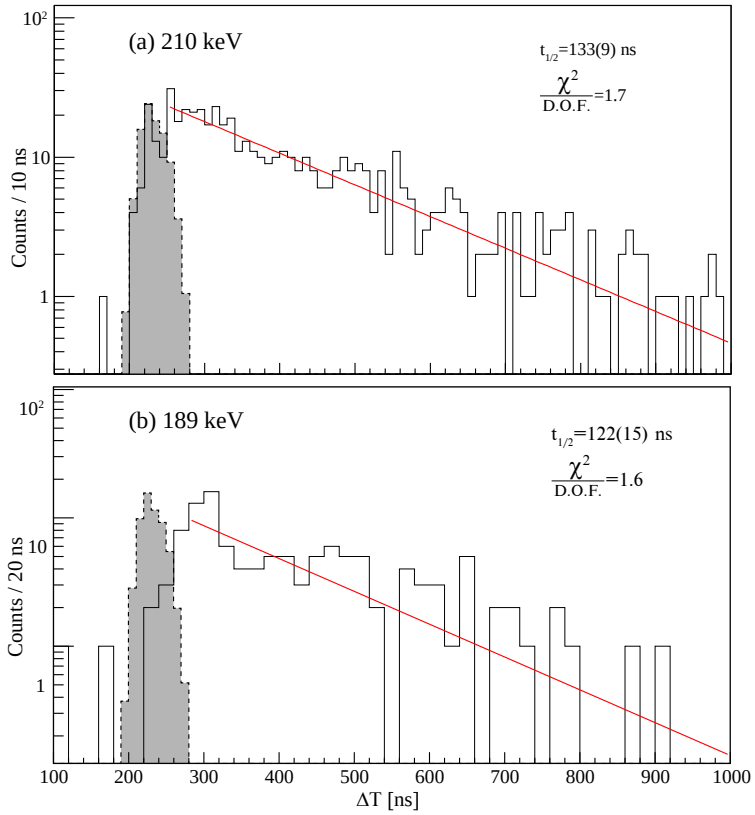

Figure 6.6: The time distribution of the (a) 210 keV and (b) 189 keV γ rays deduced from α-γ coincidences. The decay curves are compared with the time distribution for prompt 158.7 keV γ ray seen in ^{174}Os (grey). For better presentation, the prompt peak has been scaled down by a factor of $\sim$ 50.

To summarise this section, we were able to derive an improved decay scheme of ^{174gs}Ir, see Figure 6.3, and to determine the life time of the 210 keV state in ^{170is}Re. The relative intensities of two alpha decays at 5301 keV ($I_{\alpha 1}$=75(4) % and 5271 keV

$I_{\alpha 2}$=25(4) were also deduced. Due to the method used in our study, we could not determine other decay properties of ^{174}Ir, thus they should be taken from study [Sch+92].

Chapter 7

Summary and Future Work

The present thesis discusses the results from decay studies of the very neutron-deficient nuclei ^{178}Au and ^{174}Ir. The ^{178}Au nucleus was produced in the fusion-evaporation reaction ^{92}Mo(^{88}Sr,np)^{178}Au, in an experiment performed at University of Jyväskylä. A combination of the JUROGAM II γ-ray array and the gas-filled RITU separator was used, complemented by the GREAT spectrometer at the focal plane of RITU. In addition to this, the structure of ^{174}Ir was studied as a daughter of ^{178}Au after its α decay.

The study of ^{178}Au became important after a complementary experiment performed at ISOLDE a few years ago identified two α-decaying states in this nucleus. Furthermore, based on charge-radii measurements, it was concluded that both states should be strongly deformed. As such, a complementary in-beam decay study of rotational bands in this nucleus would be to confirm the results of the ISOLDE study. It is important to stress that the author of present work took part in both the ISOLDE and RITU experiments.

The much higher statistics obtained during the RITU study of ^{178}Au, in comparison to the ISOLDE experiment, allowed us to detect several new fine-structure α decays in ^{178gs,is}Au. Especially important is the confirmation with about 10 times higher statistics of two specific groups of α-γ coincidences with (5516-471.7 and 5573-421.6 keV), for which only 4 counts for each group were observed at ISOLDE.

According to the ISOLDE study, these should be unhindered α-decays, which together with unhindered 5927 keV decay of ^{178is}Au would lead to three unhindered α decays from the same isotope. This is a very unusual situation, which to our knowledge has never seen before. Therefore, the RITU study presented in this work strongly contributed to this particular issue, by providing the unambiguous confirmation of these decays.

Another important result of the present study the is identification of two sub-microsecond isomeric transitions built on top of the α-decaying ground and isomeric states in ^{178}Au. The knowledge of these states will considerably simplify the next step in the data analysis of the huge data set collected in this experiment. In particular, one of the main goals of this study was the identification of rotational bands built on top of the two long-lived states in ^{178}Au. As the usage of the Recoil-decay tagging technique is somewhat hampered in this case, the use of IDT can provide the initial identification of the band members, which can be followed by the γ-γ coincidence analysis of the JUROGAM-II data.

The information on excited states in ^{178}Au will be useful for clarification of the recent decay schemes of two long-lived α-decaying states in ^{182}Tl, proposed by the same ISOLDE collaboration based on systematical α-decay studies of odd-odd ^{180,182,184,186}Tl isotopes. In the case of ^{182}Tl $\rightarrow$ ^{178}Au decay, several fine structure α decays were observed, followed by several γ rays, but no consistent decay scheme was proposed, due to expected complexity of excited states in the odd-odd deformed nucleus, ^{178}Au. Thus, as the next immediate step in the data analysis, we will proceed in the construction of a detailed decay scheme for the excited states in ^{178}Au.

Looking further to the future, we wish to proceed with an in-beam study the of strongly-deformed nucleus, ^{180}Au. Its large deformation was also deduced in our ISOLDE study.

Bibliography

[Ali14] Fuad Arif Ali. "Shape Coexistence in the Proton-Unbound Nucleus 177Au". PhD thesis. Oliver Lodge Laboratory, 2014.

[Alv93] Carlo Rossi Alvarez. "The GASP Array". *Nuclear Physics News* 3.3 (1993), pp. 10–13.

[And+04] A.N. Andreyev, P.A. Butler, R.D. Page, D.E. Appelbe, G.D. Jones, D.T. Joss, R.-D. Herzberg, P.H. Regan, J. Simpson, and R. Wadsworth. "GEANT Monte Carlo simulations for the GREAT spectrometer". *Nuclear Instruments and Methods in Physics Research Section A: Accelerators, Spectrometers, Detectors and Associated Equipment* 533.3 (2004), pp. 422–434. ISSN: 0168-9002.

[And15] Andrei Andreyev. Private Communication. 2015.

[Ang12] Lee James Angus. *Spectroscopy of Exotic Proton-Rich Nuclei Close to A= 120*. Lee Angus, 2012.

[Aur15] Kalle Auranen. "Spectroscopy of ^{199,201}At". *Research report/Department of Physics, University of Jyväskylä* 2015, 5 (2015).

[Bea+92] C.W. Beausang, S.A. Forbes, P. Fallon, P.J. Nolan, P.J. Twin, J.N. Mo, J.C. Lisle, M.A. Bentley, J. Simpson, F.A. Beck, D. Curien, G. deFrance, G. Duchêne, and D. Popescu. "Measurements on prototype Ge and BGO detectors for the Eurogam array". *Nuclear Instruments and Methods in Physics Research Section A: Accelerators, Spectrometers, Detectors and Associated Equipment* 313.1 (1992), pp. 37–49. ISSN: 0168-9002.

[Bla+97] F Le Blanc, J Obert, J Oms, JC Putaux, B Roussiere, J Sauvage, J Pinard, L Cabaret, HT Duong, G Huber, et al. "Nuclear moments and deformation change in 184Aug, m from laser spectroscopy". *Physical Review Letters* 79.12 (1997), pp. 2213–2216.

[Boh41] N. Bohr. "Velocity-Range Relation for Fission Fragments". *Phys. Rev.* 59 (3 Feb. 1941), pp. 270–275.

[BR97] Rene Brun and Fons Rademakers. "ROOT — An object oriented data analysis framework". *Nuclear Instruments and Methods in Physics Research Section A: Accelerators,*

Spectrometers, Detectors and Associated Equipment 389.1 (1997). New Computing Techniques in Physics Research V, pp. 81–86. ISSN: 0168-9002.

[Car12] Robert Carroll. "Multiparticle configurations in 155Lu (N= 84) and 158Ta (N= 85)". PhD thesis. Citeseer, 2012.

[Cub17] James Cubiss. "In-source laser spectroscopy of At isotopes and decay studies of ^{178}Au". PhD thesis. University of York, 2017.

[Duc+99] G. Duchêne, F.A. Beck, P.J. Twin, G. de France, D. Curien, L. Han, C.W. Beausang, M.A. Bentley, P.J. Nolan, and J. Simpson. "The Clover: a new generation of composite Ge detectors". *Nuclear Instruments and Methods in Physics Research Section A: Accelerators, Spectrometers, Detectors and Associated Equipment* 432.1 (1999), pp. 90–110. ISSN: 0168-9002.

[Eva55] Robley D Evans. "The Atomic Nucleus. McGraw-Hill". *New York* 19552 (1955), pp. 785–793.

[Fed+00] VN Fedoseyev, G Huber, U Köster, J Lettry, VI Mishin, H Ravn, and V Sebastian. "The ISOLDE laser ion source for exotic nuclei". *Hyperfine Interactions* 127.1-4 (2000), pp. 409–416.

[Fir+96] Richard B Firestone, Virgina S Shirley, CM Baglin, SY Frank Chu, and J Zipkin. "Table of Isotopes, 8-th ed". *John Willey & Sons, New York* (1996).

[Gam28] George Gamow. "Zur quantentheorie des atomkernes". *Zeitschrift für Physik* 51.3-4 (1928), pp. 204–212.

[GC28] Ronald W Gurney and Edw U Condon. "Wave mechanics and radioactive disintegration". *Nature* 122.3073 (1928), p. 439.

[GI32] E. Gapon and D. Iwanenko. "Zur Bestimmung der Isotopenzahl". *Naturwissenschaften* 20.43 (Oct. 1932), pp. 792–793. ISSN: 1432-1904.

[Gri+02] E.L. Grigorescu, Anamaria Cristina Razdolescu, Maria Sahagia, A. Luca, C. Ivan, and G. Tanase. "Standardization of 152Eu". *Applied Radiation and Isotopes* 56.1 (2002). Proceedings of the Conference on Radionuclide Metrology and its A pplications, ICRM'01, pp. 435–439. ISSN: 0969-8043.

[Hag+79] E. Hagberg, P.G. Hansen, P. Hornshøj, B. Jonson, S. Mattsson, and P. Tidemand-Petersson. "Alpha decay of neutron-deficient mercury isotopes and their daughters". *Nuclear Physics A* 318.1 (1979), pp. 29–44. ISSN: 0375-9474.

[Hey+83] K. Heyde, P. Van Isacker, M. Waroquier, J.L. Wood, and R.A. Meyer. "Coexistence in odd-mass nuclei". *Physics Reports* 102.5 (1983), pp. 291–393. ISSN: 0370-1573.

[Hey04] Kris Heyde. "Basic ideas and concepts in nuclear physics: an introductory approach". *Fundamental and Applied Nuclear Physics. IOP, Bristol* (2004).

[HG07] S. Hilaire and M. Girod. “Large-scale mean-field calculations from proton to neutron drip lines using the D1S Gogny force”. *The European Physical Journal A* 33.2 (Aug. 2007), pp. 237–241. ISSN: 1434-601X.

[HG16] S Hilaire and M Girod. “Hartree-Fock-Bogoliubov results based on the Gogny force” (2016).

[Hil+92] L. Hildingsson, W. Klamra, Th. Lindblad, C.G. Lindèn, B. Cederwall, W. Satuła, R. Wyss, C. Kalfas, S. Kossionides, C.T. Papadopoulos, R. Vlastou, J. Gizon, D. Clarke, F. Khazaie, J.C. Lisle, and J.N. Mo. “High-spin phenomena in 174Os”. *Nuclear Physics A* 545.4 (1992), pp. 871–888. ISSN: 0375-9474.

[HJS49] Otto Haxel, J. Hans D. Jensen, and Hans E. Suess. “On the ”Magic Numbers” in Nuclear Structure”. *Phys. Rev.* 75 (11 June 1949), pp. 1766–1766.

[HW11] Kris Heyde and John L. Wood. “Shape coexistence in atomic nuclei”. *Rev. Mod. Phys.* 83 (4 Nov. 2011), pp. 1467–1521.

[Kel+86] J.G. Keller, K.-H. Schmidt, F.P. Hessberger, G. Münzenberg, W. Reisdorf, H.-G. Clerc, and C.-C. Sahm. “Cold fusion in symmetric 90Zr-induced reactions”. *Nuclear Physics A* 452.1 (1986), pp. 173–204. ISSN: 0375-9474.

[Kib+08] T. Kibédi, T.W. Burrows, M.B. Trzhaskovskaya, P.M. Davidson, and C.W. Nestor. “Evaluation of theoretical conversion coefficients using BrIcc”. *Nuclear Instruments and Methods in Physics Research Section A: Accelerators, Spectrometers, Detectors and Associated Equipment* 589.2 (2008), pp. 202–229. ISSN: 0168-9002.

[Kra87] K.S. Krane. *Introductory Nuclear Physics*. Wiley, 1987. ISBN: 9780471805533.

[Krö+88] U Krönert, G Bollen, M Gerber, Th Hilberath, H-J Kluge, G Passler, ISOLDE Collaboration, et al. “Observation of strongly deformed ground-state configurations in 184 Au and 183 Au by laser spectroscopy”. *Zeitschrift für Physik A Atomic Nuclei* 331.4 (1988), pp. 521–522.

[Laz+01] I. Lazarus, E. E. Appelbe, P. A. Butler, P. j. Coleman-Smith, J. R. Cresswell, S. J. Freeman, R. D. Herzberg, I. Hibbert, D. T. Joss, S. C. Letts, R. D. Page, V. F. E. Pucknell, P. H. Regan, J. Sampson, J. Simpson, J. Thornhill, and R. Wadsworth. “The GREAT triggerless total data readout method”. *IEEE Transactions on Nuclear Science* 48.3 (June 2001), pp. 567–569. ISSN: 0018-9499.

[Lei+95] M Leino, J Äystö, T Enqvist, P Heikkinen, A Jokinen, M Nurmia, A Ostrowski, W.H Trzaska, J Uusitalo, K Eskola, P Armbruster, and V Ninov. “Gas-filled recoil separator for studies of heavy elements”. *Nuclear Instruments and Methods in Physics Research Section B: Beam Interactions with Materials and Atoms* 99.1 (1995). Application of Accelerators in Research and Industry ’94, pp. 653–656. ISSN: 0168-583X.

[Mar06] Brian R Martin. *Nuclear and particle physics: an introduction*. John Wiley & Sons, 2006.

[May50] Maria Goeppert Mayer. "Nuclear Configurations in the Spin-Orbit Coupling Model. I. Empirical Evidence". *Phys. Rev.* 78 (1 Apr. 1950), pp. 16–21.

[Mis+93] VI Mishin, VN Fedoseyev, H-J Kluge, VS Letokhov, HL Ravn, F Scheerer, Y Shirakabe, S Sundell, O Tengblad, Isolde Collaboration, et al. "Chemically selective laser ion-source for the CERN-ISOLDE on-line mass separator facility". *Nuclear Instruments and Methods in Physics Research Section B: Beam Interactions with Materials and Atoms* 73.4 (1993), pp. 550–560.

[Mor56] H. Morinaga. "Interpretation of Some of the Excited States of $4n$ Self-Conjugate Nuclei". *Phys. Rev.* 101 (1 Jan. 1956), pp. 254–258.

[Mue+04] W. F. Mueller, W. Reviol, M. P. Carpenter, R. V. F. Janssens, F. G. Kondev, K. Abu Saleem, I. Ahmad, H. Amro, C. R. Bingham, J. Caggiano, C. N. Davids, D. Hartley, A. Heinz, B. Herskind, D. Jenkins, T. L. Khoo, T. Lauritsen, W. C. Ma, J. Ressler, L. L. Riedinger, D. G. Sarantites, D. Seweryniak, S. Siem, A. A. Sonzogni, J. Uusitalo, P. G. Varmette, I. Wiedenhöver, and R. Wadsworth. "High-spin states in ^{179}Au: Spectroscopy of shape-driving orbitals beyond the neutron midshell". *Phys. Rev. C* 69 (6 June 2004), p. 064315.

[Nil55] Sven Gösta Nilsson. "Binding states of individual nucleons in strongly deformed nuclei". *Dan. Mat. Fys. Medd.* 29.CERN-55-30 (1955), pp. 1–69.

[NND] NNDC. *National Nuclear Data Center*. URL: `https://www.nndc.bnl.gov/ensdf/` (visited on 12/02/2018).

[Pag+03] R.D. Page, A.N. Andreyev, D.E. Appelbe, P.A. Butler, S.J. Freeman, P.T. Greenlees, R.-D. Herzberg, D.G. Jenkins, G.D. Jones, P. Jones, D.T. Joss, R. Julin, H. Kettunen, M. Leino, P. Rahkila, P.H. Regan, J. Simpson, J. Uusitalo, S.M. Vincent, and R. Wadsworth. "The GREAT spectrometer". *Nuclear Instruments and Methods in Physics Research Section B: Beam Interactions with Materials and Atoms* 204 (2003). 14th International Conference on Electromagnetic Isotope Separators and Techniques Related to their Applications, pp. 634–637. ISSN: 0168-583X.

[Pau+95] E. S. Paul, P. J. Woods, T. Davinson, R. D. Page, P. J. Sellin, C. W. Beausang, R. M. Clark, R. A. Cunningham, S. A. Forbes, D. B. Fossan, A. Gizon, J. Gizon, K. Hauschild, I. M. Hibbert, A. N. James, D. R. LaFosse, I. Lazarus, H. Schnare, J. Simpson, R. Wadsworth, and M. P. Waring. "In-beam γ-ray spectroscopy above ^{100}Sn using the new technique of recoil decay tagging". *Phys. Rev. C* 51 (1 Jan. 1995), pp. 78–87.

[Rad95] D.C Radford. "ESCL8R and LEVIT8R: Software for interactive graphical analysis of HPGe coincidence data sets". *Nuclear Instruments and Methods in Physics Research Section A: Accelerators, Spectrometers, Detectors and Associated Equipment* 361.1 (1995), pp. 297–305. ISSN: 0168-9002.

[Rah08] P. Rahkila. "Grain—A Java data analysis system for Total Data Readout". *Nuclear Instruments and Methods in Physics Research Section A: Accelerators, Spectrometers, Detectors and Associated Equipment* 595 (3 Jan. 2008), pp. 637–642.

[RW10] David J Rowe and John L Wood. *Fundamentals of Nuclear Models*. WORLD SCIENTIFIC, 2010. DOI: 10.1142/6209.

[Sch+03] C Scholey, DM Cullen, ES Paul, JE Bastin, MA Bentley, AJ Boston, AM Bruce, PA Butler, M Caamaño, O Dorvaux, et al. "Recoil-isomer tagging techniques at RITU". *Exotic Nuclei and Atomic Masses*. Springer, 2003, pp. 494–494.

[Sch+92] W.-D. Schmidt-Ott, H. Salewski, F. Meissner, U. Bosch-Wicke, P. Koschel, V. Kunze, and R. Michaelsen. "Isomerism in neutron-deficient iridium isotopes alpha- and beta-decay studies of 171–175Ir". *Nuclear Physics A* 545.3 (1992), pp. 646–664. ISSN: 0375-9474.

[SDW77] U. Schötzig, K. Debertin, and K.F. Walz. "Standardization and decay data of 133Ba". *The International Journal of Applied Radiation and Isotopes* 28.5 (1977), pp. 503–507. ISSN: 0020-708X.

[Sii68] Antti Siivola. "Alpha-active gold isotopes". *Nuclear Physics A* 109.1 (1968), pp. 231–235. ISSN: 0375-9474.

[Sma13] James Smallcombe. "E0 Measurements in 154Sm Using SAGE: An Investigation of Collectivity in Rare-Earth Nuclei". PhD thesis. University of York, 2013.

[TFL49] C. H. Townes, H. M. Foley, and W. Low. "Nuclear Quadrupole Moments and Nuclear Shell Structure". *Phys. Rev.* 76 (9 Nov. 1949), pp. 1415–1416.

[TL03] Paul A Tipler and Ralph Llewellyn. *Modern physics*. Macmillan, 2003.

[Uus+03] J. Uusitalo, P. Jones, P. Greenlees, P. Rahkila, M. Leino, A.N. Andreyev, P.A. Butler, T. Enqvist, K. Eskola, T. Grahn, R.-D. Herzberg, F. Hessberger, R. Julin, S. Juutinen, A. Keenan, H. Kettunen, P. Kuusiniemi, A-P. Leppänen, P. Nieminen, R. Page, J. Pakarinen, and C. Scholey. "In-beam spectroscopy using the JYFL gas-filled magnetic recoil separator RITU". *Nuclear Instruments and Methods in Physics Research Section B: Beam Interactions with Materials and Atoms* 204 (2003). 14th International Conference on Electromagnetic Isotope Separators and Techniques Related to their Applications, pp. 638–643. ISSN: 0168-583X.

[Van+16] Céline Van Beveren, AN Andreyev, AE Barzakh, Thomas Elias Cocolios, RP de Groote, D Fedorov, VN Fedosseev, Rafael Ferrer, Lars Ghys, Mark Huyse, et al. "α-decay study of Tl". *Journal of Physics G: Nuclear and Particle Physics* 43.2 (2016), p. 025102.

[Ven+11] M. Venhart, A.N. Andreyev, J.L. Wood, S. Antalic, L. Bianco, P.T. Greenlees, U. Jakobsson, P. Jones, R. Julin, S. Juutinen, S. Ketelhut, M. Leino, M. Nyman, R.D. Page, P. Peura, P. Rahkila, J. Sarén, C. Scholey, J. Sorri, J. Thomson, and J. Uusitalo. "Shape coexistence in odd-mass Au isotopes: Determination of the excitation energy of the lowest intruder state in 179Au". *Physics Letters B* 695.1 (2011), pp. 82–87. ISSN: 0370-2693.

[Ven+17] M Venhart, FA Ali, W Ryssens, JL Wood, DT Joss, AN Andreyev, Kalle Auranen, B Bally, M Balogh, M Bender, et al. "De-excitation of the strongly coupled band in Au 177 and implications for core intruder configurations in the light Hg isotopes". *Physical Review C* 95.6 (2017), p. 061302.

[VH00] P. Van Duppen and M. Huyse. "Shape coexistence around the Z=82 closed shell probed by α-decay". *Hyperfine Interactions* 129.1 (Dec. 2000), pp. 149–161. ISSN: 1572-9540.

[Wei35] C. F. v. Weizsäcker. "Zur Theorie der Kernmassen". *Zeitschrift für Physik* 96.7 (July 1935), pp. 431–458. ISSN: 0044-3328.

[Wei51] V. F. Weisskopf. "Radiative Transition Probabilities in Nuclei". *Phys. Rev.* 83 (5 Sept. 1951), pp. 1073–1073.

[Woo+92] J.L Wood, K Heyde, W Nazarewicz, M Huyse, and P van Duppen. "Coexistence in even-mass nuclei". *Physics Reports* 215.3 (1992), pp. 101–201. ISSN: 0370-1573.

[Woo+99] JL Wood, EF Zganjar, Caroline De Coster, and Kristiaan Heyde. "Electric monopole transitions from low energy excitations in nuclei". *Nuclear Physics A* 651.4 (1999), pp. 323–368.

[WS54] Roger D. Woods and David S. Saxon. "Diffuse Surface Optical Model for Nucleon-Nuclei Scattering". *Phys. Rev.* 95 (2 July 1954), pp. 577–578.

[ZRL11] H. F. Zhang, G. Royer, and J. Q. Li. "Assault frequency and preformation probability of the α emission process". *Phys. Rev. C* 84 (2 Aug. 2011), p. 027303.